MASTER THESIS

Gel pad sensitivity studies and muon reconstruction in a water basin in Geant4 for IceCube multi-PMT optical modules

Supervisor:
Prof. Dr. Alexander Kappes

Second examiner:
Prof. Dr. Carlos Guerrero Sánchez

A thesis submitted in fulfilment of the requirements for the degree of
Master of Science *at* Westfälische Wilhelms-Universität Münster
Máster Interuniversitario en Física Nuclear *at* Universidad de Sevilla
by

Francisco Javier Vara Carbonell

AG Kappes
Institute for Nuclear Physics

April 2022

Declaration of Academic Integrity

I hereby confirm that this thesis on "Gel pad sensitivity studies and muon reconstruction in a water basin in Geant4 for IceCube multi-PMT optical modules" is solely my own work and that I have used no sources or aids other than the ones stated. All passages in my thesis for which other sources, including electronic media, have been used, be it direct quotes or content references, have been acknowledged as such and the sources cited.

Signature: Francisco Javier Vara Carbonell

Date: 06.04.2022

I agree to have my thesis checked in order to rule out potential similarities with other works and to have my thesis stored in a database for this purpose.

Signature: Francisco Javier Vara Carbonell

Date: 06.04.2022

Contents

1 Introduction

In the early 20th century, the explanation of the continuous energy spectrum of electrons emitted in the β-decay (β^-) had become a challenging puzzle to solve. At that time, only three particles were known: the electron, the photon and the proton, and only the first ones could be detected together with the daughter nucleus. This indicated that some part of the energy was missing, and even renowned physicists such as N. Bohr suggested that maybe the law of conservation of energy held only in a statistical sense [1].

The first step towards finding a solution was taken by W. Pauli, who postulated a new neutral particle that should exist in the nucleus and be emitted together with the electron. He called this particle *neutron*, but was later renamed by E. Fermi as *neutrino* after the discovery of the neutron by J. Chadwick [2]. In addition, E. Fermi provided a more accurate description of the solution [3] and stated that both the electron and the (anti)neutrino are created in the decay.

Even though W. Pauli was afraid that neutrinos might never be detected, it was first achieved (for the electronic antineutrino) in 1956 by C. L. Cowen and F. Reines [4]. This opened up a new world of opportunities, as the low interaction rate of neutrinos and their neutral character make them ideal astrophysical messengers. Consequently, they represent the key to solving some of the mysteries science is facing today, such as finding the origins and acceleration sites of high-energy cosmic rays.

As a consequence of the extremely low interaction rates of high-energy neutrinos, their detection requires large instrumented volumes. In this context, *IceCube* [5] stands out as the world's largest neutrino telescope with $\sim 1\,\mathrm{km}^3$. In IceCube, neutrinos are indirectly detected via the Cherenkov radiation from secondary charged particles from neutrino interactions with the medium. The detector is formed by more than 5,000 digital optical modules (DOMs) provided with a single photomultiplier (PMT), which are deployed along 86 strings in the Antarctic ice. The ice serves as a support structure for the array, and as an interaction medium for the neutrinos as well as a transparent Cherenkov medium. The detector became fully operational in 2011, and high-energy astrophysical neutrinos were detected for the first time in 2013 [6].

In view of a new generation of neutrino telescopes, which transitions from the era of discovery to the era of precision, IceCube will undergo two extensions in the near future: IceCube Upgrade and IceCube Gen2. They will extend the energy range of the detector and allow for better angular sensitivity, detection rate and understanding of the properties of glacial ice and the response of the modules. To achieve these objectives, the extensions are accompanied by new and improved optical modules that feature several PMTs housed in a transparent glass vessel. These include the multi-PMT Digital Optical Module (mDOM) and the eLongated Optical Module (LOM). Unlike the current optical modules, the sensitive area is fragmented, which provides the modules with some advantages, such as intrinsic directional resolution. In addition, they have a larger effective photosensitive area and nearly uniform angular coverage. For technical reasons, the mDOM will only be deployed in the IceCube Upgrade, and the LOM, which is a thinner design, is planned for IceCube Gen2. There are two basic designs of this module. The one that will be considered throughout this thesis consists of 16 PMTs slightly larger than those of the mDOM also contained within a pressure vessel. A further difference between the mDOM and the LOM is that the latter presents *gel pads* covering the front part of the PMTs instead of reflectors, whose aim is to increase the sensitive area of the modules.

The aim of this thesis was to assist in the development of the LOM and to provide a better understanding of the performance of both new modules through simulations with Geant4. In this regard, the performance for different gel pad casting approaches is considered in chapter 5, and the shape of

the gel pads, together with the effect of imperfections caused by roughness and the latest LOM-16 configuration created by the IceCube collaboration, are discussed in chapter 6. Finally, in chapter 7, the zenith angle resolution of the mDOM and the LOM for individual simulated atmospheric muons in water was studied using machine learning for reconstruction.

2 Neutrino: a cosmic messenger

The properties of neutrinos make them ideal astrophysical messengers that can provide answers to some of the questions currently intriguing the scientific community, such as the origin of cosmic rays. The aim of this chapter is to introduce neutrinos and neutrino astronomy.

2.1 Neutrino physics

Neutrinos are elemental particles. More precisely, they are fermions and belong to the lepton family together with the $\boldsymbol{e}^-$, the $\boldsymbol{\mu}^-$, the $\boldsymbol{\tau}^-$ and all the respective antifermions.

Neutrinos, ν, and antineutrinos, $\bar{\nu}$, come in three different flavours: electron, ν_e and $\bar{\nu}_e$; muon, ν_μ and $\bar{\nu}_\mu$; and tauon, ν_τ and $\bar{\nu}_\tau$. Where ν_l ($\bar{\nu}_l$) is the neutrino (antineutrino) which is produced with l^+ (l^-), or that produces l^- (l^+) in charged current (CC) weak interactions, being $l = e, \mu, \tau$.

Neutrino flavour oscillations have been observed (e.g. [7, 8]), and their discovery was the reason for the Nobel Prize in Physics in 2015 [9]. This implies that given a source of neutrinos of a particular flavour, e.g. ν_μ, with a given energy, E. The probability of finding a neutrino of a different flavour, e.g. ν_τ, at a sufficiently large distance, L, from the source of neutrinos is different from zero, $P(\nu_\mu \to \nu_\tau; E, L) \neq 0$ [10]. The reason behind that is neutrino flavour-eigenstates propagate as a superposition of neutrino mass-eigenstates. Thus, neutrino oscillations are direct evidence that neutrinos have mass, contradicting the Standard Model's expectations.

Although the mass of neutrinos remains uncertain, it is known that they are near-massless particles. Recent experiments have set an upper limit for the one of the electron anti-neutrino at $0.8\,\mathrm{eV/c^2}$ with a confidence level of 90 % [11] . As a result, neutrino gravitational interaction can be neglected. Being neutral particles and leptons, the only way they can interact is by means of the weak interaction.

Weak interactions can be differentiated into two main branches: charged current (CC), which is mediated by the charged massive bosons W^+ and W^-; and neutral current (NC), mediated by the neutral massive boson Z^0. At the typical detection energies of neutrino telescopes ($> 10\,\mathrm{GeV}$), these interactions are dominated by deep inelastic scattering:

$$\overset{(-)}{\nu}_l + N \xrightarrow{W^\pm} l^\pm + X \text{ (CC)}, \qquad \overset{(-)}{\nu}_l + N \xrightarrow{Z^0} \overset{(-)}{\nu}_l + X \text{ (NC)}, \tag{2.1.1}$$

where N is a proton or a neutron, X is the resulting set of final hadrons that can give rise to a hadronic shower, and $l = e, \mu, \tau$.

2.2 Neutrino astronomy

Due to the extremely low interaction rate of neutrinos with matter and their neutral character, they remain unaltered[1] from their creation until their detection. They are then advantageous over other astronomical messengers like charged particles, which are deflected by galactic magnetic fields; and electromagnetic radiation, which are quickly absorbed in matter, providing only information about the surface of astrophysical objects [12]. Besides, the space is opaque to high energy γ-rays ($> \mathrm{PeV}$) due to scattering on radiation fields such as the microwave background. However, it comes at the cost that neutrinos are extremely difficult to detect, especially at the high energies of astrophysical

[1] Omitting neutrino flavour oscillations.

neutrinos, which exhibit low fluxes as shown in Figure 2.2.1. For this reason, large volume detectors are needed for neutrino astronomy.

The production of high energetic astrophysical neutrinos is related to cosmic rays. They[2] are ionised nuclei formed by $\sim$ 90 % protons,$\sim$ 9 % alpha-particles and $\sim$ 1 % of heavier nuclei and characterised by the very high energies they can exhibit, which have been observed up to 10^{20}eV [13]. The main questions concerning cosmic rays refer to their origin and the places where they are accelerated to such high energies. Neutrinos can be the key to solving these mysteries, as it is believed they are produced in the same places, mainly after the decay of charged pions (and kaons) resulting from cosmic rays interactions with matter and radiation fields.

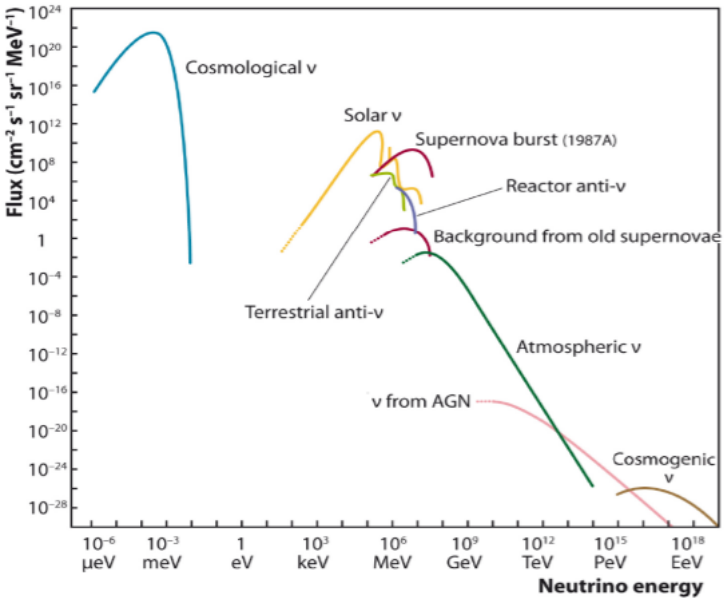

Figure 2.2.1: Theoretical and measured neutrino fluxes from natural and reactor neutrino sources. Image taken from [14].

Today, the most accepted theories about the origin of cosmic rays suggest a *bottom-up* scenario, where low-energetic charged particles are gradually accelerated to the energies that are observed. Promising galactic acceleration and creation candidates are supernova explosions, where collisions of particles with the gas of the shock front that is created can accelerate them by the so-called *Fermi mechanism of first order*. Furthermore, cosmic rays can be accelerated in regions with high magnetic fields, where associated electric fields arise as a result of their variations. These regions include super nova remnants such as pulsars i.e. a highly magnetised spinning neutron star [12]. Some of the most energetic cosmic rays can be obtained from the acceleration in extragalactic regions such as *Active Galactic Nuclei* (AGN). It is widely accepted that they consist of supermassive black holes at the centre of galaxies which are powered by an accreting disk [15], where the motions of the plasma generate strong electromagnetic fields. In addition to that, AGCs feature two relativistic jets perpendicular to the accretion disk that are able to accelerate particles to high energies. In case one of the jets is pointing towards our line of sight, AGCs are known as *blazars*. In this respect, neutrinos of 290 TeV have been detected with an arrival direction consistent with the location of the γ-ray-blazar TXS 0506+056 [16].

Cosmic rays are attenuated by interactions with photons from the microwave background. These are known as GZK interactions due to Greisen, Zatsepin and Kuzmin [17, 18]. Protons interactions with such photons produce resonant Δ^+ particles that decay into pions (π^+), which in turn decay into high energetic cosmogenic neutrinos $\sim$ EeV (see Figure 2.2.1).

[2] Also known as primary charged cosmic rays.

Other sources of astrophysical neutrinos are:

- **Core-collapse supernoave:**$\sim 99\,\%$ of the gravitational binding energy is released into neutrinos of all flavours [19].
- **Solar neutrinos:** As a result of the nuclear reactions in the Sun.

Neutrino astronomy experiments are usually set at great depths underground to minimise the background in the already infrequent neutrino detections, e.g. coming from products of *air showers*. Interactions of (primary) cosmic rays with the nuclei from the atoms of the atmosphere lead to the creation of fluxes of secondary particles, that in turn can interact and produce tertiary particles and so on. As a result, an air shower of particles is created as can be seen in Figure 2.2.2. Electrons, positrons, photons and hadrons are absorbed rapidly in the atmosphere and at shallow depths. Hence, only atmospheric neutrinos and high energetic atmospheric muons, which are mainly created after the decay of charged pions (and kaons) as [20]:

$$\pi^{\pm} \to \mu^{\pm} + \overset{(-)}{\nu}_{\mu}\ (\sim 100\,\%), \qquad K^{\pm} \to \mu^{\pm} + \overset{(-)}{\nu}_{\mu}\ (\sim 63.5\,\%), \tag{2.2.1}$$

constitute the main background[3]. Especially in the large range of energies that atmospheric neutrinos can have, up to PeV (Figure 2.2.1).

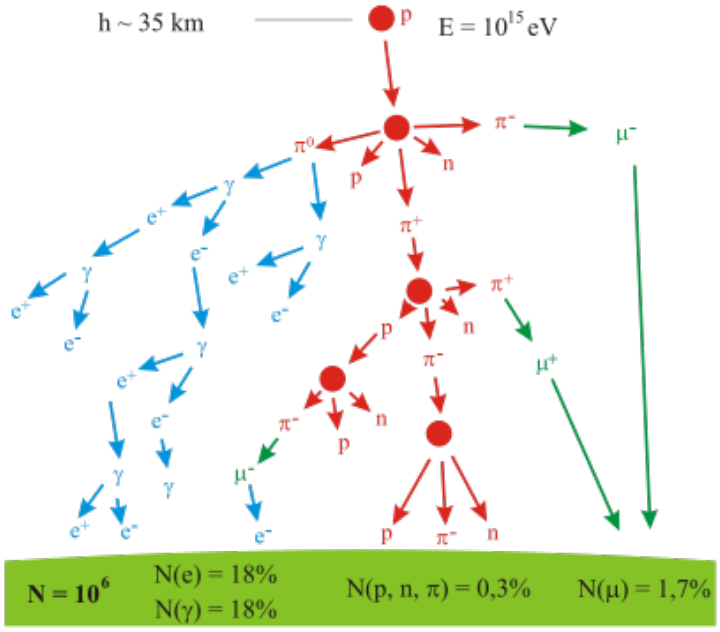

Figure 2.2.2: Schematic process of the development of a particle shower induced by a primary cosmic ray, a proton in this case. The muon part can be seen in green. Image taken from [21].

2.3 Cherenkov emission

Neutrinos are detected indirectly by means of the charged particles that are created after (weak) interactions with the detector medium[4]. In particular, the detection principle of neutrino telescopes such as IceCube [5], or detectors such as Super-Kamiokande [22] is based on the detection of Cherenkov radiation emitted by using optical modules with photomultipliers (PMTs).

[3] Atmospheric muons can also decay and produce neutrinos and antineutrinos of the electron and muon flavours.
[4] And their decay products.

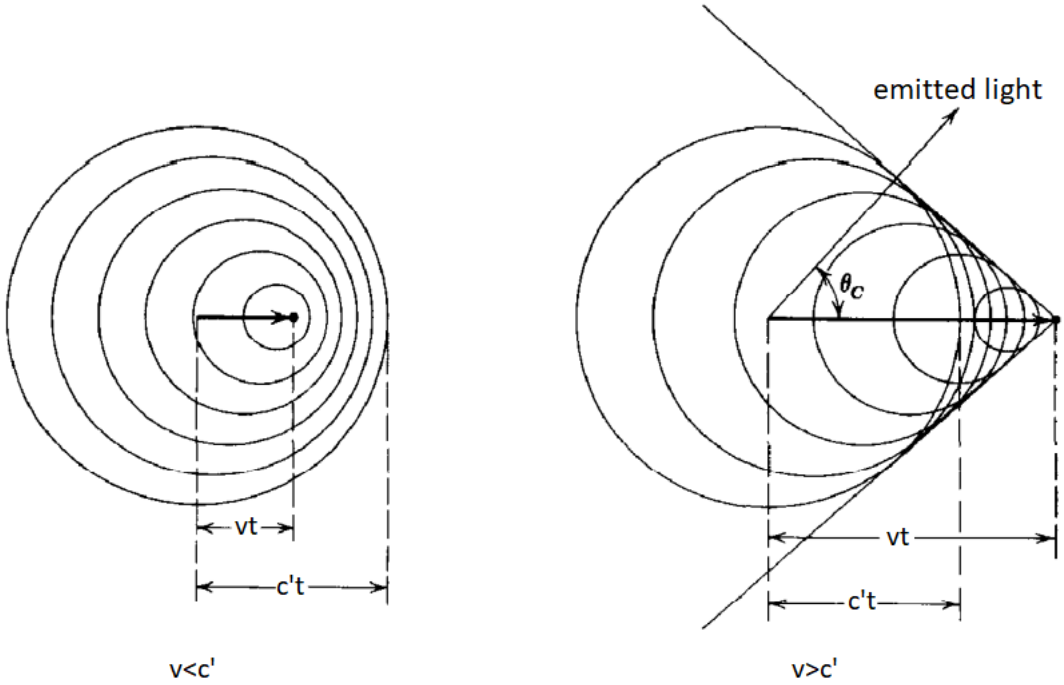

Figure 2.3.1: Diagram of a charged particle travelling through a dielectric medium. The circles represent the successive field waveforms created by the particle. **Left**: The velocity of the particle is less than that of the light in the medium ($c^{'}$). **Right**: The velocity of the particle is greater than that of the light. Explanation on text. Image taken from [23] (modified).

When a charged particle travels with a velocity greater than that of the light in a medium, an electro-magnetic shock appears and photons are emitted by the electrons of the atoms that form the dielectric medium on a cooperative phenomenon. Under such circumstance, the particle's spherical field wavelets interfere constructively (see Figure 2.3.1). As a result, light is produced on a conical surface that forms an angle θ_c with respect to the direction of the charged particle [23]. The angle θ_c can be obtained from geometrical arguments based on Figure 2.3.1 as

$$\cos(\theta_c) = \frac{c^{'}t}{vt} = \frac{ct}{nvt} = \frac{1}{n\beta}, \tag{2.3.1}$$

where $c^{'}$ is the phase velocity of light in the medium, n is the refractive index of the medium, c is the velocity of light in vacuum, v is the velocity of the charged particle and β is v/c.

An approximate formula to obtain the number of photons emitted between the interval of wavelengths λ_1 and λ_2 was given by Frank-Tamm [24]:

$$N = 2\pi\alpha l \left(\frac{1}{\lambda_2} - \frac{1}{\lambda_1}\right)\left(1 - \frac{1}{\beta^2 n^2}\right), \tag{2.3.2}$$

where α is the fine structure constant, $\alpha = e^2/(4\pi\epsilon_0\hbar c) \approx 1/137.036$, l is the travelled distance, and n is the average refractive index for the given wavelengths.

3 The IceCube Neutrino Telescope

IceCube is the first cubic-kilometer neutrino telescope and it is located at the South Pole, where it makes use of the transparent and sterile glacial ice as a Cherenkov medium for neutrino detection. Its main objective was the detection as well as the identification of sources of high-energy neutrinos, whereas secondary goals included the detection of supernova neutrinos, the search for dark matter and other exotic particles, and the study of neutrino oscillations [5, 25].

It was fully operative in 2011, and shortly afterwards, in 2013, its size made it possible to detect the most energetic astrophysical neutrinos to that time [6]. In this chapter, the IceCube array and its future extensions will be described. In addition, the detection mechanism will be explained and the new improved optical modules will be presented.

3.1 IceCube array

IceCube consists of 86 strings on the Antarctic ice that are provided with digital optical modules (DOMs), which are the sensitive components of the detector. As it can be seen in Figure 3.1.1, its main piece is a downwards 10-inch diameter photomultiplier (PMT) capable of detecting photons. In addition to that, they contain circuit boards that allow a near-autonomous operation [25].

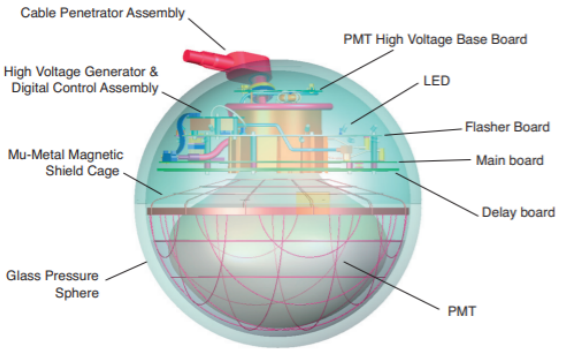

Figure 3.1.1: Drawing of the digital optical module (DOM) currently deployed on the IceCube array. Image courtesy of the IceCube collaboration.

A sketch of the Ice-Cube array is shown in Figure 3.1.2. The main in-ice array consists of 78 vertical strings each of them with 60 DOMs deployed on the ice between 1450 m and 2450 m below the surface. They have a vertical separation of 17 m and the horizontal spacing of the strings is of 125 m forming an instrumented region of a cubic-kilometer capable of detecting astrophysical neutrinos in the energy range of TeV-PeV [25].

DeepCore consists of a denser sub-array where the average horizontal separation of strings is reduced to 72 m. It is formed by eight specialised strings on the center of the array in addition to seven regular in-ice strings. With such a configuration, DeepCore is focused on lower energies providing an energy threshold of about $10\,\mathrm{GeV}$, important for studies on atmospheric neutrinos oscillations, the detection of supernova neutrinos and neutrinos from dark matter annihilation [26].

IceTop, on the contrary, is located on the surface and features 81 stations, each one with two Cherenkov tanks filled with ice that are separated by 10 m and equipped with two DOMs [27]. It serves as an air shower detector for cosmic rays in the energy range of PeV to EeV, as well as a veto array.

Finally, the IceCube Laboratory, which is the main operations building, is found at the surface in the centre of the array.

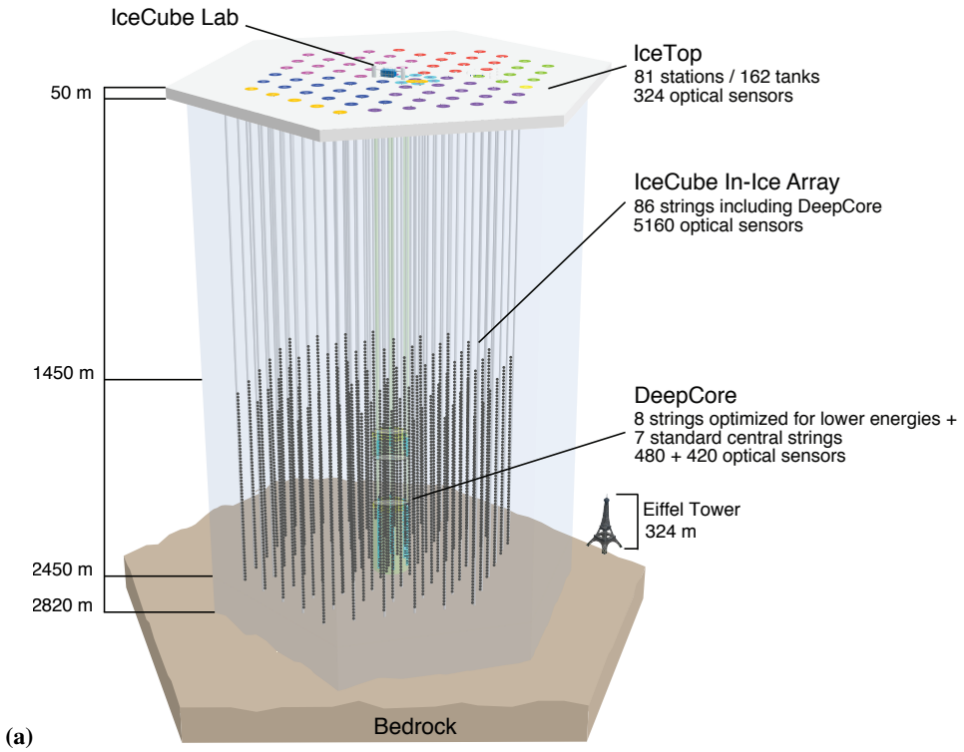

Figure 3.1.2: Schematic representation of the IceCube array. Explanation on the text. Image courtesy of the IceCube collaboration.

3.2 Event types in IceCube

At high energies (above 10 GeV), a neutrino interacting weakly with a nucleus in the ice through CC will generate a lepton that carries on average 50-80 % of the neutrino energy [5]. Furthermore, it will transfer the rest of the energy to the nucleus involved in the interaction, which will give rise to a hadronic shower near the interaction vertex. Depending on the original neutrino flavour, two main event types can be distinguished: **tracks** and **showers**.

Tracks (Figure 3.2.1a) are formed by muons[5] originating from CC interactions of ν_μ. Due to the low interaction cross section of the muons, they can travel long distances (up to 10 km at PeV energies [5]) and the events are often not fully contained within the detector volume. Since only the energy that the muon releases as it passes through the detector can be measured, the determination of the initial neutrino energy is difficult. Yet, they provide good directional information, being IceCube's angular resolution for long muon tracks better than 1° [5].

On the contrary, showers are near-spherical events (see Figure 3.2.1b) that are very localised near the interaction vertex. Electromagnetic showers arise from the electrons/positrons and the tau decay products after CC interactions of ν_e and ν_τ. On the other side, hadronic showers are created by the tau decay products as well and by the nuclear fragments at the interaction vertex after CC or NC interactions of any flavour. Since all the energy is released into a small volume that can be contained within the detector, the energy reconstruction is better than with tracks. However, the directional information is poorer.

At higher (PeV) energies, a CC interactions of ν_τ can give rise to two clearly separated showers. While the first is created at the interaction vertex by the nuclear fragments, the second results due to the products of the τ decay that experiment a slightly longer decay length. Therefore, this signature

[5] Also by any kind of background muon e.g. atmospheric muons.

is known as a **double bang** (see Figure 3.2.1c). Tau neutrinos are rarely generated in the atmosphere, so their detection is typically related to astrophysical neutrinos.

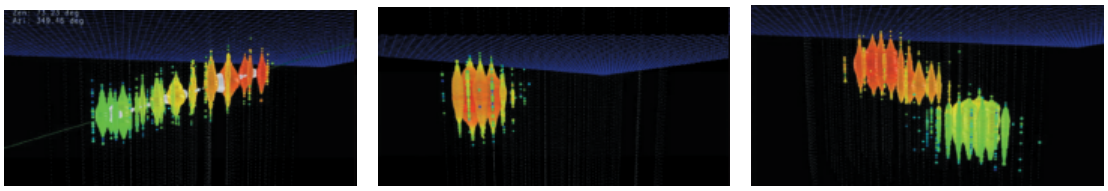

(a) **(b)** **(c)**

Figure 3.2.1: Neutrino event types in IceCube. **(a)**: Track. **(b)**: Shower. **(c)**: Double bang. Each circle represents one module, the size of the circle corresponds to the number of photons detected, and the color represents the detection time: from red (earliest) to blue (latest). Image taken from [5] (modified).

3.3 IceCube extensions

The achievement of IceCube's primary goal in 2013 with the first detection of high energetic astrophysical neutrinos [6] motivated further extensions for a new generation of neutrino telescopes. These are: IceCube Upgrade and IceCube-Gen2.

3.3.1 IceCube Upgrade

IceCube Upgrade will consists of 7 new densely instrumented strings with almost 700 modules placed within the DeepCore region as it is seen in Figure 3.3.1a. It will allow to lower the detection energy threshold to a few GeV. Moreover, it will increase the sensitivity for the detection of tau neutrinos and neutrino oscillations [28].

The Upgrade entails new and improved optical modules, which include: the multi-PMT digital optical module (mDOM), which features 24 3-inch PMTs in a pressure vessel [29], the dual optical sensor (D-Egg), which presents two 8-inch PMTs facing upwards and downwards on a UV-transparent glass vessel [30], and PDOMs, which are high-quantum efficiency IceCube DOMs with improved electronics [31].

Additionally, calibration functions will be performed. To this end, dedicated instruments will be deployed and optical modules equipped with calibration devices such as cameras with flashers and calibration LEDs. The aim is to better understand the response of the current deployed modules as well as the properties of glacial ice, which will allow for improved reconstruction algorithms and re-analysis of the data collected so far. Finally, research and development of IceCube Gen2 optical modules will be carried out.

Multi-photomultiplier Digital Optical Module (mDOM)

The mDOM (depicted in Figure 3.3.1b) follows the multi-PMT approach introduced by the KM3Net optical module [32]. It features 24 3-inch PMTs inside a glass vessel that are optically coupled to it by means of silicon-based gel and are sustained by a 3-D printed supporting structure. Each PMT is equipped with an active base that generates high-voltage in situ. Furthermore, the front part of the PMTs are surrounded by conical aluminium reflectors, whose aim is to reflect photons back to the photocathode to increase the sensitive area of the module. This results in a sensitivity $\sim 20\,\%$ higher than with realistic alternative configurations [33]. However, as they are made of a conductive material and placed close to a PMT operating at a negative high-voltage, they can induce dark rate noise, which can be avoided by connecting the reflectors to the photocathode potential [34]. Calibration devices

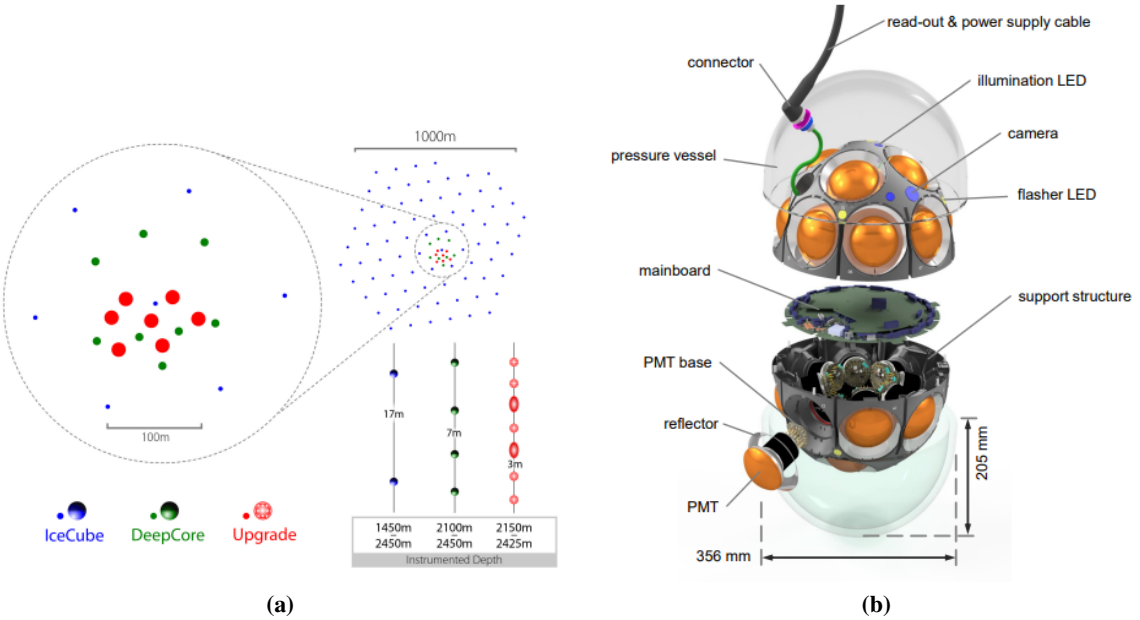

(a) (b)

Figure 3.3.1: (a): IceCube-upgrade layout. In red the seven new strings that will be deployed, whereas DeepCore is shown on green and the main in-ice array in blue. **(b)** Exploded view of the mDOM. Images courtesy of the IceCube collaboration.

such as illumination LEDs, flasher LEDs and cameras to monitor the optical properties of ice are also present [29, 33].

There are numerous advantages of the multi-PMT concept over the single-PMT design of the current IceCube DOM [35]. First, 24 3-inch PMTs provide more than twice the photocathode area of a single 10-inch PMT, and its distribution over the entire surface of the module ensures a nearly homogeneous angular acceptance over the entire solid angle. In addition, the photon counting is improved, as several PMTs can participate at the same time, which also extends the overall dynamic range. The segmentation of the sensitive area provides the module with intrinsic directional resolution, which can be used for event reconstruction (as will be done in chapter 7). Moreover, it is possible to use local event coincidences e.g. to suppress some background events.

3.3.2 IceCube-Gen2

IceCube-Gen2 will be built to meet the requirements for the physics objectives of a next-generation neutrino observatory, including improved sensitivity to point sources, a higher neutrino collection rate and an extension of the energy range (to higher energies) by several orders of magnitude [36, 37].

To target higher energies, the volume of the current detector will be expanded by approximately one order of magnitude up to $7.9\,\mathrm{km}^3$. This will be done in two ways, which are possible thanks to a better understanding of the properties of glacial ice. On the one hand, the deployment of the modules on the strings will be $125\,\mathrm{m}$ longer both above and below the current positions. On the other side, the average distance between the strings will be extended. Hence, in the preliminary baseline design of the optical array [36], 9600 new optical modules will be deployed on 120 strings, each one holding 80 modules, with an average horizontal and vertical separation of $240\,\mathrm{m}$ and $16\,\mathrm{m}$, respectively, at depths between $1325\,\mathrm{m}$ and $2575\,\mathrm{m}$. A schematic of this new array can be seen in Figure 3.3.2.

As with the IceCube array, a surface array is planned for IceCube-Gen2, consisting of two ice-Cherenkov tanks at the top of each string. Furthermore, IceCube-Gen2 will feature a radio detector array that will target at energies above $10\,\mathrm{PeV}$ [37].

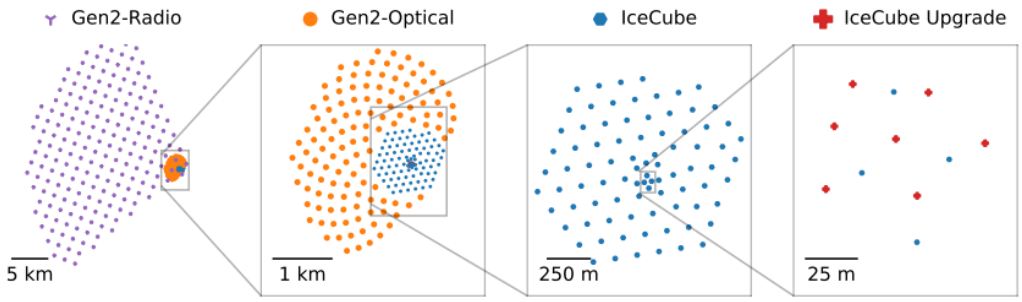

Figure 3.3.2: Schematic top view of the future IceCube Gen2 Neutrino Observatory. From left to right: Gen2-Radio array, Gen2-Optical array, current IceCube array, IceCube Upgrade. Image courtesy of the IceCube Collaboration.

For technical reasons, narrower modules are designed to fit into a thinner ice column, which saves time and fuel in the ice drilling process, whereas their lengths are restricted due to a maximum weight of 26 kg [38]. In line with this, two versions of the *eLongated Optical Module* (LOM) are being developed: the LOM-16 with a diameter of 313 mm and the LOM-18 with a diameter of 305 mm. The main difference between them is two additional PMTs that are placed facing upwards and downwards on the LOM-18. Of special interest for this thesis will be the LOM-16, hereafter referred to simply as LOM.

eLongated optical module (LOM)

The LOM (see Figure 3.3.3) [38, 39] is a thinner redesign of the mDOM, which possessed a diameter of 356 mm. It follows the multi-PMT concept, housing 16 4-inch diameter PMTs that provide a slightly larger photocathode area than the mDOM. A further difference is the absence of metallic reflectors surrounding the front part of the PMTs. Instead, they are covered by pads made of transparent silicone gel (**gel pads**), which have two functions: In the first place, they solve the optical coupling between the PMTs and the glass vessel. Secondly, they increase the sensitive area thanks reflections[6] of the photons at the interface between them and the air inside the module. Since gel pads bond the PMTs to the glass vessel, a 3D printed PMT supporting structure like the one of the mDOM is no longer needed for the LOM, which saves on costs. In addition, there are no longer metallic components (such as reflectors) near PMTs operating at high voltage that can induce dark rate noise.

The sensitivities for a LOM model with reflectors and a mDOM-like holding structure, and for a regular LOM model with gel pads have been simulated in Geant4, resulting in $\sim 7\,\%$ more photon collection for the gel pad model [40]. One of the reasons is that total internal reflections are 100 % efficient, while metallic reflectors only provide around 90 %. Secondly, gel pads are transparent and therefore have a higher angular acceptance, whereas reflectors are limited to photons coming from above. An increase in the sensitive area due to the gel pads has been experimentally confirmed [38].

In the scope of this thesis, Geant4 Monte Carlo simulation for the sensitivities of three different gel pad casting approaches are done in chapter 5. Additionally, the shape of the gel pads as well as the latest LOM-16 geometry are discussed based on simulations in chapter 6.

[6] And to some extent also refractions.

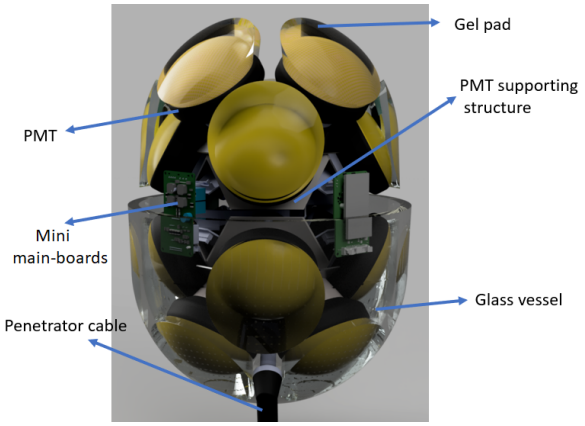

Figure 3.3.3: Representation of the LOM-16, a multi-PMT optical module for IceCube-Gen2. It features 16 PMTs on a glass vessel with a smaller diameter than the one of the mDOM. Image courtesy of the IceCube collaboration.

4 Geant4 simulations

Geant4 is a simulation toolkit [41] that allows to simulate the passage of particles through matter making use of Monte Carlo methods. It employs object-oriented programming (in C++), and offers a wide variety of classes for different purposes. It has its origins in the FORTRAN-based Geant3 simulation software and was first launched in 1998, having evolved into a major collaboration that involves institutions and universities in Europe, Canada, the United States and Japan [42]. Applications of Geant4 can be found in diverse fields ranging from medical physics to the space industry and accelerator design as examples.

The main results of this thesis will be obtained by means of simulations carried out with Geant4. In this chapter, its functioning is briefly discussed together with some of the used tools.

4.1 Geant4 basics

Geant4 allows to simulate a customisable environment (world), in which objects and regions with specific physical properties are created and placed. Different types of particles (primary events) are launched, which can interact with all the different components of that environment through selected physical processes. Furthermore, it is possible to track the particles and store all relevant information (such as energy, position and time) as they reach sensitive regions. It also provides means to visualise the created environment and the trajectories of the particles.

Geometry construction in Geant4 is a three-step process. First of all, a **solid** is created by specifying the shape. For this purpose, Geant4 offers a series of classes that range from basic geometries such as cones (G4Cons) or spheres (G4Sphere) to more sophisticated ones. Alternatively, it is possible to import geometries from CAD (computer-aided design). Boolean operations such as union, intersection and subtraction of solids are possible. The next step consists of creating a **logical volume**, by which physical properties are assigned to the solid, e.g. via the materials it is made of. Finally, the solid is placed. Each solid must have a mother volume that encompasses it and from which it is referred to. The only exception is the world.

Isotopes and elements are used to create materials through the G4Material class, where other properties such as temperature, density, physical state and pressure can be specified. Common materials can also be extracted from a provided database. In addition, they can have optical properties such as refractive index or absorption length that are defined by a material properties table (G4MaterialPropertiesTable).

Both, particles and physics interactions must be defined within the class G4VUserPhysicsList. Physical interactions can be selected from the seven major categories that are provided. These are: electromagnetic, hadronic, decay, photolepton-hadron, optical, parametrisation and transportation. They must be assigned to a particle, which in turn are defined by their own class derived from the class G4ParticleDefinition, and organised in the categories: lepton, meson, baryon, boson, shortlived and ion [41].

4.2 LOM-16 in Geant4

The starting point of this thesis is the Geant4 code for the mDOM developed by [35, 43], which was subsequently modified in the master's thesis [40] to implement the LOM. A visualisation of the

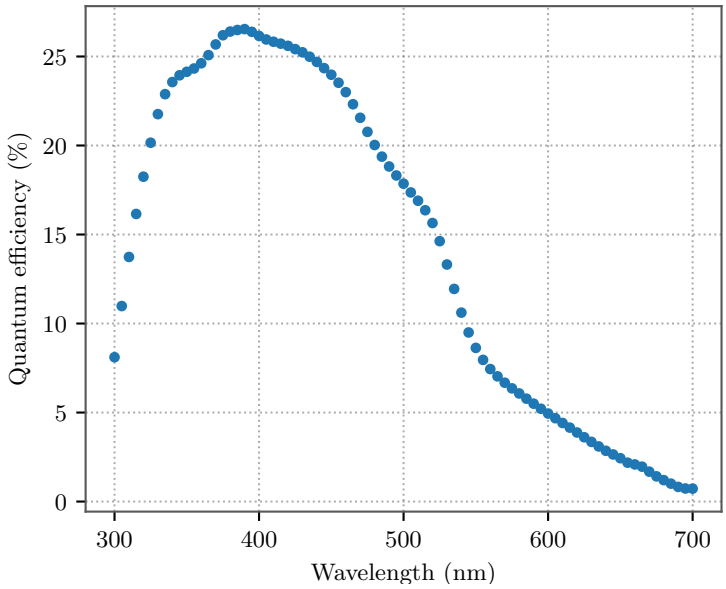

Figure 4.2.2: Quantum efficiency that was used for the calculations and the simulations throughout this thesis. The values were measured by the AG Kappes (working group) at the center of the photocathode for normal directions.

geometry of the LOM provided by Geant4 can be seen in Figure 4.2.1. It consists of 16 PMTs inside a pressure vessel, which is formed by the union of a cylindrical main body and two semi-spheres, one at the top and one at the bottom, and is 14 mm thick. The PMTs are distributed in four rows that characterise the polar and equatorial positions of the PMTs, with four in each row, whose exact positions can be found on [40]. The two hemispheres of the module are identical but the positions of the PMTs feature a 45 degree shift around the Z-axis (vertical position in Figure 4.2.1).

The response of the PMTs is not taken into account, and a photon is detected if it reaches the photocathode. There are some exceptions concerning the quantum efficiency (QE), i.e. the ratio between the number of photoelectrons produced in the photocathode and the number of photons reaching it. This property depends on the wavelength of the photon, the arriving position on the photocathode and the incident angle. To take it into account, a function was implemented (by our working group) that generates a random number when a photon arrives at the photocathode. If the number is smaller than the QE of the photon at its wavelength, it is detected, otherwise it is "killed". The values for the QE that were used in this thesis correspond to measurements at the centre of the photocathode incident normal to it and are given on Figure 4.2.2.

Optical properties such as refractive indexes and absorption lengths of all relevant materials are taken into account in the simulation as a function of the photon wavelengths. The glass vessel

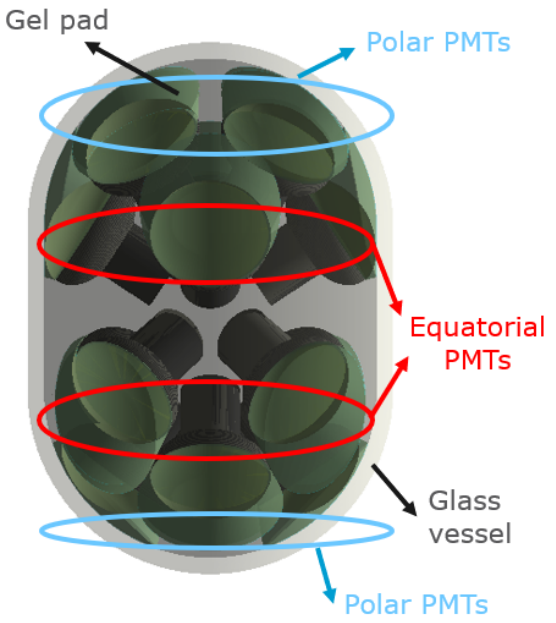

Figure 4.2.1: Geant4 visualisation of the LOM.

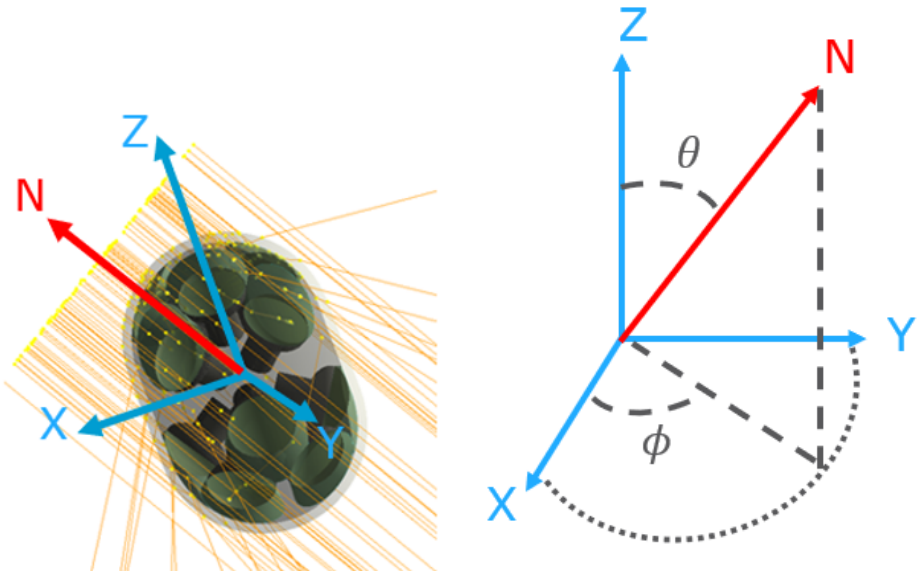

(a) (b)

Figure 4.3.1: (a): Plane wave of photons (yellow beams) pointing to the centre of the module simulated in Geant4 for the calculation of the effective area. The red arrow represents the normal vector to the plane. **(b)** Characterisation of the direction of the normal vector by the spherical angles θ and ϕ.

is made of borosilicate glass from Vitrovex [44] and the gel pads of ShinEtsu gel [45]. The rest of the module is filled with air.

As of March 2022, the module design has undergone some changes compared to the one presented in Figure 4.2.1, e.g. complete symmetry in both hemispheres. This will be covered in section 6.3.

4.3 Effective area calculation

The effective area is the parameter that is used to characterise the sensitivity of the modules as well as their angular acceptance. To calculate it, the Geant4 code **mdom_scan_angular** was used, which was created in the scope of a PhD thesis [35]. In it, a plane wave of mono-energetic photons with a diameter large enough to cover the entire module is simulated and directed towards its centre as can be seen in the Figure 4.3.1. The photons are defined by the class G4OpticalPhotons and undergo the interactions defined in the classes G4OpAbsorption and G4OpBoundary. They include optical absorption of the photons in the medium as well as reflections and refractions at the interfaces of materials that have refractive indexes or reflectivity defined. To compare different LOM geometries, it can be done at a single wavelength, therefore the QE is not considered. Unless otherwise specified, the simulations are carried out with a photon wavelength of 470 nm in accordance with [40] and in an ice environment.

The effective area, $A_{\text{eff}}(\theta, \phi)$, for a particular direction of the incident wave characterised by the azimuth (ϕ) and zenith (θ) angles in spherical coordinates, is defined as:

$$A_{\text{eff}}(\theta, \phi) = \frac{N_{\text{det}}(\theta, \phi)}{N_{\text{emit}}} \cdot A_{\text{beam}}, \tag{4.3.1}$$

where $N_{\text{det}}(\theta, \phi)$ is the number of the photons that are detected, N_{emit} is the number of emitted ones and A_{beam} is the area of the beam. It provides then a direct measurement of the angular acceptance. An overall sensitivity value can be obtained by calculating the mean effective area, $\overline{A_{\text{eff}}}$, over the

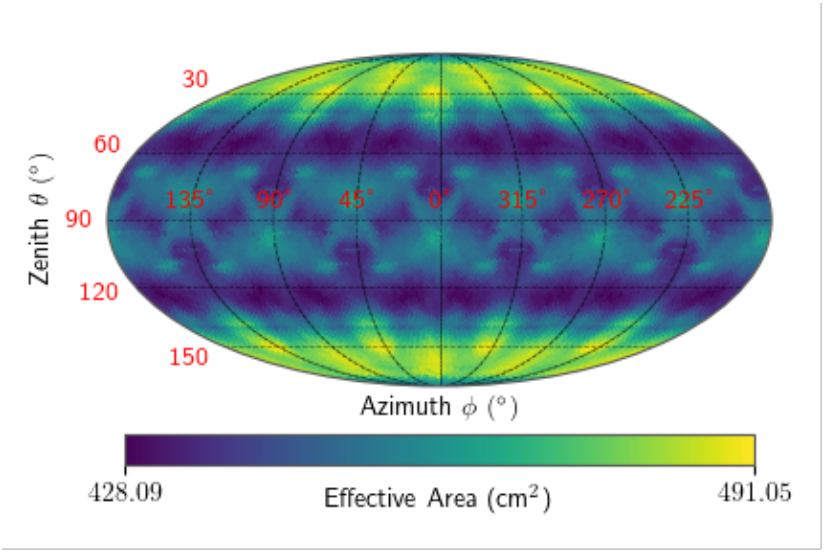

Figure 4.3.2: Example of the effective area as a function of the angles θ and ϕ that characterise the direction of the incident planes of photons using HEALPix pixelisation.

whole solid angle as:

$$\overline{A_{\text{eff}}} = \frac{1}{A_{\text{total}}} \int\int A_{\text{eff}}(\theta,\phi) \cdot \sin(\theta) d\phi d\theta, \qquad A_{\text{total}} = \int\int \sin(\theta) d\phi d\theta. \tag{4.3.2}$$

In our case, eq. 4.3.2 is converted into a sum due to the discrete step in the simulations:

$$\overline{A_{\text{eff}}} = \frac{1}{A_{\text{total}}} \sum_{\theta,\phi} A_{\text{eff}}(\theta,\phi) \cdot \sin(\theta) \Delta\theta \Delta\phi, \qquad A_{\text{total}} = \sum_{\theta,\phi} \sin(\theta) \Delta\theta \Delta\phi. \tag{4.3.3}$$

To obtain the best angular coverage and simplify the calculations, the values for the simulated (θ, ϕ) pairs are calculated by HEALPix, which can be implemented in python with the healpy package [46]. HEALPix stands for Hierarchical Equal Area isoLatitud Pixelization, and provides a pixelisation of the spherical surface in a way that every pixel covers the same area. As a result, $\sin(\theta)\Delta\phi\Delta\theta = A_{\text{pixel}}$ is constant. Thus, it is obtained

$$A_{\text{total}} = \sum_{\theta,\phi} A_{\text{pixel}} = N_{\text{pixel}} \cdot A_{\text{pixel}}, \qquad \overline{A_{\text{eff}}} = \frac{\sum_{\theta,\phi} A_{\text{eff}}(\theta,\phi)}{N_{\text{pixel}}}, \tag{4.3.4}$$

where N_{pixel} is the total number of pixels and A_{pixel} is the area of one single pixel. Moreover, the resulting pixelisation allows to represent the effective area as a function of the incident direction angles (θ, ϕ) as shown in Figure 4.3.2. It must be highlighted that due to the symmetry of the module, the overall sensitivity can be obtained by simply calculating the mean effective area over one octant of the solid angle, with the rest being equivalent.

The errors are calculated following Gaussian propagation, where its source is considered only in the number of detected photons as $\sqrt{N_{\text{det}}(\theta,\phi)}$. These only include the statistical uncertainty and do not cover systematic errors, such as the ones stemming from the material definition, construction tolerances etc.

5 Simulations for gel pad casting approaches

As explained in section 3.3.2, gel pads are a new design feature of the LOM module compared to the mDOM. They are used as an alternative to reflectors to increase the sensitive area of the module via reflections[7], whilst also serving as optical coupling between PMTs and glass vessel.

The aim of this chapter is to provide sensitivity studies through Geant4 simulations for different approaches that have been considered for the production of gel pads: *precasted pads*, *acrylic pads* and *in-situ poured pads*.

5.1 Gel pad casting approaches

Three pad casting approaches are being considered (see Figure 5.1.1) [39, 47]:

- **Precasted gel pads**: The gel is cured directly onto the glass of the PMTs using an external mould which provides the desired gel pad shape and that is removed at the end.
- **In-situ pouring**: The gel is poured and cured directly whilst assembling a half-module by using transparent (plastic) shells that surround the frontal region of the PMT which remains inside of the module after the curing process.
- **Acrylic pads**: Instead of using a solid gel pad, an acrylic lens in the desired shape is placed in front of the PMTs. However, for proper operation a thin layer of optical coupling (not restricted to gel) must be deployed at both optical interfaced (with the PMT and the vessel).

Precasted pads correspond to the original concept of gel pads, which was already implemented in Geant4 by [40] (see Figure 4.2.1). In this approach, the cured pad is assembled applying a thin layer of liquid gel to its surface and pressing it against the vessel, taking special care to ensure that no residual gasses remain in this interface to prevent delamination and bubble formation under module conditions (i.e. underpressure and low temperatures). One main problem is that the liquid gel used to adhere the gel pads to the vessel can leak out, leaving air voids and irregular surface adhesion, whereas the resulting trails impedes calibration devices such as the LED flashers. As a possible solution, the *in-situ pouring* method was considered, which retrains the gel to the desired shapes, while allowing for a stronger bond between the glass vessel and the gel pads [39, 47]. To omit possible bubble formation within the gel pads in module conditions and ease of production, acrylic pads were investigated as an alternative.

Throughout this chapter, the sensitivities of in-situ shell and acrylic pads will be compared with those of the original gel pad concept of the precasted method by simulating the respective effective areas. Hence, in most cases, relative values will be given, as they provide a more direct comparison. Furthermore, the absolute values are strongly dependent on the geometry of the gel pads, which has been set as non-overlapping cones for this chapter, with polar semi-opening angles of 26° and equatorial ones of 16°[8].

[7] That can be total internal reflections at a minimum incidence angle of $\sim 45.4^\circ$ with respect to the normal of the side of gel pads.

[8] The definition of semi-opening angle is found on chapter 6.

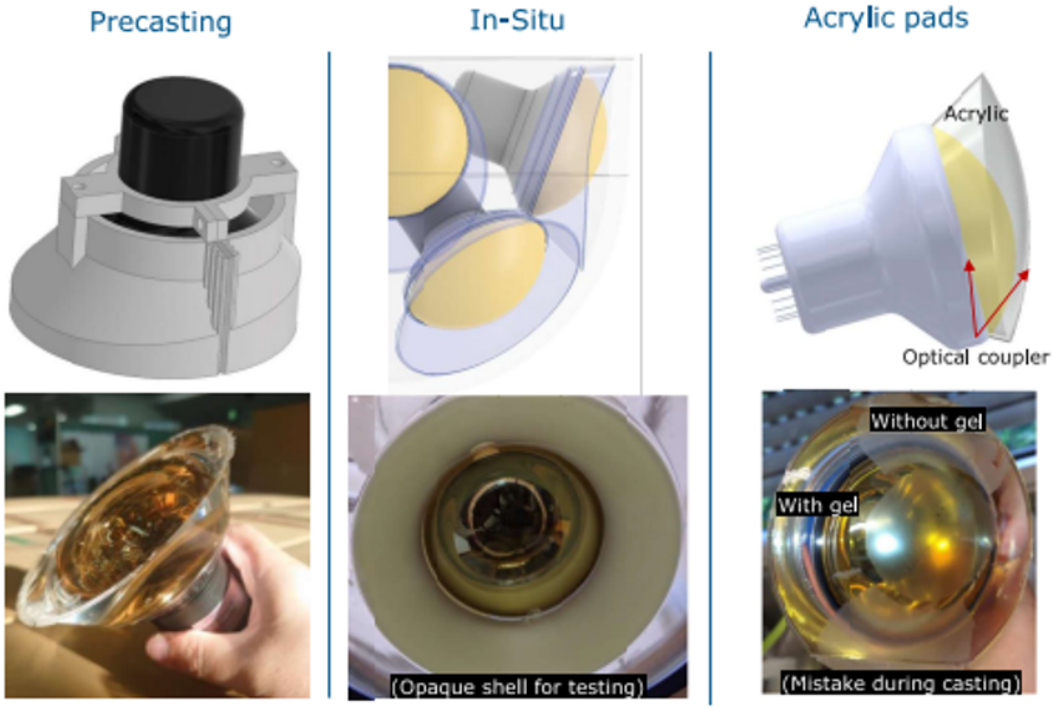

Figure 5.1.1: Gel pad casting procedures that were considered for the simulations in this chapter: **Left**: Precasting mold (top) and precasted gel pad (bottom). **Middle**: Gel pads from the in-situ pouring approach. **Right**: Acrylic pads. Images provided by Markus Dittmer.

5.2 Acrylic pad simulations

As already mentioned, acrylic pads represent a good alternative to regular gel pads as they are easier to produce. Its implementation in Geant4 consists of an acrylic body that is joined to the glass vessel and to the photocathode by a coupling material, as can be seen in Figure 5.2.1.

The main differences on the performance between acrylic pads and regular gel pads are associated with their different optical properties, such as the refractive indices and absorption lengths of the two materials and the ones of the coupling material. Regarding the refractive index, the mean effective area as a function of the acrylic and coupling refractive indices has been simulated and the results are given in Figure 5.2.2. Steps of 0.25 have been taken for the refractive index and two different coupling thicknesses (1 mm and 5 mm) have been considered.[9] The absorption lengths of the acrylic and coupling material have been set to the corresponding value of the Shin-Etsu gel at 470 nm.

Regarding the thickness of the coupling, no significant differences in performance are observed. The results in figure 5.2.2 indicate that the worst configurations feature a coupling material with a lower refractive index than the gel ($n_{gel} \sim 1.405$). This is probably due to poor optical coupling with the glass vessel, which exhibits a refractive index of ~ 1.48 at the current wavelength; and with the acrylic materials, whose minimum simulated refractive index was 1.4. For the same reason, the maximum overall value lies at refractive indexes of 1.5 ± 0.25[10] for both the coupling material and the acrylic. In particular, the mean effective area is enhanced by ~ 9.6 % with respect to the one of regular gel pads. In the vicinity of these values, the refractive indexes of the coupling, acrylic and glass materials are approximately matched and the reflections produced at their interfaces are minimised.

[9] For a 5 mm coupling, there are regions where overlaps between the upper and lower couplings are observed due to the minimal distance of the PMT photocathode window to inner vessel surface.

[10] The mean effective area for both materials at n=1.475 coincides within the error with that of n=1.5.

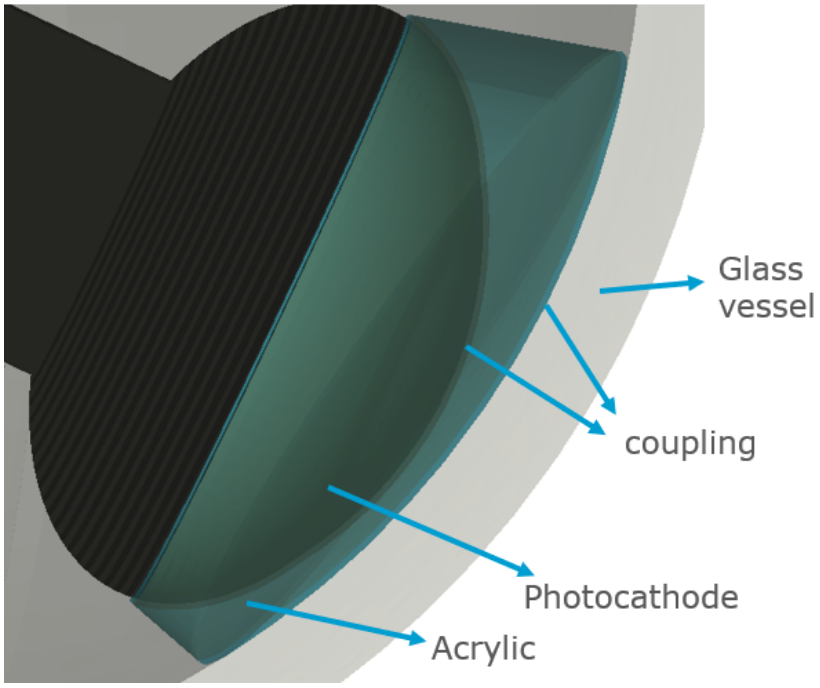

Figure 5.2.1: Acrylic pad in Geant4. The gel pad is replaced by an acrylic lens that is coupled to the photocathode and the glass vessel by a coupling material.

Moreover, following Snell's law, a pad with higher refractive index (1.5 vs. 1.405) reduces the angle at which total internal reflections occur from 45.4° to 41.8°, resulting in more efficient performance.

The next step is to take into consideration the absorption lengths of the materials. In this context, the absorption lengths of three acrylic materials from [48] have been studied, all three featuring refractive indices of ~ 1.5 over the entire wavelength spectrum that will be investigated. The values are given together with those of Vitrovex glass and Shin-Etsu gel in Figure 5.2.3.

To observe the impact of the absorption length on the performance, the mean effective area as a function of the wavelength has been simulated and the results can be seen in Figure 5.2.4 and Figure 5.2.5, where the values have been measured in steps of 10 nm from 300 nm to 570 nm. The choice of the lower limit is due to the zero absorption length below 300 nm for Vitrovex glass, whereas the upper limit corresponds to the data available in [48].

In Figure 5.2.4, 1 mm thick Shin-Etsu gel has been used as a coupler. Since acrylics have shorter absorption lengths than the gel at shorter wavelengths, the values for the mean effective areas of the acrylics are a few tens of percent worse at 300 nm, while the difference decreases with increasing wavelength and, above a wavelength of 400 nm, they all have similar values. On the other hand, in Figure 5.2.5, a hypothetical (coupling) gel with the same absorption length [11] like Shin-Etsu gel, but with a refractive index of 1.5 has been implemented as the coupling material. Although the mean effective areas of the acrylics present lower values at 300 nm, all acrylics outperform the gel at 360 nm and above, approaching values of $\sim 10\%$ larger effective areas, which is in agreement with the results from Figure 5.2.2.[12]

In order to compare the sensitivities expected from the different casting methods, sums and weighed sums from the data in Figure 5.2.4 and 5.2.5 have been calculated and the results can be found in tables 5.2.1 and 5.2.2. The left columns correspond to the sum of the mean effective areas for the simulated data for each of the different acrylic materials and divided by the same sum using regular gel pads (expressed in %). In addition, the second columns correspond to the same calculation as before, but each mean effective area has been weighed by the quantum efficiency at the corresponding wavelength. Finally, the last column represents a weighed sum in which the Cherenkov spectrum

[11] The absorption length of the optical coupler will not significantly affect the results as long as it is not set to a very low value, which is not the case for the one of ShinEtsu gel.

[12] That was simulated at 470 nm.

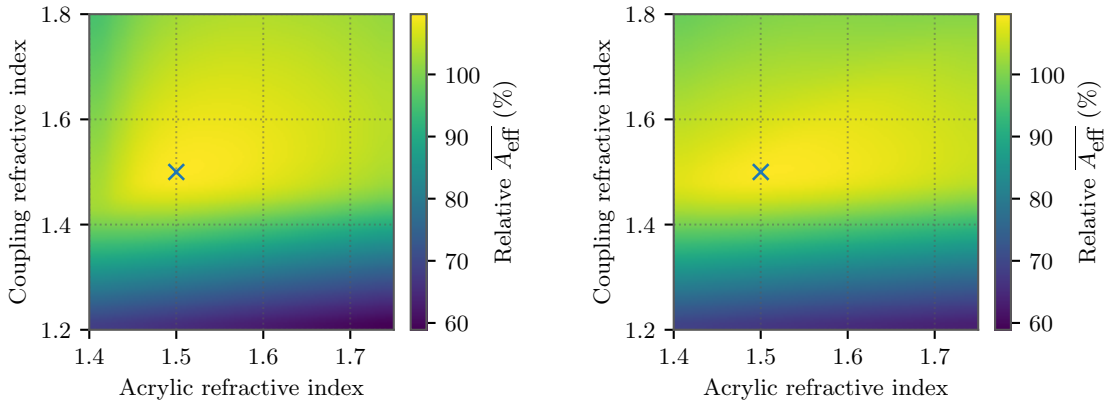

(a) Coupling thickness of 1 mm

(b) Coupling thickness of 5 mm

Figure 5.2.2: Mean effective area for the acrylic pad configuration as a function of the refractive indices of the acrylic and the coupling material. Values are expressed as a ratio (in percent) to the mean effective area of regular gel pads with the same geometry. The blue cross lies at the maximum value at a refractive index of 1.5 for both materials, which approximately matches that of the glass vessel material. Interpolations between simulated data has been used.

and the quantum efficiency have been taken into account. For this, the Frank-Tamm formula (eq. 2.3.2) is considered, which indicates, in an approximate manner, the number of photons produced in a given interval of wavelengths by Cherenkov radiation. The refractive index of ice can be approximated as a constant and thus eq. 2.3.2 results in a constant multiplied by the difference between the maximum and minimum light frequencies in the interval that is considered. Then, a Cherenkov-QE weighted sum can be obtained as such:

$$S_{\text{Cherenkov}}(\text{Material}) = \sum_{i=1}^{27} \left[\frac{\overline{A_{\text{eff}}}(\lambda_i) \cdot QE(\lambda_i) - \overline{A_{\text{eff}}}(\lambda_{i-1}) \cdot QE(\lambda_{i-1})}{2} \cdot \left(\frac{1}{\lambda_{i-1}} - \frac{1}{\lambda_i} \right) \right], \tag{5.2.1}$$

where $\lambda_0 = 300$ nm, $\lambda_{27} = 570$ nm and $\lambda_i - \lambda_{i-1} = 10$ nm. Moreover, $QE(\lambda)$ and $\overline{A_{\text{eff}}}(\lambda)$ correspond to the PMT quantum efficiency and the mean effective area of the corresponding material at wavelength λ. As a result, eq. 5.2.1 considers an average mean effective area that is weighted by the quantum efficiency in a given interval of wavelengths, and then it is multiplied by the factor involving the wavelengths from the Frank-Tamm formula. The final result, $S_{\text{Cherenkov}}$, is given by:

$$S_{\text{Cherenkov}} = \frac{S_{\text{Cherenkov}}(\text{Acrylic})}{S_{\text{Cherenkov}}(\text{Gel})} \cdot 100. \tag{5.2.2}$$

The further the source is, the flatter is the photon wavelength spectrum, and the QE only weighing is to be considered.

The performance of acrylic pads with gel as coupling material is only slightly worse compared to the performance of regular gel pads, with losses ranging from 2 % to slightly more than 6 % in the worst case. On the other hand, if a coupler with a refractive index of 1.5 is used, there are improvements for all the different acrylics ranging from 0.5 % in the worst case to 6.7 % in the best case.

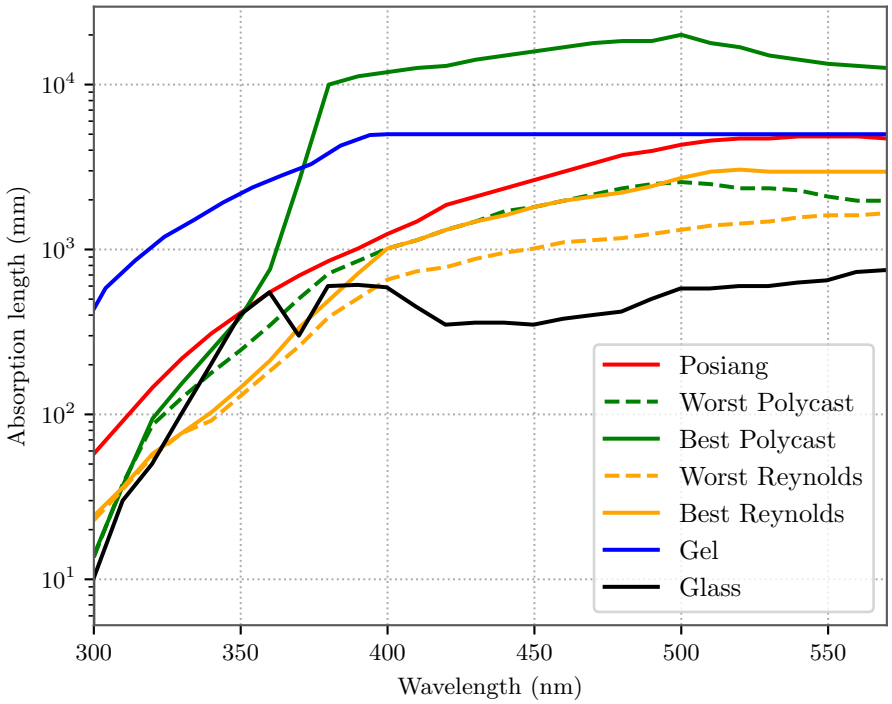

Figure 5.2.3: Absorption lengths of three acrylic materials: Posiang, Polycast and Reynolds [48] together with Vitrovex [44] glass and Shin-Etsu gel [45]. The upper and lower values given for Polycast and Reynolds materials are the result of uncertainties and actual variations in the absorption lengths.

Table 5.2.1: Sums and weighed sums for the different acrylic materials using Shin-Etsu gel as coupling. The values indicated are relative to the same weighed sums for regular gel pads. Explanation on text.

Material	Sum (%)	Sum with QE (%)	Sum with QE and Cherenkov (%)
Posiang	98.1210 ± 0.0021	98.1343 ± 0.0022	97.4022 ± 0.0024
Worst Polycast	96.4581 ± 0.0021	96.6894 ± 0.0022	95.405 ± 0.005
Best Polycast	97.8546 ± 0.0021	98.2501 ± 0.0022	97.1442 ± 0.0024
Worst Reynolds	94.6172 ± 0.0021	94.5445 ± 0.0022	92.6308 ± 0.0023
Best Reynolds	95.5012 ± 0.0021	95.4876 ± 0.0022	93.6089 ± 0.0023

Table 5.2.2: Sums and weighted sums for the different acrylic materials using a gel with a refractive index of 1.5 as coupling. The values indicated are relative to the same weighed sums for regular gel pads. Explanation on text.

Material	Sum (%)	Sum with QE (%)	Sum with QE and Cherenkov (%)
Posiang	106.7478 ± 0.0021	106.6976 ± 0.0022	105.6917 ± 0.0025
Worst Polycast	104.9399 ± 0.0021	105.1075 ± 0.0022	103.509 ± 0.006
Best Polycast	106.4315 ± 0.0021	106.7749 ± 0.0022	105.3699 ± 0.0025
Worst Reynolds	102.9387 ± 0.0021	102.7802 ± 0.0022	100.4958 ± 0.0024
Best Reynolds	103.8912 ± 0.0021	103.7955 ± 0.0022	101.5493 ± 0.0024

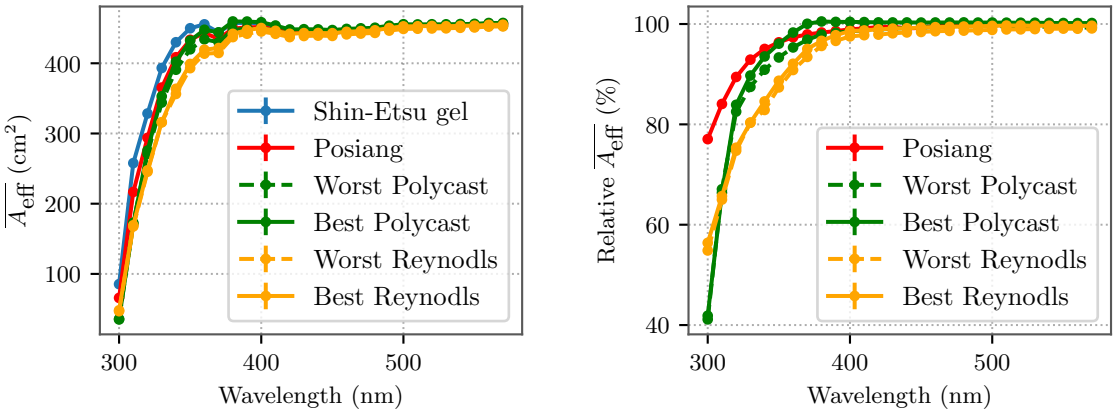

(a) Absolute values.

(b) Performance relative to regular gel pads.

Figure 5.2.4: Mean effective area as a function of the wavelength for different acrylic materials and regular gel pads. 1 mm thick ShinEtsu gel has been used as coupling material. **(a)**: Absolute values. Some of them overlap in the plot and cannot be distinguished. **(b)**: Values relative to regular gel pads performance. The simulated values were joined for clarity.

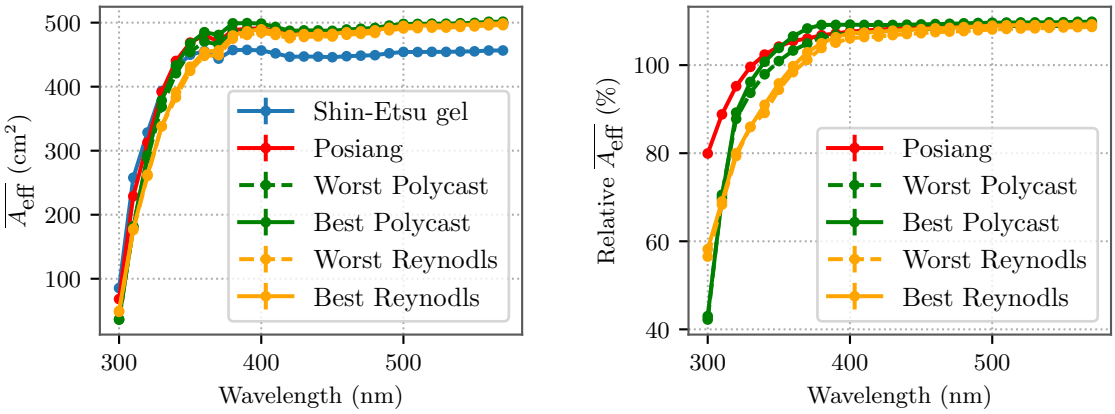

(a) Absolute values.

(b) Performance relative to regular gel pads.

Figure 5.2.5: Mean effective area as a function of the wavelength for different acrylic materials and regular gel pads. A hypothetical 1 mm thick gel with a refractive index of 1.5 has been used as coupling material.**(a)**: Absolute values. Some of them overlap in the plot and cannot be distinguished. **(b)**: Values relative to regular gel pads performance. The simulated values were joined for clarity.

5.3 In-situ shell pads simulations

The geometry resulting from the in-situ shell approach has been created in Geant4 using a shell material that surrounds the gel and has different optical properties to the latter, as can be seen in Figure 5.3.1. The volume of the total pad is the same as that of the precasted pads. Therefore, the thicker the shell, the thinner the gel and vice versa.

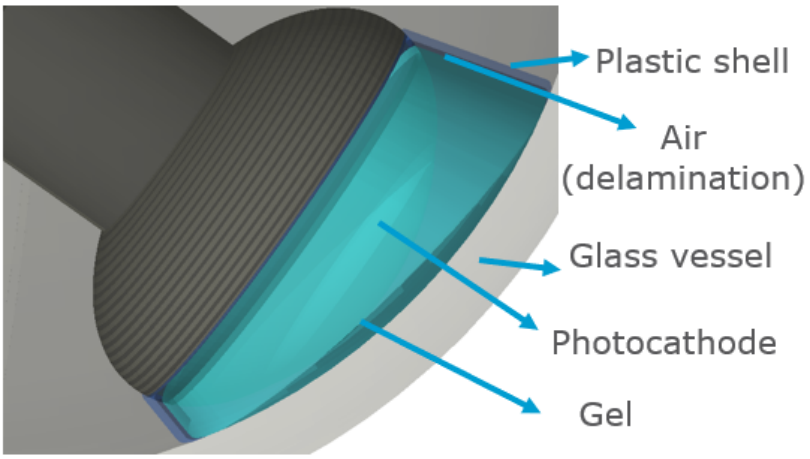

Figure 5.3.1: Geant4 geometry of the gel pads following in-situ pouring approach. A transparent plastic shell with its own optical properties covers the photocathode and the gel.

To study the impact of this approach on the sensitivity, the mean effective areas as a function of the thickness of the shell and its refractive index has been calculated and the results can be seen in Figure 5.3.2. The step size taken for the thickness was 1 mm whereas it was of 0.5 in the case of the refractive index. The values for the mean effective area are very similar in all the simulated combinations, with maximum variations of $\sim$ 1 %. It is found that the higher the refractive index of the shell, the worse the performance. One reason could be a poorer optical coupling between the shell and the gel inside it, resulting in reflections at their interface and thus photons being "lost". On the contrary, slight gains are observed if the refractive index is kept at 1.5 and the thickness is higher than 4 mm. As already stated in the last section, this is a refractive index that matches that of glass materials.

One of the major problems with this approach is to find a material for the shell that features a thermal expassion coefficient similar to that of the gel. Otherwise, delamination will occur and an air gap between the shell and the gel will arise. The effects of this delamination were naively simulated in Geant4 with an air layer of constant thickness placed between the shell and the gel, as it can be seen in Figure 5.3.1. The mean effective area as a function of the thickness of the air gap can be seen in figure 5.3.3a, where a 2 mm thick shell with a refraction index of 1.5 was used. It is observed that the thicker the air gap, the smaller the mean effective area, which drops by almost 5 % for a thickness of 3 mm. This can be attributed to two main reasons: First, the thicker the air, the smaller the final volume of the gel pad. This has consequences on the final performance, as some regions of the photocathode are not covered by either the gel or the acrylic/plastic shell and the surface area on which reflections can occur is reduced. To illustrate this, in Figure 5.3.3b the mean effective area as a function of the reduction of the gel pad diameter for regular gel pads is shown, where the losses range from 0.5 % at 1 mm to 4 % at 4 mm. Secondly, air has a much lower refractive index than gel ($n_{air} \sim$ 1 vs. $n_{gel} \sim$ 1.4), so there are total internal reflections at the interface between the shell and the air from the delamination, which has the same result as having an even more reduced gel pad. It has to be stressed again that in a real case, the air gap resulting from delamination is not as uniform as the one naively simulated. Yet, these simulations can give an idea of possible consequences.

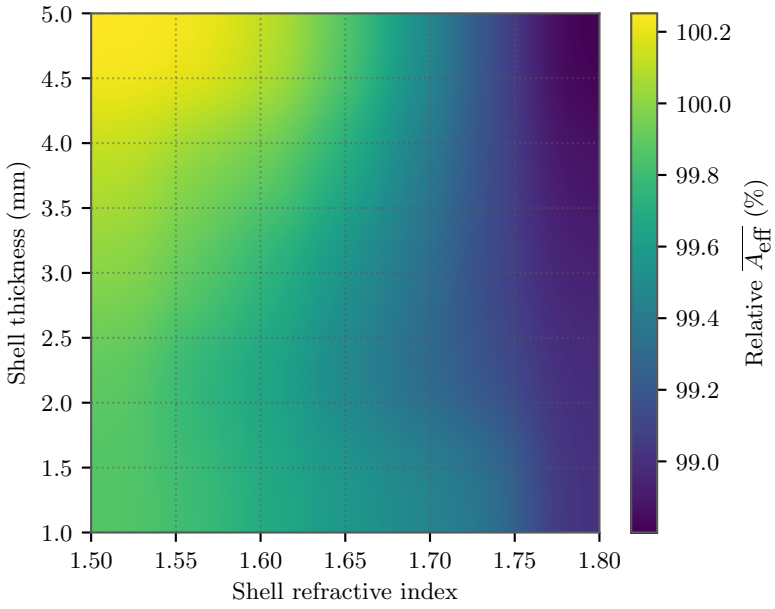

Figure 5.3.2: Mean effective area for shell pads as a function of the refractive index of the shell and its thickness. The values are expressed in ratio to that of the regular gel pads (in percent). Interpolation between simulated data has been performed.

Table 5.3.1: Sums and weighted sums for different pad configurations following the in-situ pouring approach. The values indicated are relative to the same weighed sums for regular gel pads. Explanation on text.

Material	Sum (%) ($\pm$ 0.0021 %)	Sum with QE (%) ($\pm$ 0.0022 %)	Sum with QE and Cherenkov (%) ($\pm$ 0.0024 %)
Shell 2 mm	99.7635	99.7676	99.7052
Shell 5 mm	99.8985	99.8996	99.7177
Shell 2 mm air 1 mm	98.1711	98.1662	98.1351

For the sake of completeness, the mean effective area as a function of the wavelength has been calculated and the results are illustrated in Figure 5.3.4. In particular, three configurations have been considered: a 2 mm thick shell, a 5 mm thick shell and a 2 mm thick shell with 1 mm thick of air delamination. As for the shell material, any acrylic can be a potential candidate. For this reason, the Posiang acrylic presented in the previous section has been chosen without loss of generality. For all configurations, the mean effective areas are a few percent lower than those of regular gel pads at 300 nm, especially true for the 5 mm thick case. This can be attributed to the shorter absorption length of the acrylic at these energies. On the contrary, they provide more similar results at higher wavelengths, as expected from the results of Figure 5.3.2.

For a global comparison, the table 5.3.1 provides the results of the sums and weighed sums for the same calculations that were performed in the last section using the data in the figure 5.3.4a. It can be concluded that this approach provides very similar results to regular gel pads, with losses lower than 0.3 % with no delamination and up to 2 % for moderate delamination.

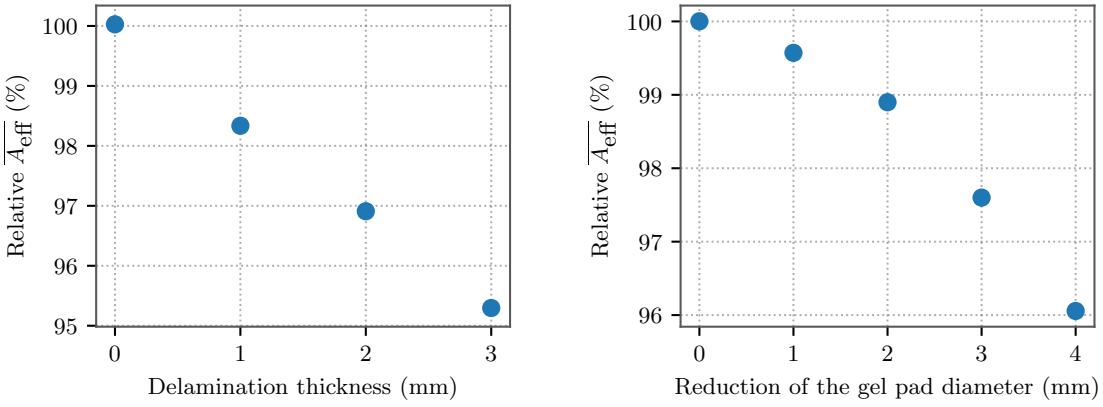

(a) **(b)**

Figure 5.3.3: **(a)**: Mean effective area as a function of the delamination thickness for pads following the in-situ approach. The values are given in ratio to the absence of delamination (in %). **(b)**: Mean effective area for regular gel pads as a function of the reduction of its diameter. The values are given relative to the performance of full gel pads (in %). Error bars cannot be seen.

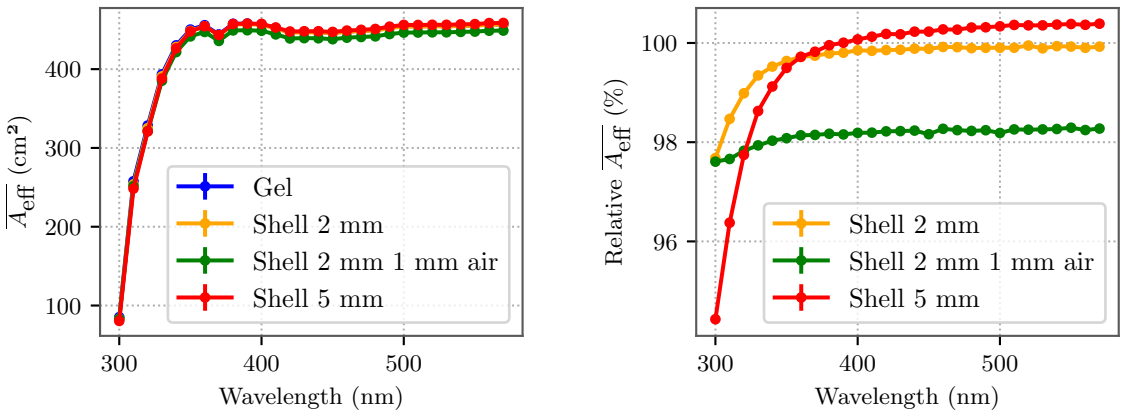

(a) Absolute values.

(b) Performance relative to regular gel pads.

Figure 5.3.4: Mean effective area as a function of the wavelength for different pad configurations following the in-situ pouring approach. **(a)**: Absolute values. Some of them overlap in the plot and cannot be distinguished. **(b)**: Values relative to regular gel pads performance. The simulated values were joined for clarity.

5.4 Current status

The provided simulations have shown that all considered approaches can provide similar performance to regular gel pads and even improve the module mean effective area for ideally matched refractive indexes. Nevertheless, the acrylic pad approach was eventually discarded as the coefficient of thermal expansion is different to that of the gel, resulting in delamination from the coupling material at low temperatures. The same behavior was observed for in-situ shells, ultimately rendering both methods futile. Expanding on-situ casting, the working group of the University of Wisconsin-Madison pursues a hybrid approach where the shell consists of a thin rim of gel that is casted in an external mould whereas the leftover cavity is filled during half-module assembly [39]. On the other side, the groups at Münster and Chiba Universities improve on the original concept of precasted pads, as potential problems in the bond between the pad and the vessel can be solved by standardizing the procedures and using partly cured gel as well as caulking to combat leakages. Hence, the two methods currently being pursued provide the gel pads with the same optical properties as the original concept. At the time of writing this thesis, the development is still progresses for which reason a definite approach has not been selected yet.

In any case, the simulation studies presented in this chapter suggest the LOMs module performance in terms of mean effective area is largely independent of the gel pad casting approach when considering realistic values.[13]

[13] That is acrylic pads having a refractive index of 1.5 and using gel (n$\sim$1.4) as optical coupler, since a coupler with refractive index of 1.5 is not achievable. And using an equal acrylic material for the in-situ shell method, since finding a plastic material with the same thermal expansion coefficient as gel is difficult.

6 Studies on gel pad geometry

In this chapter, different aspects of the geometry of gel pads and the LOM module will be discussed, based on Geant4 simulations. First, the sensitivities of three different gel pad shapes will be compared. Then, the effect of roughness on the side of the gel pad on the performance will be studied. Finally, the implementation in Geant4 of latest LOM-16 configuration as of March 2022 will be presented.

6.1 Gel pad shape

Gel pads make use of reflections at the interface between gel ($n_{gel} \sim 1.4$) and the air that surrounds it ($n_{air} \sim 1$) to increase the sensitive area of the module. Especially important are total internal reflections, which can occur with a minimum incident angle (measured from the normal at the interface) of 45.4 degrees and have an efficiency of 100 % in contrast to those originating from reflective coating materials. Due to the nature of reflections, the geometry of the gel pad plays a fundamental role for a good performance. In this section, three different shapes for the gel pads are going to be discussed based on results from mean effective areas. These are: conical shapes, ellipsoidal shapes and Winston cones.

6.1.1 Conical and ellipsoidal gel pads

Conical and ellipsoidal shapes can be easily implemented in Geant4 by means of the classes G4Ellipsoid (ellipsoidal shape) and G4Cons (conical shape). Once they are created, they must be cut by means of boolean operations with the PMT to avoid overlaps. The final result can be seen in Figure 6.1.1b (conical shape) and 6.1.1a (ellipsoidal shape).

The parameters that characterise the ellipsoidal shape are the semi-major axis a and the semi-minor axis b, that can be observed in Figure 6.1.1a. On the other side, the conical shape is defined by its semi-opening angle θ. Both gel pad geometries were implemented in the Geant4 code of the LOM in the scope of the master thesis [40], where optimisation studies as a function of the different shapes for the polar and equatorial positions[14] were also carried out. In this thesis, these studies are going to be repeated implementing a further constraint, i.e. gel pads are not allowed to overlap. In order to achieve this, the results from [40] will be used as a starting point.

Overlaps can occur in two different situations: between neighbouring gel-pads (either polar-polar or equatorial-polar) and between equatorial gel pads and a nearby PMT in the polar position. The first situation apply to both geometries, while the second one is only found in ellipsoidal gel pads.

Concerning conical shapes, in [40] a maximum of the mean effective area as a function of the polar and equatorial semi-opening angles was found at 76^o and 17^o for the polar and equatorial semi-opening angle, respectively . This was the only maximum and no other local maximum was observed, i.e. the values increase monotonically towards the maximum. This fact motivated looking in regions as close as possible to that optimum configuration. The mean effective area as a function of both semi-opening angles was simulated, and it is shown in Figure 6.1.2, where the red shaded region represents overlapping configurations. The maximum polar angle that was simulated is 42 ^{o}, where overlaps between neighbouring polar gel pads start to occur. In general, it is observed that the larger the openings, the larger the mean effective area. For this reason, the optimal configurations are found

[14] These positions were explained in section 4.2

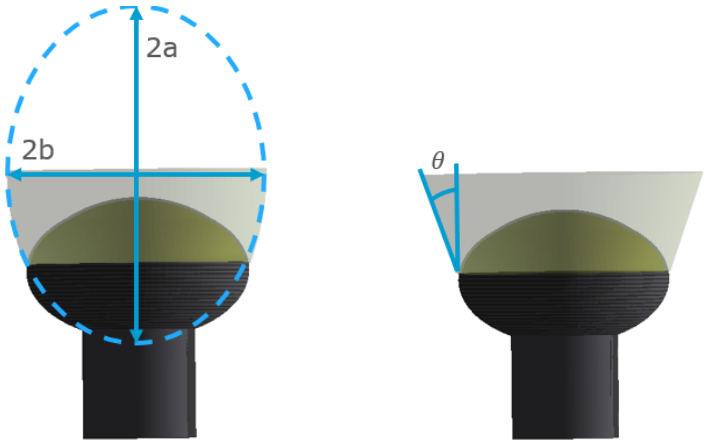

(a) Ellipsoidal gel pad.

(b) Conical gel pad.

Figure 6.1.1: Conical and ellipsoidal gel pads implemented in Geant4. The ellipsoidal gel pad ((**a**)) is defined by its semi-axes a and b, whereas the conical shape ((**b**)) is described by its semi-opening angle θ.

at the overlapping border. More precisely, values ranging from (448.69 $\pm$ 0.13) cm^2 to (448.00 $\pm$ 0.13) cm^2 for the mean effective areas are found along this boundary in the region from 42^o to 30^o for the polar semi-opening angles, with the highest values for the larger polar openings, while decreasing for smaller ones.

The optimisation of the ellipsoidal shape involves four parameters and is, therefore more complex. The first step was to fix the polar ones and find an optimum configuration for the equatorial values. In [40], an optimum value was found for a = 64 mm and b = 61 mm. Such a configuration cannot be used since it presents an overlap between the gel pad and the PMTs in the polar position. To deal with it, the semi-axis b was slightly lowered while maintaining a within the same range. In particular, there is no longer an overlap for b = 58 mm while a can be as small as 61 mm. The mean effective area as a function of the semi-axes a and b for the equatorial gel pads is shown in Figure 6.1.3a. The highest values arise for larger b and smaller a, with small differences which coincide within the errors in the range of 61 to 67 mm for a while b is 58 mm.

Without loss of generality, the equatorial parameters were eventually set to a = 64 mm and b = 58 mm in order to optimise the polar ones. In [40], the best configuration for polar ellipsoidal pads was found at a = 54 mm and b = 135 mm, where there is an overlap between polar gel pads. Furthermore, the results provided suggest that the semi-axis b should be as large as possible up to a value of 135 mm, while a should preferably be smaller than 60 mm. In Figure 6.1.3b, the mean effective area as a function of both semi-axes for polar gel pads is provided, where a is in the range 35-60 mm and b belongs to 73-78 mm. Similar to the conical case, the shaded region represents configurations that feature overlap. The values for mean effective areas for all the configurations on the boundary of that region are similar with values $\sim$ 453 cm^2, nevertheless, the best are found for b equal to 74 and 75 mm with a as small as possible (43 mm and 39 mm respectively), where the curvature at the side and the apertures are maximal.

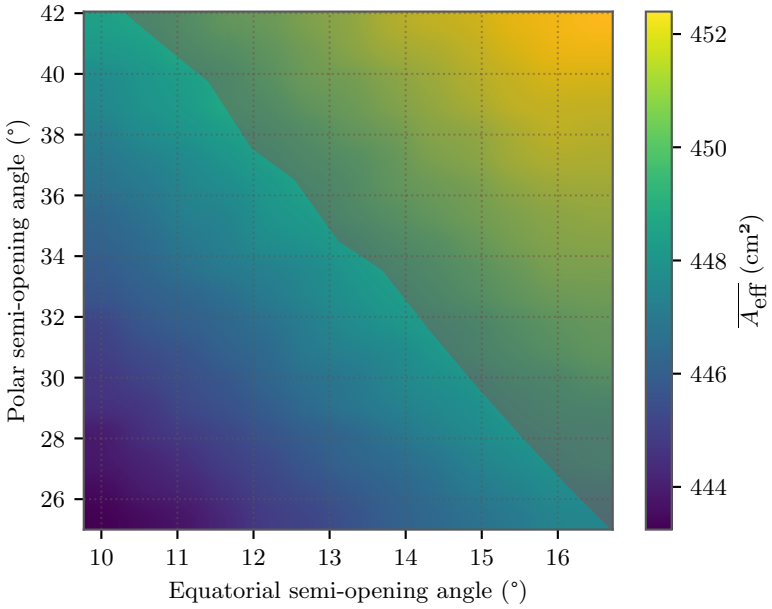

Figure 6.1.2: Mean effective area for gel pads with conical shape as a function of the polar and equatorial semi-opening angles. The red shaded region corresponds to overlapping configurations. Simulation results were interpolated for clarity.

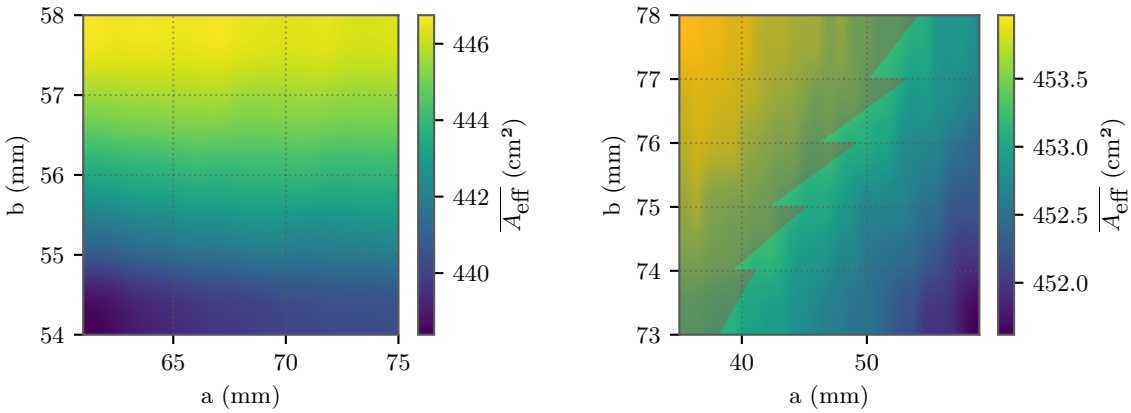

(a) Equatorial gel pads.

(b) Polar gel pads.

Figure 6.1.3: Mean effective area for ellipsoidal gel pads as a function of the semi-axes a and b for equatorial **(a)** and polar **(b)** positions. The red shaded region represents overlapping configurations. Simulation results were interpolated for clarity.

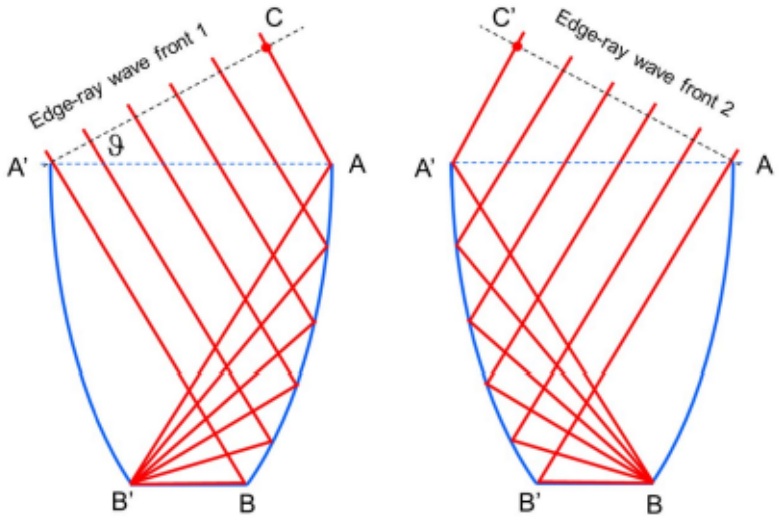

Figure 6.1.4: Operational principle and definition of Winston cones. Explanation on the text. Image taken from [50].

6.1.2 Winston cone gel pads

In order to find a better geometry, Winston cones, also known as *Compound Parabolic Concentrators* (CPCs) [49], were considered. They arose in an attempt to find an ideal 2D concentrator, i.e. a system that is able to transport energy (light) from an entry aperture to an exit one that has a smaller size. This is achieved by fulfilling the so-called edge-ray principle [49]. It states that, given that the extreme rays at the entry of an optical device (with no light generation or loss) emerge at the extreme positions at the exit aperture, all rays within these extreme ones will also emerge anywhere at the exit. By "extreme positions" both place and direction are meant. With this in mind, 2D Winston cones are created by using two reflective parabolic sections as it is shown in Figure 6.1.4: one A'B' with focus on B and another AB with focus on B', being AA' the entry aperture and BB' the exit one. Then, the edge-ray principle is fulfilled for the extreme rays A'B, CA on Figure 6.1.4 (left) and C'A', AB' on Figure 6.1.4 (right), thanks to the properties of the parabola. As a result, Winston cones are ideal concentrators in the sense that any incoming ray at the entry aperture at an angle less or equal than the maximum acceptance (or design) angle (θ on Figure 6.1.4) will emerge at the exit aperture.

Due to the geometrical properties of the parabola, CA+AB' is equal to A'B+BB'. Moreover, CA/AA' = sin(θ) and A'B is equal to AB' due to symmetry. Consequently, the size of the entry aperture of Winston cones is determined by the size of the exit one and the design angle as:

$$CA + AB' = A'B + BB' \rightarrow AA'\sin(\theta) = BB', \tag{6.1.1}$$

which corresponds with the so-called maximum concentration ratio for ideal concentrators [49].

An analytical description of the Winston cone can be provided based on the parameters shown in Figure 6.1.5:

$$r = \frac{2f\sin(\phi - \theta_{\max})}{1 - \cos(\phi) - a'}, \qquad z = \frac{2f\cos(\phi - \theta_{\max})}{1 - \cos\phi}, \tag{6.1.2}$$

where $\theta_{\max}$ is the design angle, $\phi \in [2\theta_{\max}, \theta_{\max} + \pi/2]$, a' is half of the size of the exit aperture and f is the focal length of the parabola:

$$f = a'(1 + \sin(\theta_{max})). \tag{6.1.3}$$

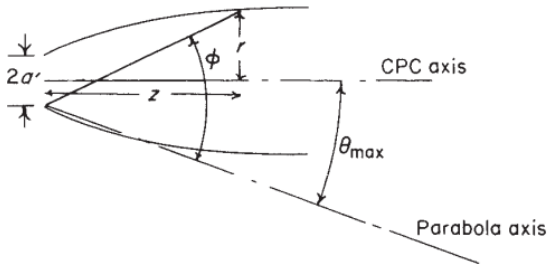

Figure 6.1.5: Parameters that describe a Winston cone (CPC). θ_{max} corresponds with the maximum acceptance (or design) angle and 2a' is the diameter of the exit aperture. Image taken from [49].

In addition to that, the length of the Winston cone, L, is determined by the size of the exit aperture and the design angle as:

$$L = \frac{\text{a} + \text{a}'}{2 + \tan(\theta_{\text{max}})}, \tag{6.1.4}$$

being a half of the size of the entry aperture, a=a'/sin(θ_{max}).

Gel pads are made of dielectric material, which affects the overall angular acceptance. In particular, a Winston cone with a design angle of θ_{design}, will have a different maximum acceptance angle $\theta_{\text{acceptance}}$ in accordance with Snell's law:

$$n_1 \cdot \sin(\theta_{\text{design}}) = n_2 \cdot \sin(\theta_{\text{acceptance}}), \tag{6.1.5}$$

where n_2 is the refractive index of the material at the entry, Vitrovex glass in our case, and n_1 is the refractive index of the gel.

Gel pads are 3D objects, so in a more realistic case, a 3D Winston cone is obtained by taking the revolution about its symmetry axis. However, they are no longer ideal concentrators, as the requirements for this only apply to meridian rays, i.e. those crossing the Winston cone's axis of symmetry. Nevertheless, 3D Winston cones still provide a nearly-ideal performance [49].

In order to implement Winston cones in Geant4, there is no such a class that allows to do it directly. To this end, they are approximately created using G4Polycones [41]. To create an object with this class, z-positions and respective radii must be provided. Then, planes are created at the selected z-positions by revolution of the respective radii and all the different planes are joined creating a single compact solid. Therefore, equations 6.1.2 and 6.1.3 can be used to parametrise the solid and create such planes. The final result can be seen in Figure 6.1.7, where 200 planes were used. As a direct consequence of eq. 6.1.4 and the maximum concentration ratio, it can be noted that given a fixed exit aperture, which in our case is the photocathode, the smaller the design angle, the longer the Winston cone will be and the larger the entry aperture will be.

Figure 6.1.6: LOM module with Winston cone gel pads. Once implemented the gel pads are cut and asymmetrical.

One of the main concerns regarding Winston cone gel pads is that, due to their size, once implemented in the module they will be cut off and asymmetrical (Figure 6.1.6). For this reason, they cannot provide ideal performance.[15]

[15] More information about truncated Winston cones and dielectric filled ones can be found on [49].

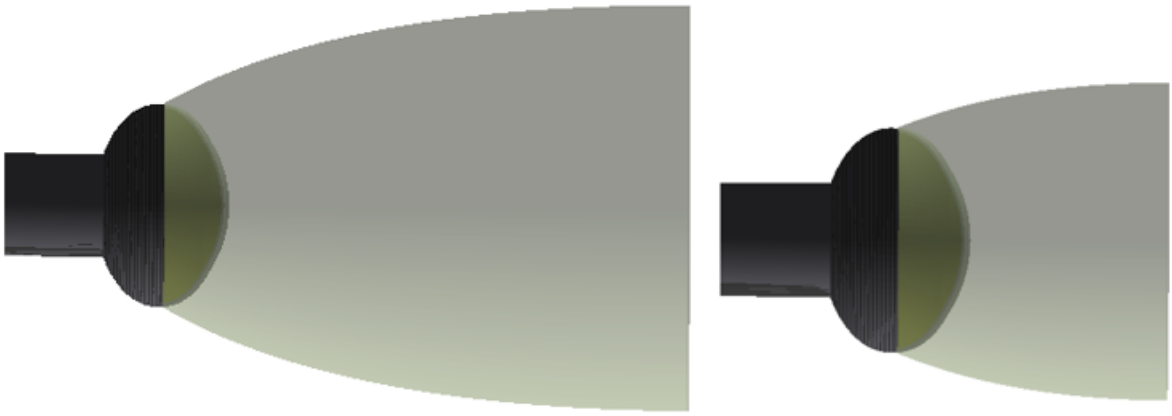

(a) (b)

Figure 6.1.7: Winston cone gel pads in Geant4. (a) Design angle of 30°. (b) Design angle of 45°.

The mean effective area as a function of the design angle of Winston cones for polar and equatorial positions can be observed in Figure 6.1.8. At equatorial design angles lower than 50° there are overlaps between the equatorial Winston cones and the nearest PMT in the polar position. Hence, it is the smallest equatorial design angle that was simulated. The minimum polar design angle simulated was one degree, and no overlap between polar gel pads was observed. Even though larger gel pads are more cut and asymmetric than smaller ones, the results indicate that the largest mean effective areas arise for the configurations with smaller design angles i.e. with larger gel pads, with values $\sim 452\,\mathrm{cm}^2$.

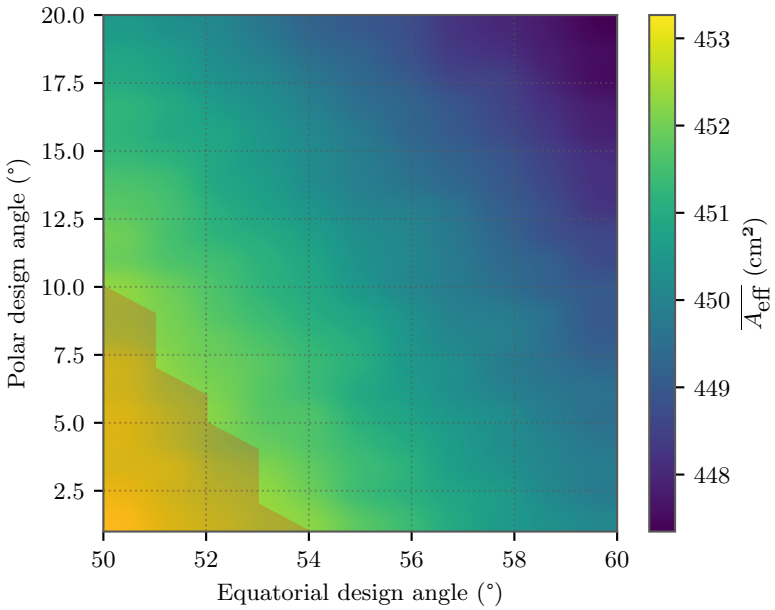

Figure 6.1.8: Mean effective area for gel pads with Winston cone shape as a function of polar and equatorial design angles. The red shaded region corresponds to overlapping configurations. Simulation results were interpolated for clarity.

In order to better understand this issue, the effective areas for an individual polar PMT with Winston cones with design angles of 20° and one degree can be seen on Figures 6.1.9b and 6.1.9a,

respectively. [16] Besides, the substraction of the values from both plots is shown in Figure 6.1.9c. The brightest regions that can be distinguished in the three figures correspond to directions of the plane waves of photons that have little tilt with respect to the orientation of the polar PMT. Despite both Winston cones being designed for collection of photons with zero tilt, the one-degree Winston cone feature larger effective areas for these directions, as more photons are accessible due to its larger size. On the other hand, the 20-degree Winston cone outperforms the one-degree cone in the vicinity for slightly larger incidence angles. It can be seen in the dark shadow around the brightest spot in Figure 6.1.9c, and it is consistent with the principle of operation of Winston cones. The reason this shadow is asymmetric and shifted southwards is that the polar gel pads are more cut off on the side closer to the equator than at the poles. Nonetheless, the one-degree Winston cone provides a better efficiency again at even higher incidence angles, due to the additional reflections in its larger volume; and resulting overall in a slightly larger mean effective area.

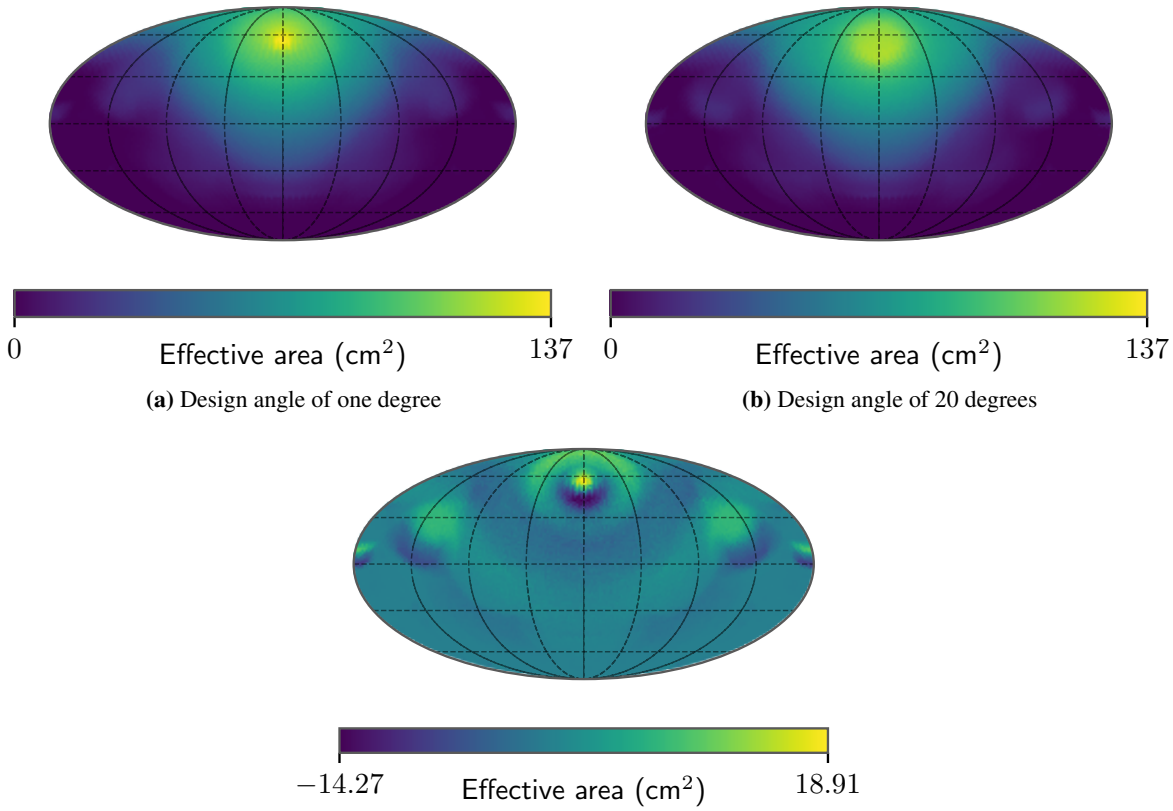

(a) Design angle of one degree

(b) Design angle of 20 degrees

(c) Difference between the above plots.

Figure 6.1.9: Effective areas for single a single polar PMT with Winston cone gel pads. The brightest spot corresponds to the directions where the plane waves impinge on the PMT with little tilt.

6.1.3 Comparison of different shapes

A comparison of the effective areas for the previously described shapes for gel pads: ellipsoidal, Winston cone and conical; is shown in Figure 6.1.10a, 6.1.10b and 6.1.10c, respectively, where the optimal configurations are simulated. The accompanying mean effective areas are listed in table 6.1.1, along with the simulation parameters that were used for their calculation. All three geometry shapes

[16] All the other PMTs were also present in the calculation so as to take into account their shadow.

agree in providing maximum efficiencies for the largest possible openings, with certain preference for polar gel pads. However, the apertures are not the only determining factor as there is also dependence on the shape of the gel pads. This is evident in the different patterns of effective areas shown in Figure 6.1.10 and, in general, in the different mean effective areas they provide. Overall, however, the differences between the best and worst geometries (ellipse and cones respectively) hardly exceed 1 %.

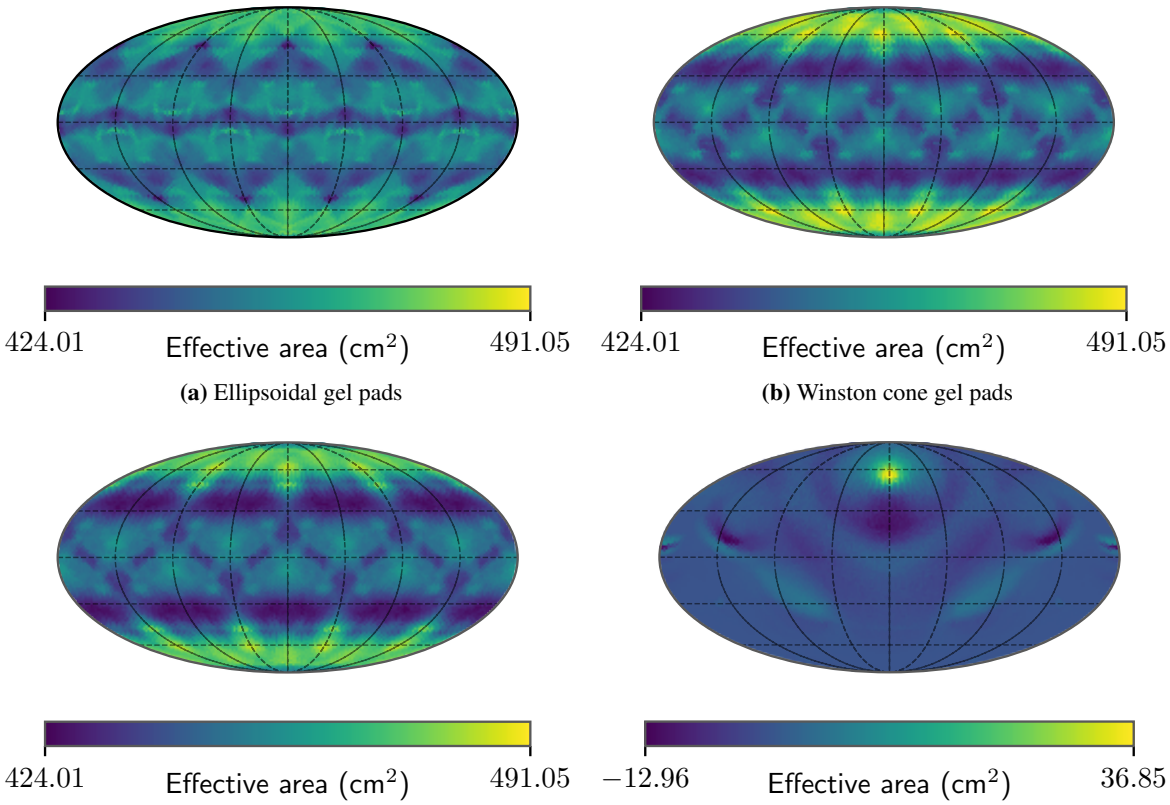

(a) Ellipsoidal gel pads

(b) Winston cone gel pads

(c) Conical gel pads

(d) Difference for polar PMT with Winston cones and with ellipsoidal gel pads.

Figure 6.1.10: (a)-(c): Effective areas for the optimal configurations of the different shapes that were considered. **(d)**: Differences between the effective areas for a single polar PMT with a Winston cone gel pad of a design angle of one degree and an optimal polar ellipsoidal gel pad (the average is -0.1320 $\pm$ 0.0005 cm^2).

In Figure 6.1.11, the effective areas for the three different geometries are given as a function of the zenith impact angle and averaged over the azimuth one. All three perform best at polar incidence angles, which is consistent with the polar gel pads having large apertures, as they contribute the most in these directions. In addition, ellipsoidal gel pads have the most homogeneous angular acceptance, while Winston cones have the least. More precisely, the standard deviation of the simulated effective areas with respect to the mean is $\sim 2.2\,\%$[17] for ellipsoidal gel pads and $\sim 3.4\,\%$ for Winston cones, whereas it is of $\sim 3.1\,\%$ for regular cones.[18]

To answer the question why ellipsoidal gel pads outperform Winston cone shaped gel pads, Figure 6.1.10d is considered. It shows the differences in effective area for all directions that were simulated

[17] The errors of the effective areas are less than 0.05 %.

[18] The homogeneity can be improved in all cases, especially for Winston cones and regular cones, if the polar openings are slightly reduced in favor of the equatorial ones. It would affect the final mean effective areas by less than 1 %, according to Figure 6.1.8 and 6.1.2.

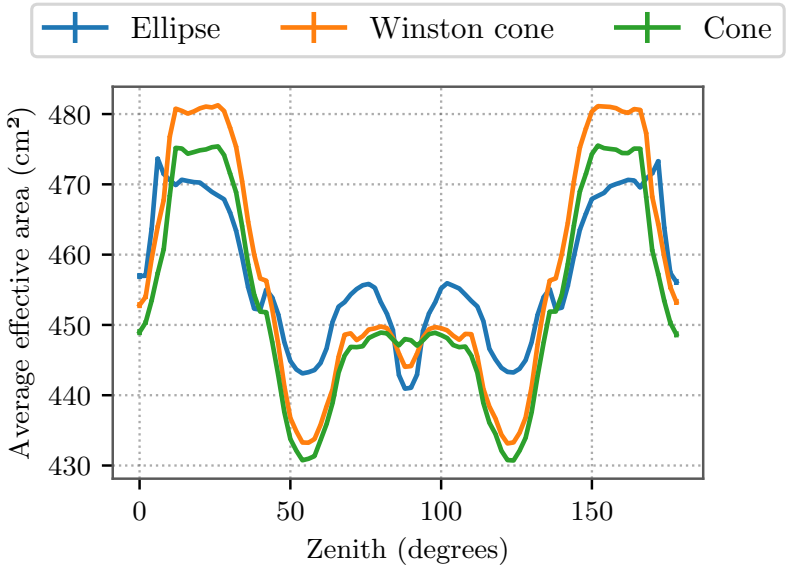

Figure 6.1.11: Effective areas for the three different shapes that were considered as a function of the zenith impact angle and averaged over the azimuth one.

between a polar PMT with a Winston cone gel pad of one degree design angle and a polar PMT with an optimal ellipsoidal gel pad. The Winston cone shape clearly outperforms the ellipsoidal gel pad in the observable bright spot, which corresponds to directions that target the PMT with little tilt with respect to its normal. This is in accordance with the operating principle of the Winston cones, which leads to a very inhomogeneous angular acceptance. Ellipsoidal gel pads, however, provide a more homogeneous acceptance and, a slightly larger mean effective area overall, thus resulting in a better approach. [19]

Eventually, a conical gel pad model was adopted, as it has been shown that there is not much difference in efficiency with the other geometries and they are the easiest to produce.

Table 6.1.1: Values of optimal mean effective areas and their parameters for the different shapes that were considered: ellipsoidal, Winston cones and cones. P. and Eq. stand for polar and equatorial, respectively.

Shape	Ellipsoidal	Conical	Winston cone
$\overline{A_{eff}}$ (cm^2)	453.291 ± 0.07	448.69 ± 0.13	452.08 ± 0.13
Parameters	P. semi-axis a = 42 mm P. semi-axis b = 74 mm Eq. semi-axis a = 64 mm Eq. semi-axis b = 58 mm	P. opening = 38 ° Eq. opening = 12 °	P. design = 6 ° Eq. design = 52 °

6.2 Gel pad roughness

If not specified, the interface between two dielectric mediums in Geant4 is by default perfectly smooth. However, gel pads may have a certain degree of roughness, especially on the side. Therefore, the impact on performance shall be assessed.

[19] Equatorial gel pads of both kinds provide the same value within the errors.

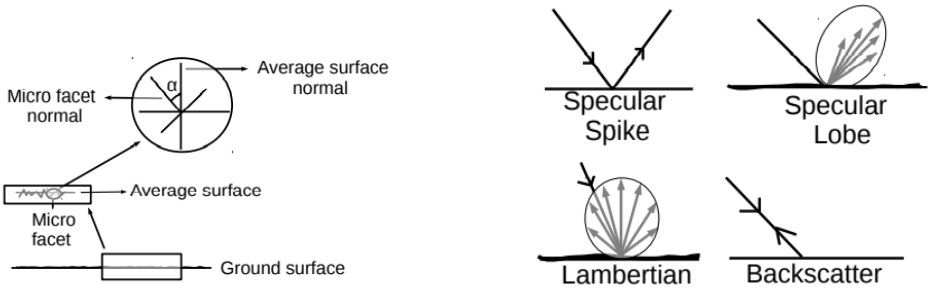

Figure 6.2.1: **(a)**: Roughness is implemented by the Unified model by dividing the surface into micro facets whose normal is different to that of the average. **(b)**: Four different kind of reflections that have to be specified within the Unified model. Images taken from [51].

Surfaces in Geant4 can be defined in two ways [41]: either by a *logical skin*, i.e. the surface that covers an entire solid; or the contact surface between two solids can be selected by means of a *border surface*. Optical boundary properties can then be assigned to the surfaces via the G4OpticalSurface class, where, among other functions, the physical models to be used can be selected and a *material properties table* can be provided.

In the scope of this thesis, only the *Unified* model will be considered. In order to implement roughness, the finish must be set to *ground*. As a result, the surface is split into micro-facets as can be seen in Figure 6.2.1a. When a photon encounters the surface, first, a micro-facet direction is randomly created following a Gaussian distribution with standard deviation σ_α. Then, Snell's law is applied and, if the result is a reflection, one has to select between four types by assigning their probabilities. These four kinds of reflections (see Figure 6.2.1b)) are:

- **Specular spike**: Reflections about the average normal of the surface (equal result as if no roughness was applied for reflections).
- **Specular lobe**: Reflections about the normal of a micro-facet.
- **Lambertian**: Diffuse reflection. It is set by default.
- **Backscatter**

In our case, a border surface was created between the side of the gel pad and the air inside the module. [20] Then, the mean effective area as a function of σ_α, which is the input parameter (given in radians), was simulated and the results are in Figure 6.2.2 for the four different kinds of reflections (each one with 100 % probability). The simulations were done for gel-pads with the optimal conical shape, and results are given relative to the mean effective area for the same shape with no roughness. As expected, for $\sigma_\alpha = 0$, both specular lobe and specular spike provide the same mean effective area as a conical gel pad with no roughness. However, as the roughness increases, the losses are much higher for the specular lobe than in the case of the specular spike. The reason is specular spike considers only differences on the refractions, whereas specular lobe takes into account reflections as well. As for lambertian and backscatter, there are losses even without roughness implemented. The backscatter presents a 15 % drop for $\sigma_\alpha = 0$, given by the absolute lack of gain from reflections on the gel pads. In contrast to that, the losses for lambertian range from slightly more than 4 % for no roughness to less than 6.5 % for extremely rough surfaces ($\sigma_\alpha > 2\pi$). It must be remarked that for very rough surfaces, it is possible that a photon undergoes several boundary interactions within the same process [41].

[20] Border surfaces are ordered. That is, it is important to define it in both directions: Gel-Air and Air-Gel.

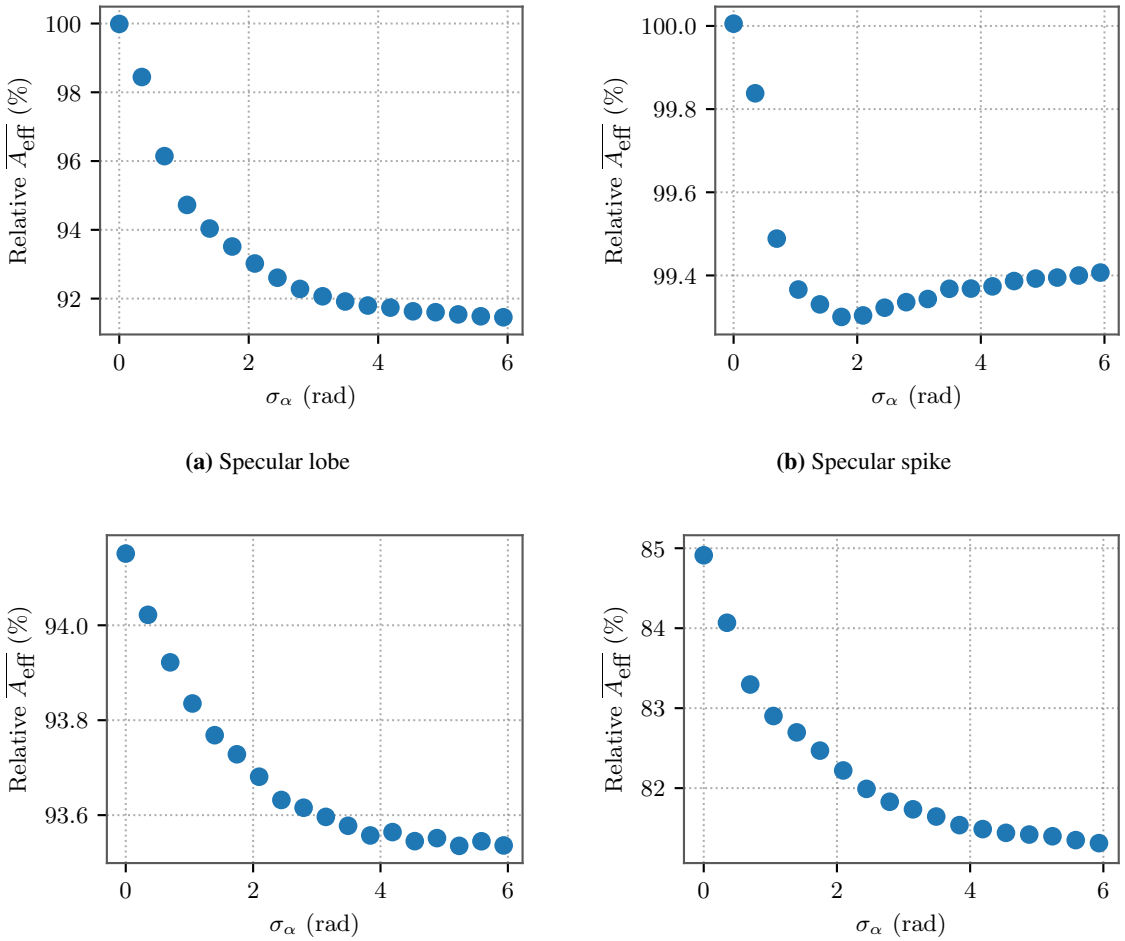

(a) Specular lobe

(b) Specular spike

(c) Lambertian

(d) Backscattering

Figure 6.2.2: Mean effective areas as a function of σ_α for different reflections. The values are given with respect to the mean effective area of conical gel pads with no roughness. Error bars cannot be seen.

Experimental studies on gel pads are needed, so that both the type(s) of reflection(s) and the corresponding σ_α value can be properly implemented. Nonetheless, a very likely configuration is one with specular lobe reflections and a σ_α lower than 0.75 radians, resulting in losses below $4\,\%$.

6.3 Simulations for the latest LOM-16 in Geant4

The baseline design of the LOM has undergone some modifications with respect to the previously presented implemented by [40]. The implementation in Geant4 of the new geometry is shown, together with the old one, in Figure 6.3.1b and 6.3.1a, respectively, and it corresponds to the latest CAD version of the LOM-16 module created by the IceCube collaboration. The main difference corresponds to the PMT distribution, which is now symmetric in both hemispheres of the module. This modification was necessary in order to have more space to place the electronic devices of the module, such as the mini-main boards that can be seen in Figure 6.3.1c. Gel pads feature a conical geometry that was justified in the previous section but their openings are changed. The constraint imposed in section 6.1 did not allow overlaps among them or with neighbour PMTs. However, overlaps with the penetrator cable must also be taken into account, which leads to reduced openings. In order to deal

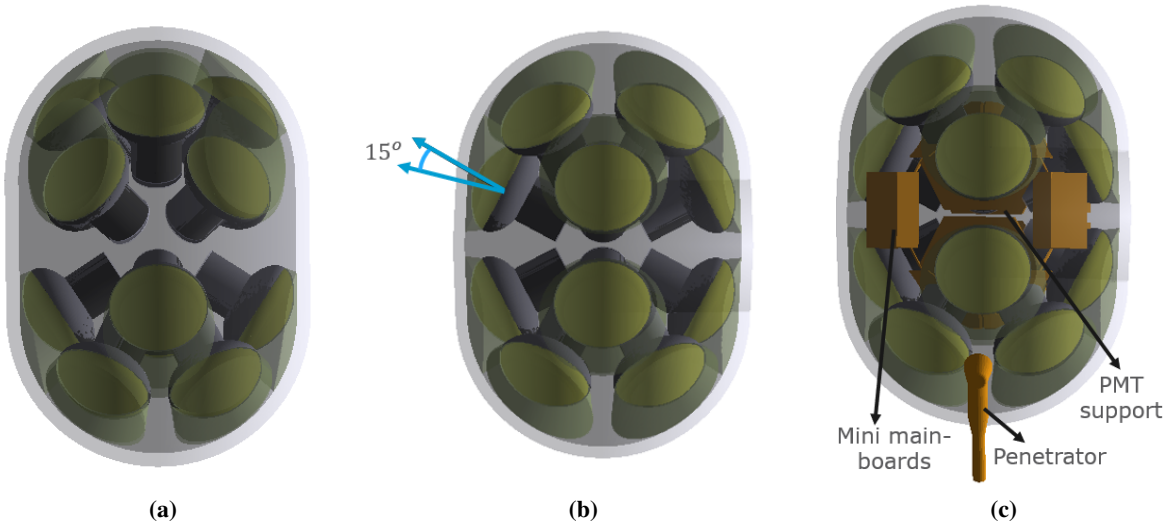

Figure 6.3.1: Geometry representations from Geant4: **(a)** Old geometry with conical gel pads. Semi-openings from table 6.1.1. **(b)** New geometry. Polar and equatorial semi-opening angles are 30 and 22 degrees respectively. **(c)** New geometry with penetrator cable, mini main-boards and PMT supporting structure.

with it, equatorial gel pads axis are tilted with respect to the PMT axis (see figure 6.3.1b), which allows an equatorial semi-opening angle of 22°, whereas the polar one is set at 30°. A regular cone with circular base can no longer fit into the (circular) photocathode when it is inclined. As a result, tilted gel pads were approximately created using cones with an ellipsoidal base provided by the class G4EllipticalCone. [21]

Apart from what is mentioned above, the LOM code has been implemented within a new Geant4 framework created by our working group. This includes: a new version of Geant4 (10.7 vs. 10.2), an update of the PMT dimensions and all the materials, and a more precise definition of the glass vessel. The latter was previously created by the union of a cylindrical body and two semi-spheres, one at each pole; while the current vessel is slightly wider at the equator than in the region near the poles, where it is also joined with two semi-spheres.

The values of the mean effective areas for the different geometries that appear on Figure 6.3.1 are shown on table 6.3.1, while the effective area plots can be seen on Figure 6.3.3. In this case, the wavelength that was studied is 400 nm. The old geometry was simulated within the new framework, and it can be noted that it presents a sensitivity value that is more than 5 % higher than the one from table 6.1.1. One of the reasons is that at 400 nm, the mean effective area is $\sim$ 10 cm^2 higher than at 470 nm. Secondly, as a result of the update on the dimensions of the PMT (systematic errors)[22]. In fact, using the conical opening angles from table 6.1.1, a small overlap arises between the gel pads of the old LOM configuration implemented within the new framework.

It is observed that the new geometry features a mean effective area that is $\sim$ 1.5 % larger than the former one. Nonetheless, it is more inhomogeneous according to Figure 6.3.3a and 6.3.3c. In particular, the standard deviations of the simulated effective areas with respect to their mean is of $\sim$ 4.3 % for the new geometry whereas it was only $\sim$ 3.1 % for the old one.[23] This presents the old geometry as a better one, however impossible to do due to the spatial limitations discussed previously. In addition to that, some extra components were placed in the new geometry to study the impact on the

[21] The resulting equatorial gel pad coincides with the photocathode at four points forming the vertices of a square, while the rest of the pad exceeds the photocathode slightly.

[22] With the implementation of the old PMTs into the new framework, values differ only by $\sim$ 0.2 %

[23] The same value for the new geometry with the "extra" components is raised to $\sim$ 4.6%.

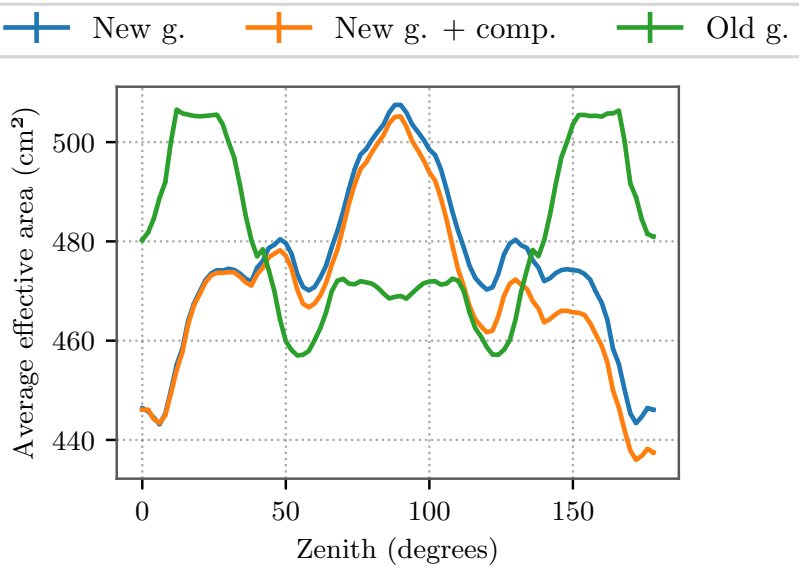

Figure 6.3.2: Effective area as a function of the zenith incidence angle averaged over all azimuth for the old geometry with conical gel pads (Old g.), the new one (New g.) and the new one with CAD components (New g. + comp.) .

performance, such as the PMT holding structure, the penetrator cable and the main-boards (Figure 6.3.1c), all of which were imported from the CAD version of the module created by the IceCube collaboration. The optical properties of the penetrator cable were taken from the one of the mDOM, while the rest was considered as a perfect absorber. As a result, the losses in the mean effective area are $\sim$ 1 %. To better understand where they come from, Figure 6.3.3d shows the effective areas of the new geometry without extra components subtracted by the one that has them. Hence, the bright spots indicate shadows caused by the different components, the main one of which corresponds to the penetrator in the southern region.

The average of the effective areas over all azimuth directions as a function of the zenith incidence direction is given in Figure 6.3.2. The former geometry performs better at the polar regions, as a result of the larger semi-opening angles of the polar gel pads, while the new one does at zenith incidence angles closer to 90°. It should be noted that the sites with maximum effective areas in the equatorial regions in Figure 6.3.3a and 6.3.3b do not correspond to situations where a PMT is directly targeted, but is an intermediate site between all of them. Finally, the values in Figure 6.3.2 are very similar for the new geometry with and without components, and the major differences arise at incidence angles close to 130 degrees due to the influence of the penetrator, which agrees with Figure 6.3.3d.

Table 6.3.1: Mean effective areas for the different configurations presented in Figure 6.3.1. The wavelength studied was 400 nm.

	Old geometry	New geometry	New geometry with additional components
$\overline{A_{eff}}$ (cm^2) $\pm$ 0.08	474.682	482.104	477.494

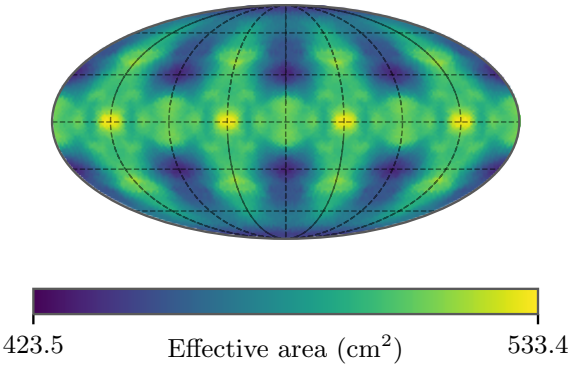

(a) New geometry of LOM-16.

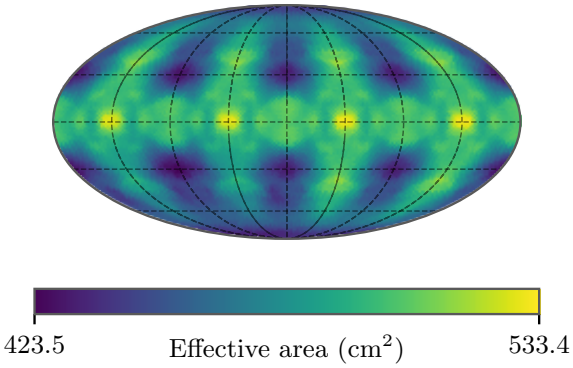

(b) New geometry of LOM-16 with penetrator, mini boards and PMT supporting structure.

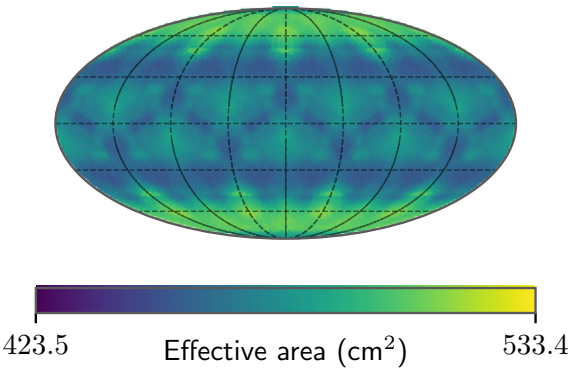

(c) Old geometry of LOM-16 with conical gel-pads.

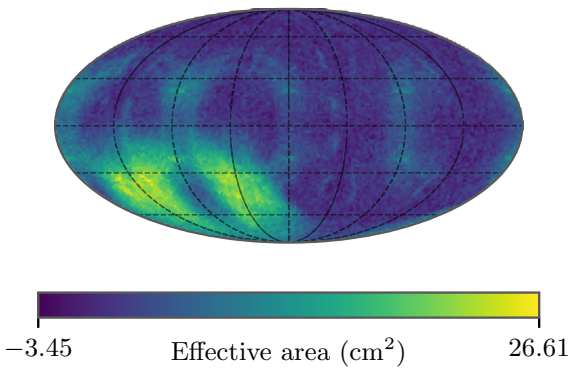

(d) Difference between (a) and (b).

Figure 6.3.3: Effective areas as a function of the incidence angles for the indicated cases.

7 Muon reconstruction on a water basin

The LOM and the mDOM are two new optical modules that will be implemented in future IceCube extensions and were already presented in chapter 2. Unlike the current deployed DOMs, they feature several PMTs housed in a glass vessel. Among the advantages compared to a single PMT is the segmentation of the sensitive area which provides intrinsic directional sensitivity. In the scope of this chapter, the zenith angular resolution of both types of modules for individual atmospheric muons in water was studied with Geant4 simulations, using machine learning for reconstruction.

7.1 Simulation setup

The setup used is depicted in Figure 7.1.1a. Both modules: mDOM and LOM, are simulated on Geant4 individually in the middle of a water basin. This corresponds to an actual one that is present in the basement of the Institute of Nuclear Physics of the University of Münster. For a good reconstruction, reflections of photons must be avoided to preserve their original directional information. In this context, its five walls are made out of opaque black material, while the top is fully covered by black balls. The reflectivities of these materials are calculated in the next section. In addition to that, the modules are held in place by a suction cup[24] which has been simulated as perfectly absorbent to take into account its shadow.

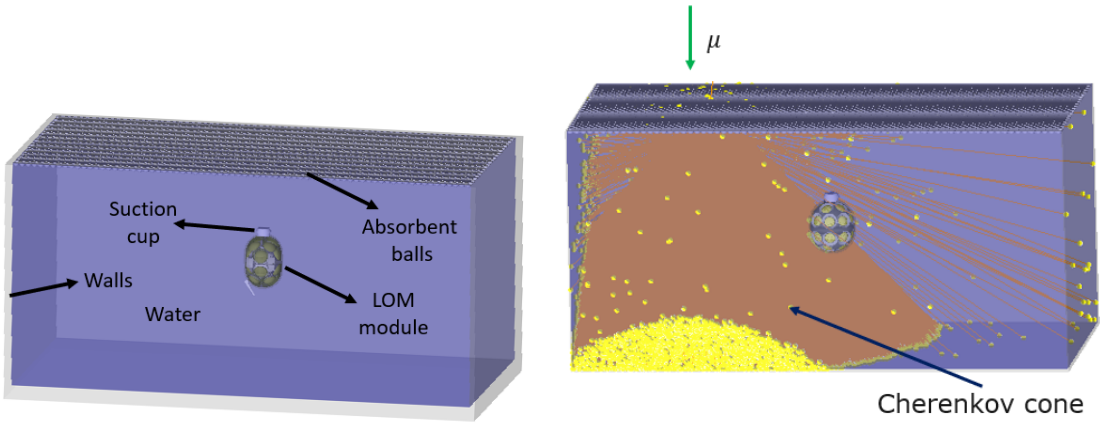

(a) **(b)**

Figure 7.1.1: **(a)**: Geometry visualisation in Geant4 of the setup with the LOM module. **(b)**: Simulated muon (with the direction of the green arrow) going through the water basin with the mDOM. In yellow the Cherenkov photons.

The LOM module corresponds to the latest configuration presented in section 6.3, with the penetrator cable, the PMT holding structure and the mini main boards. The code for the mDOM module was created in the framework of two PhD thesis ([35, 43]) and adapted into a new Geant4 framework by our working group. In addition, the penetrator cable of the mDOM was positioned to take into account its shadowing for a fair comparison with the LOM module. Some aspects of the actual response

[24] PBG-110. There is a string that connect it to the top surface but can it was neglected on the simulation.

of PMTs are considered, such as the QE when detecting a photon[25] and the limit of the dynamic range of PMTs, which is approximately of 180 photons.

The physical processes that are taken into account and the particles that will be considered appear in table 7.1.1. The most relevant process for muons is the Cherenkov emission. It is implemented by the class G4Cerenkov, and requires the definition of the refractive index of the medium. In the case of photons, as in the previous chapters, the main processes are reflections and refractions at the interfaces and absorptions on the materials. An example of a simulated muon going through the water basin is shown in Figure 7.1.1b, where the resulting photons appear in yellow.

As already explained in chapter 2, for Cherenkov emission to occur, the charged particle velocity must be greater than the phase velocity of light in the medium. This is equal to $\beta > 1/n$, where $\beta = v/c$ and $n = c/c'$, being c the velocity of light in vacuum, c' the velocity of light in the dielectric medium and v the velocity of the charged particle. Hence, the kinetic energy of the particle, E_{kin}, must be at least the threshold energy, E_{th}:

$$E_{kin} = m_0 \cdot c^2 \left(\frac{1}{\sqrt{1-\beta^2}} - 1 \right) > E_{th} = m_0 \cdot c^2 \left(\frac{1}{\sqrt{1-n^{-2}}} - 1 \right) = m_0 c^2 \left(\sqrt{\frac{n^2}{n^2-1}} - 1 \right), \tag{7.1.1}$$

where m_0c^2 is the rest energy of the particle. If m_0c^2 is substituted by the value of the muon ($\sim 0.106\,\text{GeV/c}^2$) and n by the refractive index of water (n = 1.333). Then, $E_{th} \sim 0.054$ GeV, which is two orders of magnitude lower than the mean energy of atmospheric muons at the ground (~ 4 GeV) [20]. For this reason, muons were simulated at an energy of 4 GeV. Nevertheless, according to eq. 2.3.2, the energy dependence of the Cherenkov yield is with β^2. Therefore, for energies that are sufficiently high with respect to the rest mass of the muon (e.g. over 1 GeV, where $\beta \sim 0.994$) the yield is approximately constant. This was confirmed by simulations for a given muon trajectory.[26]

For the zenith angle reconstruction, muons are simulated individually with random starting positions in planes that cover the entire setup, as it is shown in Figure 7.1.2. In turn, the directions of the normal vectors of such planes, which in spherical coordinates are defined by the azimuth (ϕ) and zenith (θ) angles, are randomly sampled. In the range [0^o, 90^o] for the zenith and [0^o, 360^o] for the azimuth angles. Consequently, the directions of the muons cover half of the entire solid angle and are homogeneously distributed in the zenith direction, which is the one to be reconstructed.

Table 7.1.1: Particles and physical processes used for the simulation to obtain the data for muon reconstruction.

Particle	**Geant4 physics class**	**Description**
Muon	G4Cerenkov	Generation of Cherenkov Photons
	G4MuIonisation	Ionisation process for muons
	G4MuBremsstrahlung	Bremsstrahlung for muons
	G4MuMultipleScattering	Scattering of muons
	G4MuPairProduction	Pair production process for muons
Optical photon	G4OpAbsorption	Absorption of optical photons
	G4OpBoundaryProcess	Reflection/refraction at optical interfaces
	G4OpRayleigh	Rayleigh scattering of photons
	G4OpMieHG	Mie scattering of photons

[25] In the way it was explained in chapter 4.

[26] These results are given in the Appendix in Figure A.0.1.

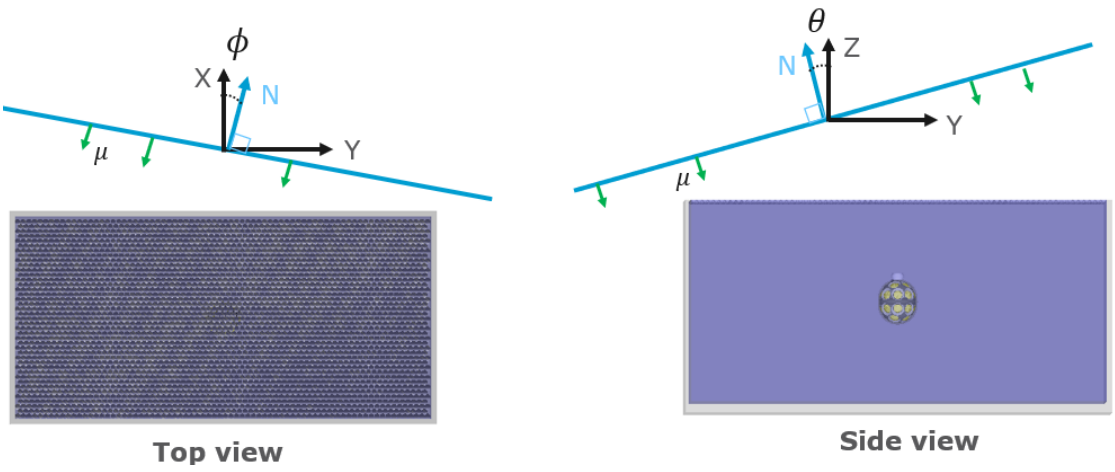

Figure 7.1.2: Schematic setup for the simulation of muons for the reconstruction. Muons (green arrows) are individually simulated with random origin in planes that cover the entire setup (blue lines) and that point to its centre.

7.2 Reflectivity measurement of basin boundary materials

The reflectivity is defined as the probability of reflection of photons at an interface between two materials as a function of their wavelength. This property can be assigned to a surface in Geant4[27], which were defined as *skin surfaces* in the case of the balls and as a *border surface* at the water-wall interface. In this regard, the experimental setup that appears in Figure 7.2.1 was used to measure it for the materials of the basin walls, and two candidates for absorbent balls.

First, a xenon lamp is used to supply light to an integrating sphere. The latter consists of a hollow sphere, the inner walls of which exhibit diffusive reflection in such a way that a ray of light incident at one point will be homogeneously distributed to all the other points. It is therefore only necessary to measure the light at an arbitrary point on the sphere, and it is sent to a spectrometer. This features various grating blaze positions optimised for measuring at different wavelengths and allows to obtain the intensity of the light as a function of the wavelength. Finally, the signal, which was digitised on the spectrometer, is directed to the computer where it is displayed.

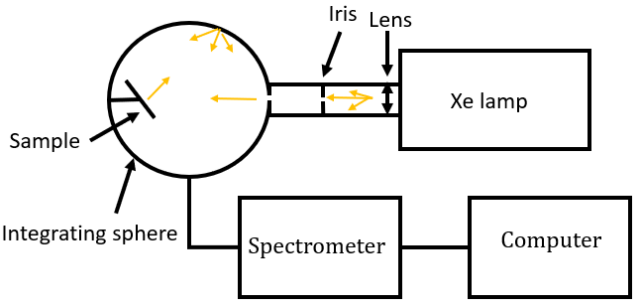

Figure 7.2.1: Experimental set-up for the measurement of the reflectivity. The yellow arrows represent photons. Explanation on the text.

With this setup, the reflectivity of a material can be calculated by comparing the light that is reflected on a sample placed within the integrating sphere, with the light that is measured without a sample (reference measurement) and with the one that is measured by placing a light trap (background measurement). In the end:

$$\text{Reflectivity} = \frac{M_{\text{Sample}} - M_{\text{Background}}}{M_{\text{Reference}} - M_{\text{Background}}}, \tag{7.2.1}$$

where M_{sample}, $M_{\text{Background}}$ and $M_{\text{Reference}}$ are the measurements with the sample, the background and the reference, respectively. For it to work properly, the light must be collimated and directed

[27] The definition of optical surfaces and its properties in Geant4 was already discussed in section 6.2.

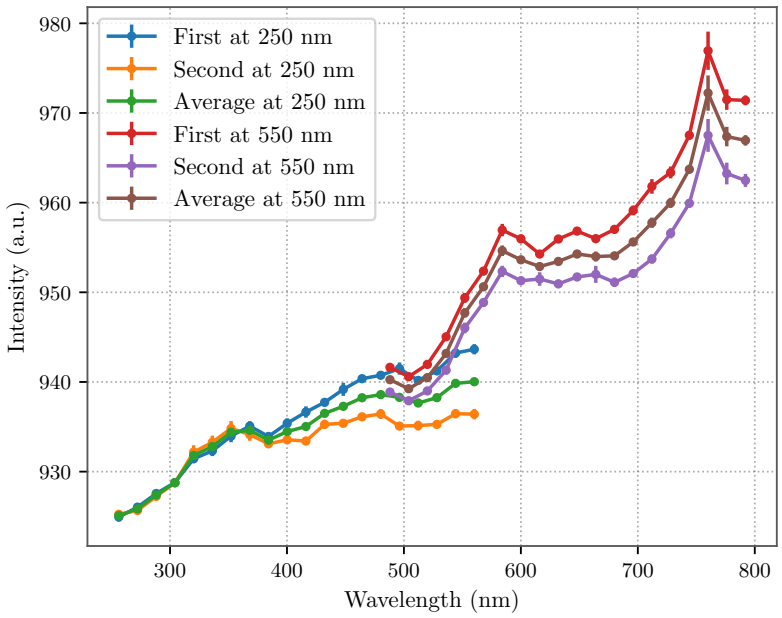

(a)

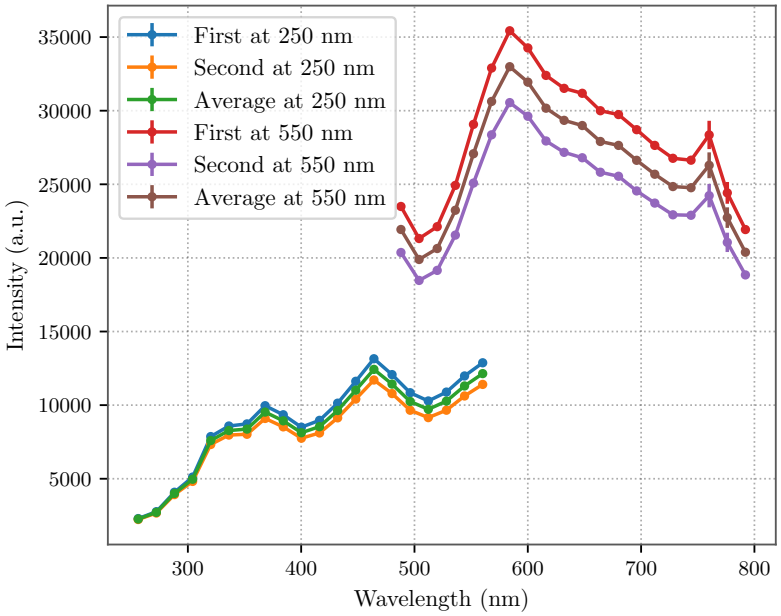

(b)

Figure 7.2.2: **(a)**: Measurement of the background. **(b)**: Measurement of the reference. "First" and "Second" stand for the measurements at the beginning and at the end, respectively. The measured points were joined for clarity. 250 nm and 550 nm stand for the two different grating blaze positions the measurements were taken.

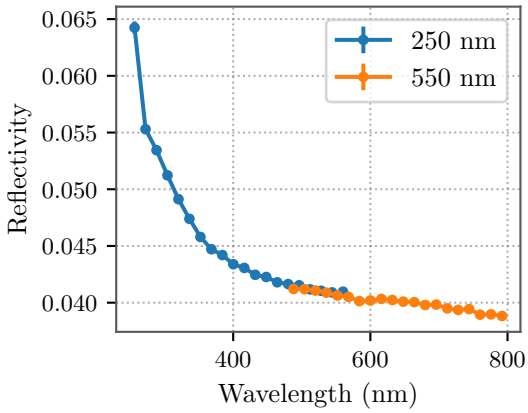

(a) First ball candidate

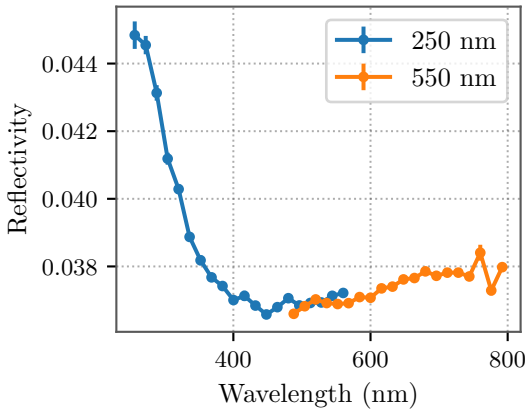

(b) Second ball candidate

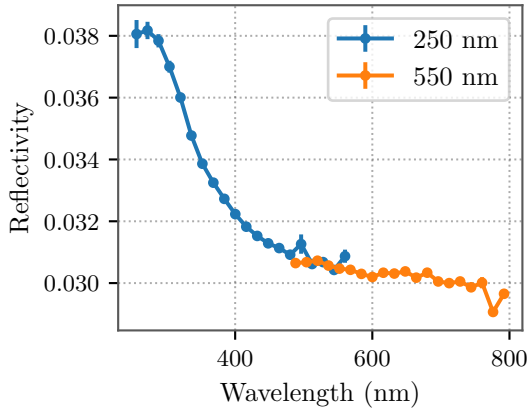

(c) Wall

Figure 7.2.3: Reflectivity as a function of the wavelength measured for different materials used for the boundary of the basin. The two colors represent the measurements at different blaze positions of the grating, which target the wavelengths shown on the legend. The measured points were joined for clarity.

only at the sample, otherwise the background is significantly increased. This is achieved by placing an iris before the entrance into the integrating sphere and a lens right after the lamp. In addition, the normal to the sample surface must be tilted with respect to the direction of the incident light so that the reflected light is not lost by backreflection towards the entrance aperture.

Since the lamp intensity varies over time, background and reference measurements are made at the beginning and at the end of the process (see Figure 7.2.2a and 7.2.2b), and the average is considered in the calculation of the reflectivity. In addition, all measurements are carried at two grating blaze positions, targeting 250 nm and 550 nm respectively, allowing measurements from below 300 nm (under which everything is absorbed in the glass pressure vessel of the modules) and over 700 nm, where the QE of the PMTs becomes zero. The final results for the reflectivities of the different materials can be seen in Figure 7.2.3. The wall material has the lowest reflectivity over the entire wavelength spectrum, followed by the second candidate of absorbent balls and finally, the first candidate. In particular, the first two cases feature an average reflectivity less than 4 %. In view of the results, the second absorbent ball candidate was chosen for the simulation.

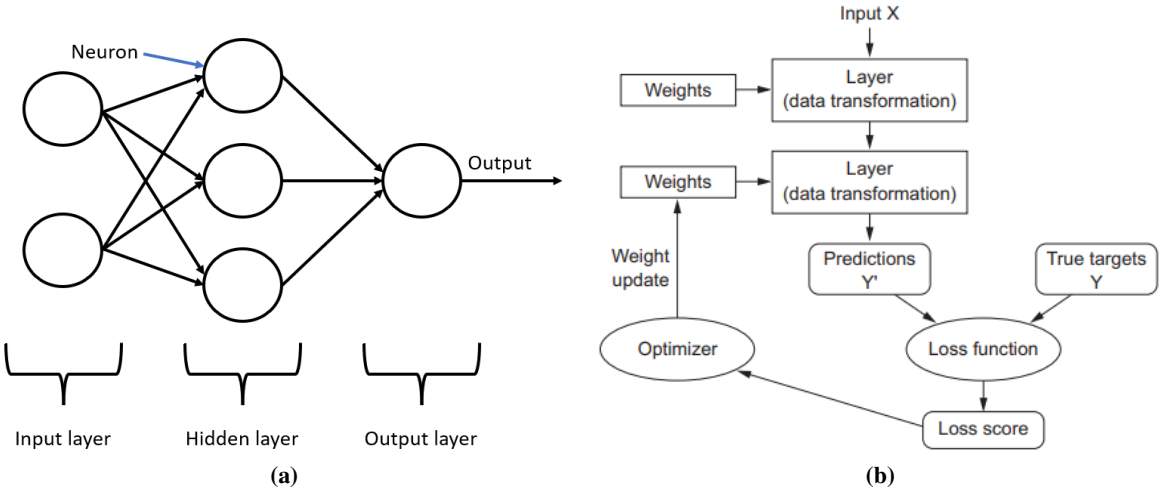

Figure 7.3.1: (a): Layer architecture of a fully connected neural network. **(b)**: Training process of a neural network. The weights and biases of the layers are updated to minimise the loss score. Image taken from [52].

7.3 Deep Learning principles

The reconstruction of the zenith incidence angle of muons will be done using machine learning algorithms[28]. Hence, the objective of this section is to provide the basics of these techniques to be implemented.

7.3.1 Fully connected neural networks

The goal of supervised learning is to obtain the rules that govern some input data (known as training data) whose "labels" are known and, therefore, it allows to predict those of new datasets. For this, a **neural network** (NN) is created, which consists of a series of layers each of which is made of **neurons**. The first and last layers are called the input and output layers, respectively, while any other in between is referred to as a hidden layer (see Figure 7.3.1a).

The data is transformed at each of the hidden layers and the output one by means of **activation functions**, $f(w \cdot x + b)$, where w is a **weight** matrix, b a **bias** and x is the input data of a layer. The size of the weight matrix of a layer is equal to the number of inputs times the number of neurons that form the layer, while the number of biases is equal only to the number of neurons. The output of one layer corresponds to the input of the next, so each step results in more complex and abstract representations of the data [52]. For this reason, this kind of NN are known as *fully connected*, since all the neurons of successive (dense) layers are connected.

In the end, a prediction of the label(s) of some input dataset is made based on the values of the weights and biases. The values of these parameters are generated randomly in the first instance and must be properly adjusted following the **training** process (see Figure 7.3.1b). With this in mind, a **loss function**, $L = L(w, b)$, is defined. This compares the true label of the input data with the predicted one by providing a **loss score** (usually simply called loss) that must be minimised. This is done by the **optimiser**, which updates the weights, w_k, and biases, b_k, to new values, $w_{k'}$ and $b_{k'}$, following the *stochastic gradient descendent* (SGD) method. For this, the gradient of the loss with respect to the weights and biases is calculated[29] for a certain number of training datasets (a **batch**), which are

[28] More precisely supervised learning algorithms.
[29] It is achieved using the *Backpropagation* algorithm [52].

randomly sampled. Then, the parameters are shifted to the opposite direction from the gradient as [53]:

$$w_k \to w_{k'} = w_k - \frac{\eta}{m}\sum_j \frac{\partial L_{X_j}}{\partial w_k}, \qquad b_k \to b_{k'} = b_k - \frac{\eta}{m}\sum_j \frac{\partial L_{X_j}}{\partial b_k}, \tag{7.3.1}$$

where m is the size of the batch, L_{X_j} is the loss for a training dataset X_j of the batch and η is the **learning rate**. At this point, a new batch is considered and the process continues until all the training data has taken into account, which is called an **epoch**. The training then consists of repeating this process to minimise the loss by continuously updating the weights and biases over several epochs, resulting in more accurate predictions. In addition, some optimisers apply the SGD with *momentum*, i.e. the parameter update carries inertia so that it depends not only on the current gradient but also on the previous ones, which is useful to avoid local minima of the loss, especially when the learning rate is small.

7.3.2 Convolutional neural networks (CNN)

While fully connected neural networks can only learn global patterns, convolutional neural networks (CNN) are able to recognise local, translationally invariant patterns on the input and their spatial hierarchies. Therefore, they are usually the best choice for computer vision applications [52]. The extraction of these features is done in CNN by using *filters* and the convolution operation works by sliding them over a 3D input tensor, which results in another 3D tensor called a *feature map*. The process for three 3×3 filters is depicted in Figure 7.3.2. Being $N \times N$ the size of the filters, a $N \times N$ 3D patch of the input feature map is extracted. Then, it is converted into a 1D tensor by means of a tensor product whose length corresponds to the number of filters that were used. The output feature map is then formed by the 1D tensors, that are arranged in such a way that their positions correspond to the original ones in the input feature map. As a result of the convolution process, the output width and height are reduced. If necessary, it can be avoided by the implementation of *padding*, which adds rows and columns to the input feature map to preserve the original dimensions.

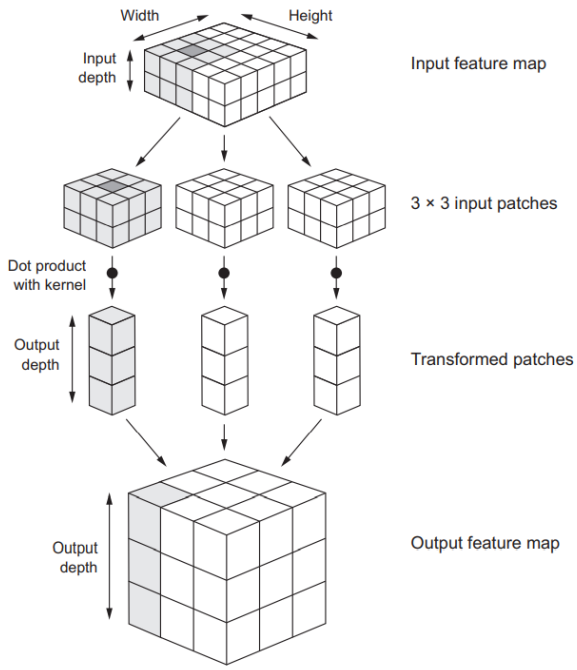

Figure 7.3.2: Convolution process over a 3D feature map. Explanation on text. Image taken from [52].

Convolution layers are usually followed by a *pooling* operation that reduces the size of the feature map. In particular, maxpooling substracts 2×2 windows from the input feature map and returns the maximum value for such a window. In the end, the height and width of the feature map are reduced by a factor of 2. The aim of this process it to reduce the number of information by retaining only the most relevant one, which provides a more efficient learning. At the end of a convolutional neural network the outputs are flattened so they can be the input of dense layers.

7.4 NN training with simulated data

As muons pass through the water basin, photons are emitted and detected by the different PMTs of each module. The array formed by the number of photons detected on each of the PMTs for each simulated muon event will constitute the datasets that are fed to the neural network(s), whose objective will be to predict the corresponding zenith directions. In order for the reconstruction to be carried out at all possible zenith angles without a prior favourable treatment, the data have been simulated with a homogeneous distribution of this parameter in the range that the atmospheric muons can take from zero to 90 degrees, as already explained in section 7.1.

In this thesis, the neural networks were created and trained in python making use of the *Keras* [52] deep-learning library. The first kind of NN that are going to be discussed are fully connected ones, whose architecture is characterised by the number of dense layers and the units (neurons) in each layer. In addition, ReLu (rectified linear unit) was the activation function implemented in the layers, which is one of the most universally used. It returns its input argument if it is positive and zero otherwise. As for the optimiser, it was opted for *Adam* [54], which implements momentum to the stochastic gradient descendent method. The mean squared error (mse) was selected as the loss function that compares the predicted labels with the real ones. It is defined as:

$$mse = \frac{1}{n}\sum_{i=1}^{n}\left(Y_i^{\text{predicted}} - Y_i^{\text{true}}\right)^2, \tag{7.4.1}$$

where $Y_i^{\text{predicted}}$ and Y_i^{true} are, respectively, the predicted and the true labels for the n data samples that are being compared on a batch. This function is widely used in cases where the predictions are to arbitrary continuous values.[30]

In most cases, it is not reliable to fed the NN data and labels that have very large values or that are very inhomogeneous. Hence, the most common approach is to normalise the input. In particular, for each feature, the mean was subtracted and then divided by the standard deviation. In that way, each input feature has a mean of zero and standard deviation of one, known as standardisation.

As explained in section 7.3.1a, NNs must follow a training process to properly adjust the coefficients of the weight matrix of its layers. In this way, they are changed by the optimiser to reduce the loss in a process that is repeated over several epochs. An example is found on Figure 7.4.1a, where the training loss (in orange) is reduced after each epoch as a consequence. The training line corresponds to the loss for the data used for the training, while the validation line is the loss after each epoch for data that were not fed to the training. Validation serves to monitor it, as after several epochs, the NN starts to "memorise" the training data, known as **overfitting**, and thus fails to generalise and to predict different datasets. Both training and validation sets (also called test set) are drawn from the same large set of simulated data that is randomly shuffled, with 80 % going to training and 20 % to validation. This must be done to ensure that there is no dataset that is in principle easier to predict than the other.

Apart from the loss, another metric that can be used to monitor the training is the mean absolute error (*mae*), and it is the one that will be used in this thesis to control the performance of the NN over epochs. In Figure 7.4.1b, it can be seen that this metric, like the loss, decreases over epochs. It must be noted that since the input is transformed to have a standard deviation of one and a mean of zero, the units of the mae are not degrees, but must be transformed accordingly.

The election of the best parameters for a given NN model and its training is not a precise science, but rather an empirical procedure. For this reason, several configurations were created and compared. The default learning rate for Adam ($1 \cdot 10^{-3}$) showed good performance. However, the performance improved slightly with a moderately reduced rate, which finally was set at $4 \cdot 10^{-4}$. The batch size for the training was always 32. The architecture for the training in Figure 7.4.1b consisted in 4 dense

[30] These kind of problems are known as regression, in contrast to other common ones such as classification, where discrete values are predicted.

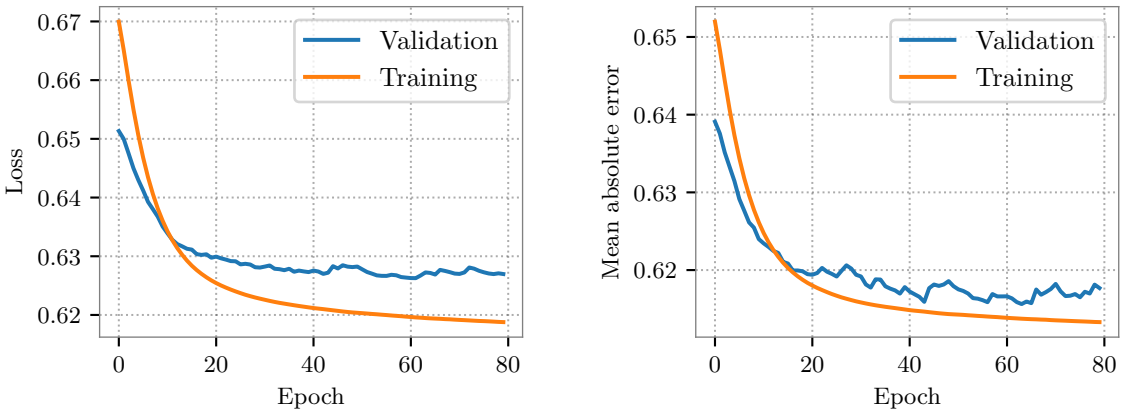

(a) **(b)**

Figure 7.4.1: Training of a fully connected model with $\sim 4 \cdot 10^5$ training parameters for the LOM data. **(a)**: Loss by epoch. **(b)**: Mae by epoch.

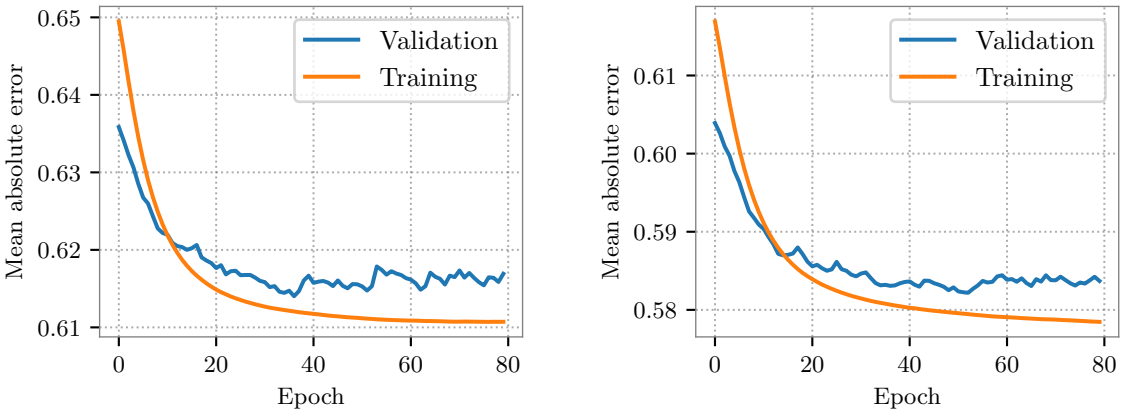

(a) **(b)**

Figure 7.4.2: Training and validation mae by epoch for the optimal fully connected models with $\sim 1.1 \cdot 10^6$ training parameters. **(a)**: LOM. **(b)**: mDOM.

layers[31] and a total of $\sim 4 \cdot 10^5$ parameters for the data of the LOM. Alternatively, in Figure 7.4.2a, a NN with the same number of layers and $\sim 1.1 \cdot 10^6$ parameters was trained. In the latter, the validation mae features lower values (0.614 vs. 0.616 for the respective minimum mae values). This indicates that the larger network performs slightly better. Even larger and intermediate networks resulted in worse performance. Therefore, the NN from Figure 7.4.2a proved to be the best among those tested. The same applies for the mDOM data, where the training for the equivalent optimal network[32] is shown in Figure 7.4.2b.

[31] In addition to one extraction layer that is used at the end in regression problems and that does not contain any activation function.

[32] The mDOM has more input values (24 vs. 16). Hence, the "same" network contains more parameters.

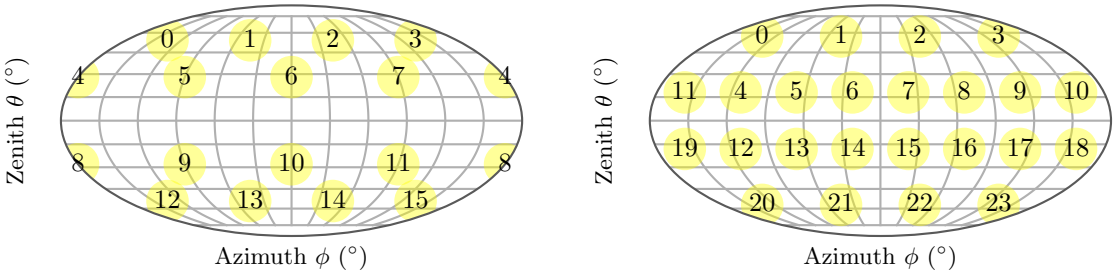

(a) LOM **(b)** mDOM

Figure 7.4.3: Angular distribution of the positions of the centres of the PMTs.

7.4.1 Training with convolution neural networks

In section 7.3.2, it was explained that for image applications, CNNs usually perform more efficiently than fully connected networks. In this context, if the angular distribution of the normal of the PMTs in both modules is considered (as it is shown for the centres of the PMTs in Figure 7.4.3), the number of detected photons on each PMT together with their spatial distribution for a given muon event will form a (spatial) detection pattern that is characterised by the direction of the incident muon. Two examples are given in Figure 7.4.4, where the detection of two different muons with the mDOM, which have the same zenith angle, provide similar detection patterns; but are shifted as a result of the different origins and azimuth directions of the muons. Therefore, the detection of a muon event can be considered as an image that can be fed to a CNN.

However, the images from Figure 7.4.4 cannot be given directly to the neural networks. In turn, the number of photons detected per muon event at each PMT of Figure 7.4.3 must be expressed in terms of a square matrix. In this regard, different arrays were considered[33] and the ones that provided the best results are found in Figure 7.4.5a and 7.4.5b for the LOM and the mDOM, respectively.

The trainings of the CNNs were done with the same same batch size, optimiser, learning rate and activation functions as in the previous section. Therefore, the main differences lie in the new representation of the data and in the architecture of the NN. The training of the optimal models that were found for the mDOM and the LOM data can be seen in Figure 7.4.6. In both cases, the networks consists of two convolution layers with filters 3×3, followed by a maxpooling operation and the output is flattened to fed a fully connected NN of three layers. Additionally, padding was used at the convolutional layers to preserve the size of the input matrices. Other networks with the same characteristics but with smaller filter size, different number of filters, different number and size of final dense layers and one additional maxpooling after the first convolutional layer were tried but resulted in (Sometimes only slightly) worse performance. In total, the optimal CNNs consist of $\sim 5\cdot10^5$ training parameters for the LOM and $\sim 8\cdot10^5$ for the mDOM, due to the larger number of pixels. The validation maes indicate that both perform better than the optimal fully connected models of $\sim 1.1\cdot10^6$ parameters, being the minimum maes of 0.6115 (vs. 0.614 with only fully connected) for the LOM and 0.58 (vs. 0.5822) for the mDOM. However, the performance is not greatly improved either. In this respect, it should be noted that this type of neural network is limited in this problem, for example, by the number of available pixels.

[33] A few examples are shown on the appendix, Figure A.0.2.

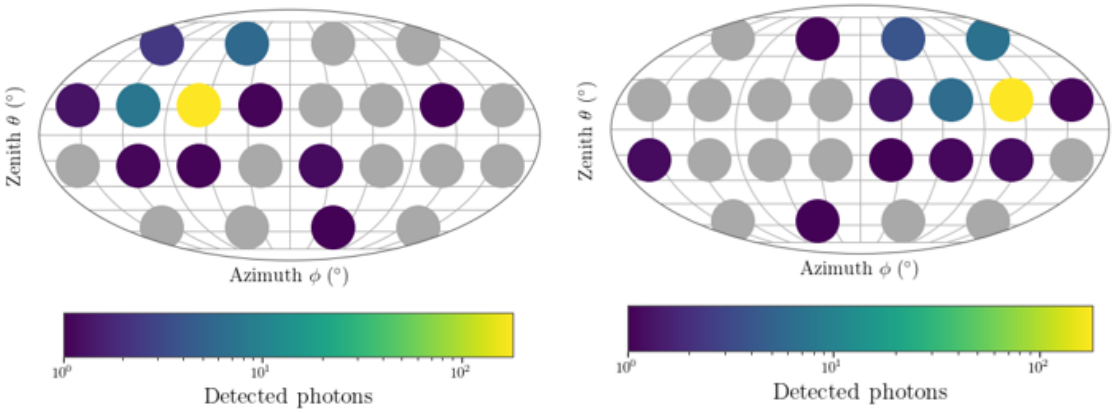

(a) **(b)**

Figure 7.4.4: Detection pattern for two different muon events for the mDOM. The muons have the same zenith angle but different azimuth angles and origins. Each circle represents the respective PMT on Figure 7.4.3. Grey color means no photon detected.

PMT0	PMT1	PMT2	PMT3
PMT4	PMT5	PMT6	PMT7
PMT8	PMT9	PMT10	PMT11
PMT12	PMT13	PMT14	PMT15

(a)

0	0	0	0	0	0	0	0
0	0	0	0	0	0	0	0
0	PMT0	0	PMT1	0	PMT2	0	PMT3
PMT11	PMT4	PMT5	PMT6	PMT7	PMT8	PMT9	PMT10
PMT19	PMT12	PMT13	PMT14	PMT15	PMT16	PMT17	PMT18
0	PMT20	0	PMT21	0	PMT22	0	PMT23
0	0	0	0	0	0	0	0
0	0	0	0	0	0	0	0

(b)

Figure 7.4.5: Matrix representations of the input data to use in CNNs. The labels "PMTi" stand for the number of photons detected per muon event at the PMTs characterised by the same labels in Figure 7.4.3. **(a)**: LOM data. **(b)**: mDOM data.

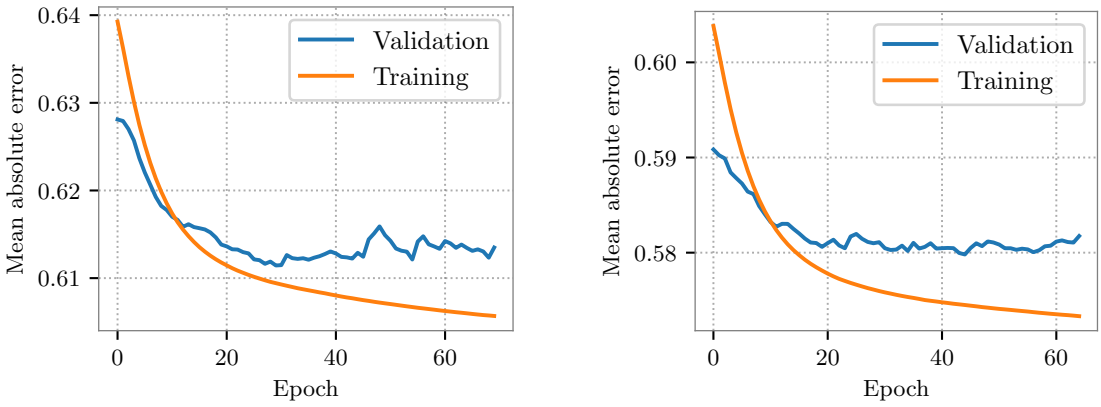

(a) **(b)**

Figure 7.4.6: Training and validation mae by epoch for the optimal CNNs: **(a)**: LOM data. **(b)**: mDOM data.

7.4.2 Regularisation

In each of the trainings, the mae continues to decrease as epochs increase for the training data set, but reaches a plateau or even increases approximately above certain epochs for the validation set. This is a sign of overfitting, which can be avoided by simply stopping training at the appropriate epoch, known as *early stopping*. This is one of the so-called *regularisation* methods to deal with overfitting. Other two common techniques that were considered are *l2 regularisation* and *dropout*. They have in common that they make the training set more difficult to memorise for the NN. Dropout achieves this by *dropping out* a certain percentage of output features of a layer, while l2 regularisation adds to the final loss an amount for every weight coefficient in a layer that is proportional to the squared value of the weight coefficient, hence, it prevents the weights from taking very high values.

In Figure 7.4.7a is depicted the mae by epoch after using a dropout rate of 0.3 placed after the flattened operation in the optimal CNN for the mDOM data. In keras, this dropout rate indicates that 30 % of the outputs of the layer before are set to zero. Besides, Figure 7.4.8a represents the same case but with the LOM data, with the difference that the dropout rate is 0.2. As expected, the overfitting is reduced. In addition, the values of the best validation maes are similar to the corresponding ones without regularisation.

On the other side, Figure 7.4.8b and 7.4.7b show the maes for the optimal CNN of the LOM and mDOM data, respectively, after using l2 regularisation with a proportionality factor of 0.0001 in the dense layers. In these cases, the overfitting is reduced as well. However, the maes take higher values, which are even worse if the proportionality factor is increased.

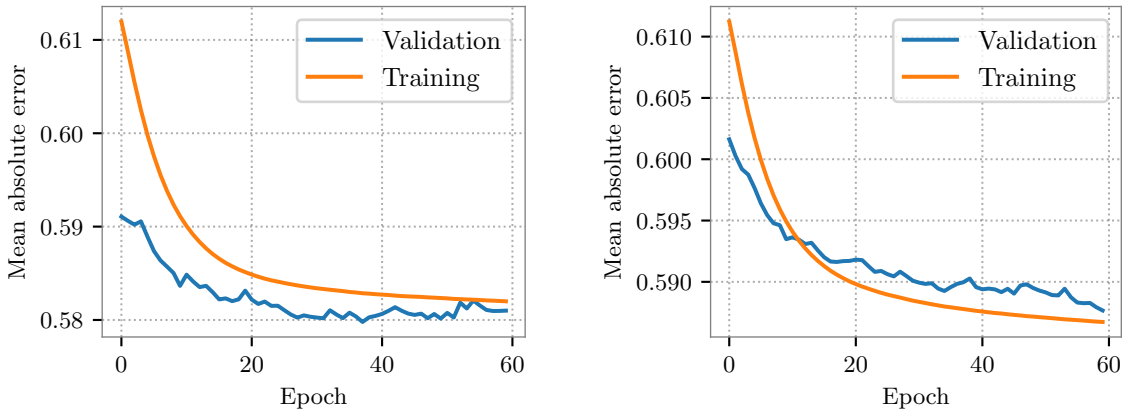

(a) Dropout

(b) L2 regularisation

Figure 7.4.7: Training and validation mae by epoch for the optimal mDOM CNN using regularisation techniques. Explanation on text.

7.5 Zenith angular resolution for simulated muons

In the end, it was decided to use CNNs with dropout for the reconstruction since they are less prone to overfitting and have a similar overall performance to those without dropout. The performance of these networks was tested on new data that had not been confronted in any way with them during the training process. The reason is that even former test data can leak some information to the models due to their constant tuning.

The reconstructions of the zenith angles of the simulated events are shown in Figure 7.5.1 (for the LOM) and Figure 7.5.2 (for the mDOM), based on certain selection criteria according to the number of photons detected per event. The plots correspond to two dimensional histograms where

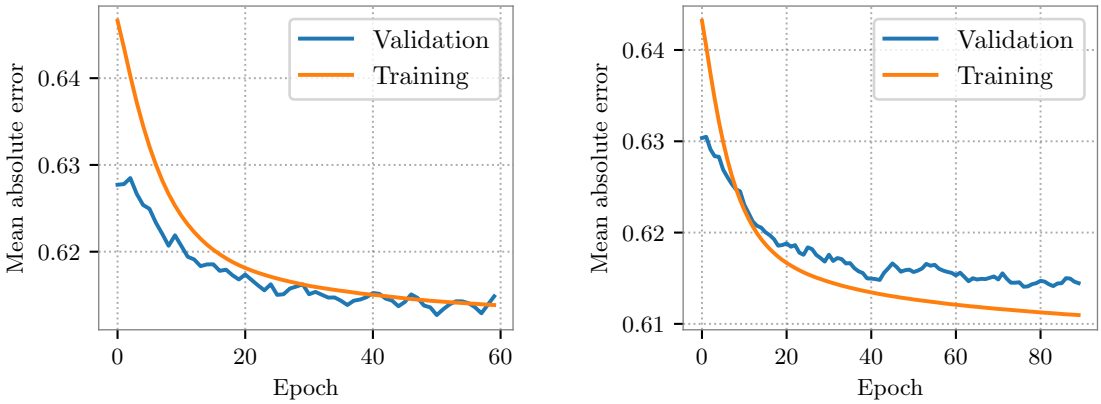

(a) Dropout

(b) L2 regularisation

Figure 7.4.8: Training and validation mae by epoch for the optimal LOM CNN using regularisation techniques. Explanation on text.

the predicted zenith angles are represented against the true values. Hence, a perfect reconstruction would follow the diagonal red lines that are given.

In cases where less than 10 photons are detected, the appearance of horizontal patterns is notable. This is characteristic of data whose training was unsuccessful for different reasons, so the model tends to predict the average between them to minimise the loss. On the other hand, in the range of 10-50 detected photons, the horizontal accumulation mostly disappears, and a better reconstruction pattern emerges, which improves as the threshold of detected photons is increased. The reason is that the more photons are detected, the more directional information is provided and the better the event can be reconstructed. Yet, some horizontal accumulations appear even for a high detection threshold. The difference between these and those found for 1-10 detected photons is that they do not cover the whole spectrum of true zeniths, but only certain ranges. Therefore, the predictions are not arbitrary, but the network is "indecisive" between a certain range of values. In fact, these accumulations disappear to some extent if the networks are trained for more epochs or if they are trained without dropout, indicating that there may be a problem of underfitting in relation to these ranges of values.[34] On the other hand, the networks used for the reconstructions in Figures 7.5.1 and 7.5.2 were trained until they started experimenting a general overfitting i.e. with early stopping, as discussed in the last section 7.4.2. Thus, an overall balance has to be sought, with the networks used in the reconstructions shown having the smallest errors overall.[35]

Due to the limited performance of both modules in the range of 10-50 detected photons, a detection threshold of 50 photons was eventually considered. This selection represents $\sim$ 42 % of the detected events in both modules, with $\sim$ 44 % of the total detected events belonging to the range 1-10 (the distribution of the number of photons detected per event is given in the Appendix, Figure A.0.4). The overall predictions are shown in Figure 7.5.3. In addition, the distributions of the differences between the simulated and reconstructed zenith angles ($\theta_{\text{true}} - \theta_{\text{predicted}}$) are given in Figure 7.5.4a. The black vertical lines are placed at the respective medians which are close to zero. The red vertical lines delimit the region in which 68 % of the values are found, i.e. one sigma, and it is the width of such interval that is considered as the resolution, in the following. In this line, the resolutions for this detection threshold as well as for the different selection criteria that were implemented in Figure

[34] This is probably because the detection patterns of these values are very similar and therefore particularly difficult to differentiate for the network.

[35] Reconstructions for the LOM that do not feature horizontal accumulations for the same optimal networks without dropout are provided on the appendix for illustration, Figure A.0.3. All of them present worse resolutions.

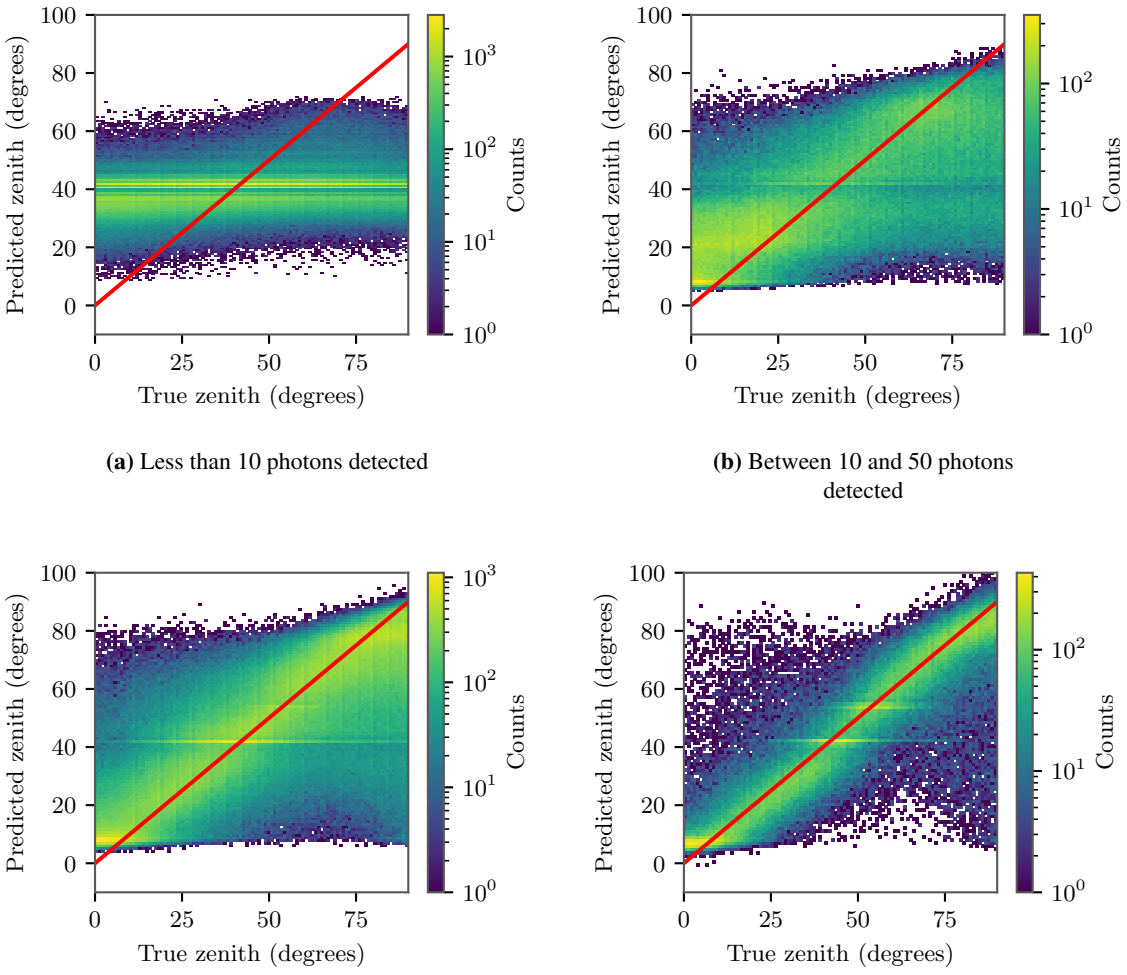

(a) Less than 10 photons detected

(b) Between 10 and 50 photons detected

(c) Between 50 and 250 photons detected

(d) At least 250 photons detected

Figure 7.5.1: Predicted zenith angles vs. true ones for different selection criteria on the number of photons detected per event for the LOM.

7.5.2 and 7.5.1 are shown on table 7.5.1. In all cases, the mDOM features a resolution that is a couple of degrees better than that of the LOM. Since the mDOM has a larger number of PMTs (24 vs. 16), on average, more of them are hit, which provides more directional information. More precisely, for a detection threshold of 50 photons, 12 PMTs are hit on average on the mDOM whereas only 10 on the LOM.[36]

It is important to note that the performance is not homogeneous across all zenith angles. In Figure 7.5.5a and 7.5.5b, the medians of the distributions of the differences between simulated and predicted zenith angles are represented as a function of the true zenith angle. Besides, the resolution as a function of the true zenith angle for both modules is given in Figure 7.5.3. In all the cases it was considered a detection threshold of 50 photons. The performance is better at moderate zenith angles than at extreme ones, where the absolute values of the medians are $\sim 10^\circ$. On the one side, this behaviour is, to some extent, common in the type of networks that were implemented. Since there is no data neither above 90° nor under 0°, the network fails in the regression of these values. On the other side, the basin is a rectangular prism, whose length is greater than its height. For this reason, not all zenith

[36]The distribution of the number of PMTs that are hit per event at this photon detection threshold are given in the Appendix, Figure A.0.5.

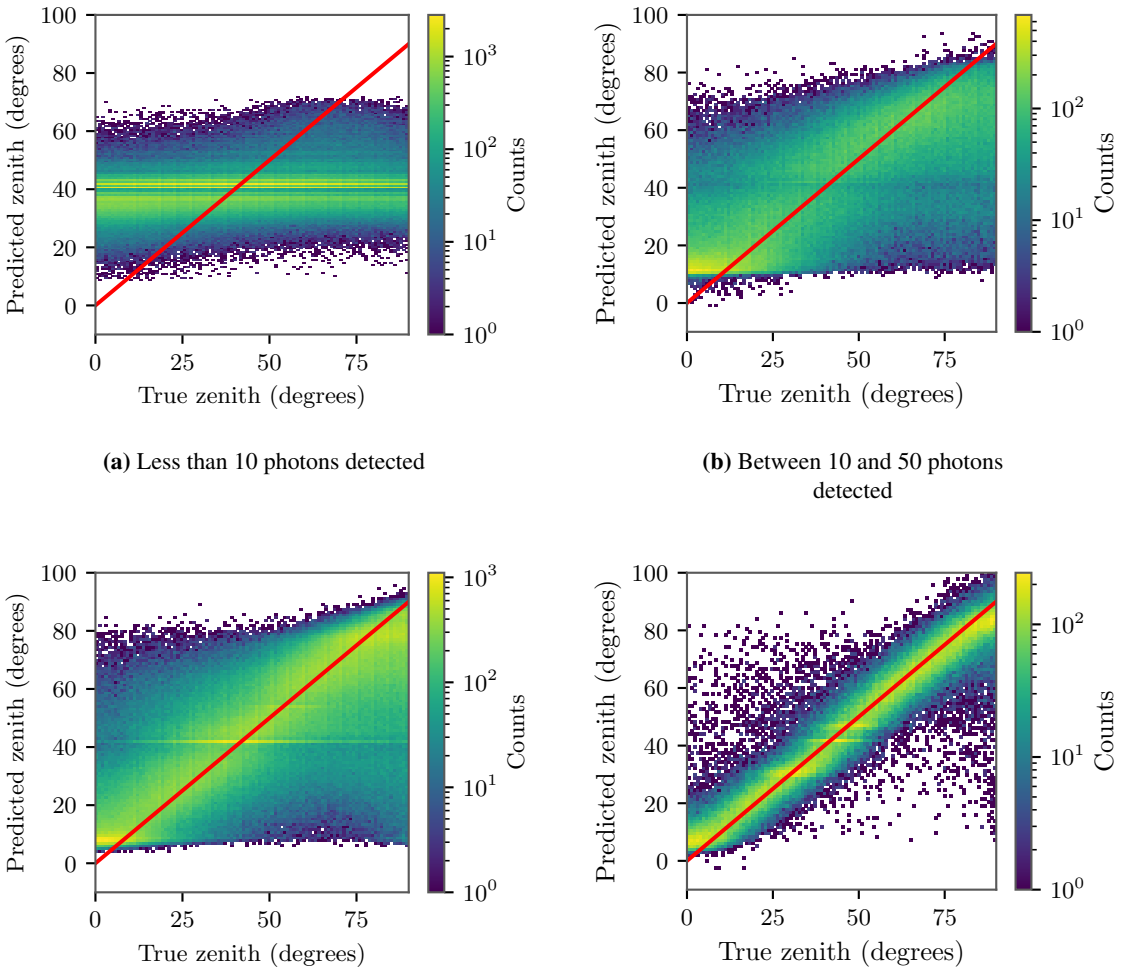

(a) Less than 10 photons detected

(b) Between 10 and 50 photons detected

(c) Between 50 and 250 photons detected

(d) At least 250 photons detected

Figure 7.5.2: Predicted zenith angles vs. true ones for different selection criteria on the number of photons detected per event for the mDOM.

directions are treated under the same conditions, and it is observed that on average, more photons are detected per event for higher zenith angles. This is illustrated by the angular distribution of the events in which at least 50 photons are detected, given in appendix, Figure A.0.6. The architecture of the CNNs and the election of some of the parameters for the training, such as the loss function and the number of epochs, may also have some influence.

As a result of the resolution's angular dependence, the overall resolution for a realistic muon angular distribution will vary. In particular, if the average angular distribution at sea level is considered, i.e. $\sim \cos^2(\theta)$, the distributions of the differences between the simulated and reconstructed zenith angles can be seen in Figure 7.5.6. In both cases, the medians are shifted to negative values, and the sigma interval is now considerable inhomogeneous with respect to zero difference. All the relevant values can be found on table 7.5.2.

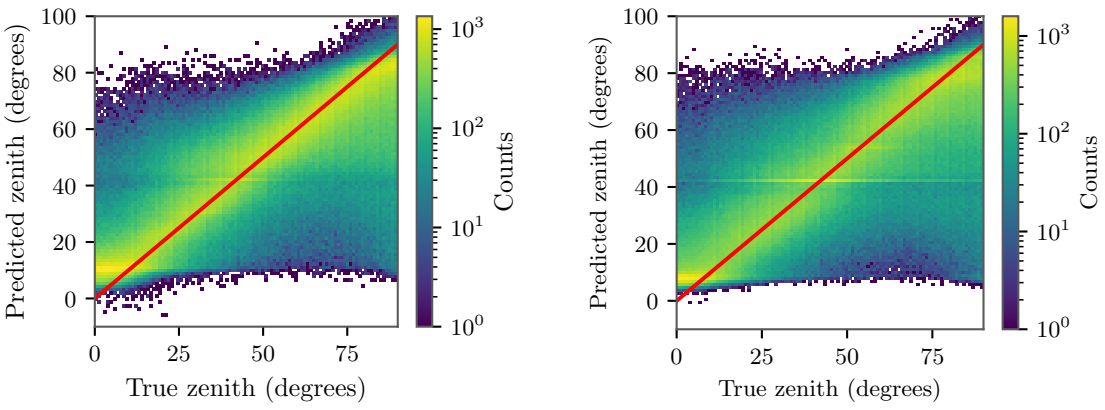

(a) mDOM reconstruction

(b) LOM reconstruction

Figure 7.5.3: Predictions of the optimal models in data where at least 50 photons are detected. The red line correspond to an ideal performance.

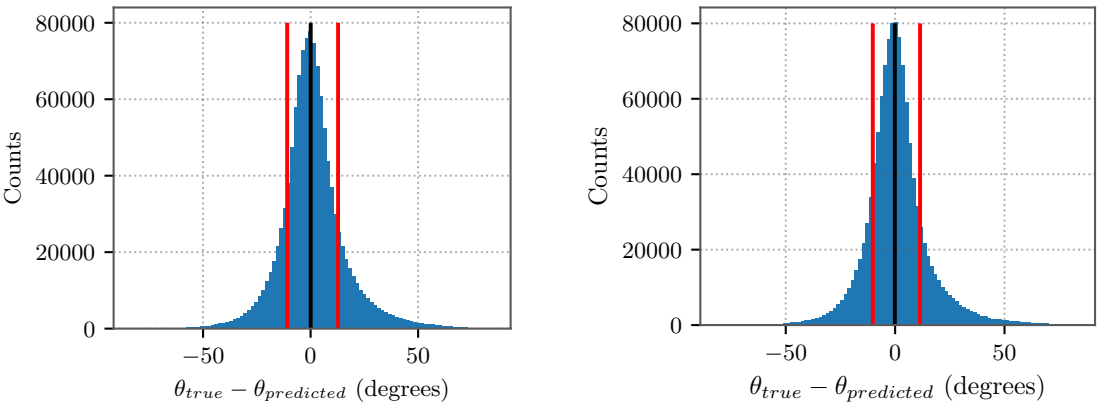

(a) Reconstruction with LOM

(b) Reconstruction with mDOM

Figure 7.5.4: Distribution of the differences between simulated and predicted zenith angles ($\theta_{true} - \theta_{predicted}$). The vertical black lines lie on the median whereas the red lines delimit the one sigma region, i.e. where 68 % of the values are found. Resolutions are sometimes one degree greater than the sum of the errors due to rounding.

Table 7.5.1: Median and resolution for the distributions formed by the differences between the true and predicted zenith angles. Different selection criteria has been implemented based on the number of detected photons per event. The sum of the errors of the median may deviate from the resolution value by one degree due to rounding on the units. The units are degrees.

Module	Photons detected	Median (1σ)	Resolution
LOM	$\geqq 50$	0^{+13}_{-11}	24
	<10	0^{+29}_{-26}	55
	10-50	-1^{+21}_{-16}	37
	50-250	0^{+14}_{-12}	26
	$\geqq 250$	1^{+7}_{-7}	14
mDOM	$\geqq 50$	0^{+11}_{-10}	22
	<10	-1^{+29}_{-25}	54
	10-50	-1^{+17}_{-14}	31
	50-250	0^{+13}_{-11}	24
	$\geqq 250$	0^{+5}_{-5}	11

Table 7.5.2: Median and resolution for the distributions formed by the differences between the true and predicted zenith angles considering a muon angular distribution $\sim \cos^2(\theta)$. The sum of the errors of the median may deviate from the resolution value by one degree due to rounding on the units. Units are degrees.

Module	Photons detected	Median (1σ)	Resolution
LOM	$\geqq 50$	-4^{+9}_{-12}	21
mDOM	$\geqq 50$	-4^{+8}_{-10}	19

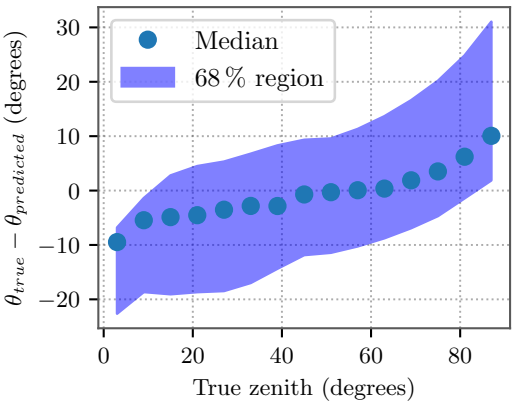

(a) LOM

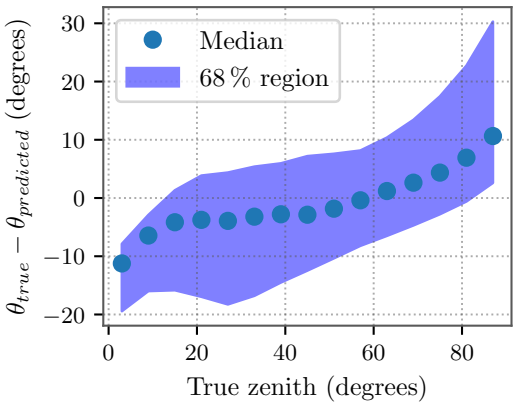

(b) mDOM

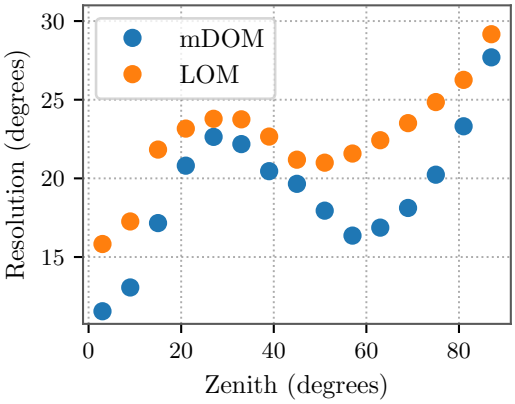

(c)

Figure 7.5.5: (a)-(b): Median and one sigma region for the distributions of the differences between simulated and predicted zenith angles as a function of the true zenith angle. **(c)**: Resolution as a function of the true zenith angle.

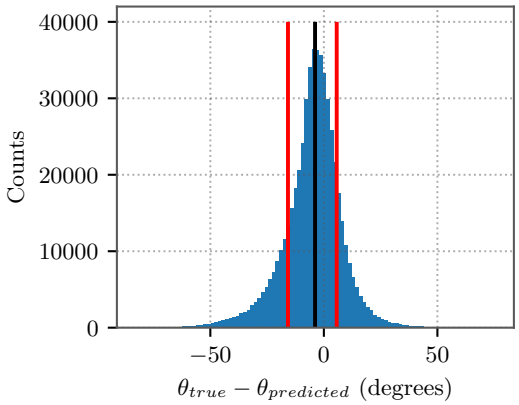

(a) Reconstruction with LOM

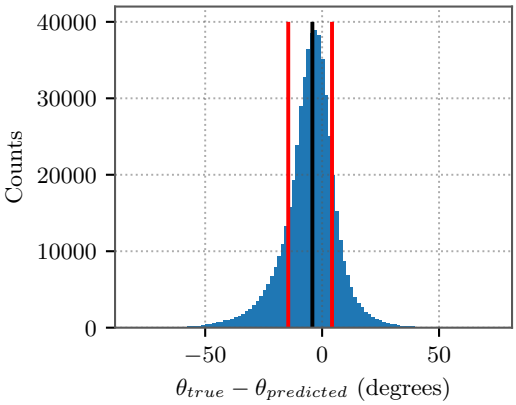

(b) Reconstruction with mDOM

Figure 7.5.6: Distribution of the differences between simulated and predicted zenith angles ($\theta_{true} - \theta_{predicted}$) for the average muon angular distribution at sea level, i.e. $\sim \cos^2(\theta)$.

8 Summary and outlook

The first aim of this thesis was to perform sensitivity studies for the gel pads of the LOM-16 - a new multi-PMT optical module for IceCube Gen2 - by means of Geant4 simulations. Gel pads are a new design feature of the LOM which serve as optical coupling between the glass vessel and the PMTs and increase the effective area of the module, resulting in better performance than conventional metallic reflectors due to the 100 % efficient total internal reflection and their higher angular acceptance.

The sensitivities of pad configurations resulting from different manufacturing approaches were compared: "regular" gel pads made entirely out of gel, gel pads surrounded by an acrylic/plastic shell that would provide a better bond between the glass vessel and the gel pads and acrylic pads that would be easier to produce. From a simulation point of view, their differences came from their different optical properties, i.e. acrylics feature a larger refreactive index (close to 1.5 vs. $\sim$ 1.4 of the gel) whereas the gel has (in general) longer absorption lengths, especially at shorter wavelengths. The results showed that both alternative approaches can provide performances similar to that of regular gel pads for realistic values, with $\sim$ 0.3 % losses for a 2 mm thick acrylic shell with refractive index of 1.5 and losses of $\sim$ 2-2.5 % for an acrylic pad with acrylic refractive index of 1.5 and gel as coupling. Furthermore, for acrylic pads with coupling refractive indices of 1.5, enhancements of up to $\sim$ 7 % are observed since this refractive index coincides with that of the glass materials and provides a more efficient total internal reflection. Nonetheless, the acrylic pad and in-situ plastic shell methods were finally discarded for the fabrication of gel pads due to delaminations at low temperatures as a result of the different coefficients of thermal expansion than the one of the gel.

Another aspect of the gel pads that was treated was its geometry. For this, three shapes were considered: conical, ellipsoidal and Winston cones (also known as CPC [49]). The first two were already studied in the scope of a Master thesis [40]. In this thesis, a further constrained was imposed, i.e. that gel pads cannot overlap. All shapes had in common that they provided maximum performance for their largest possible apertures. In addition, it has been observed that, although Winston cones are cut and asymmetrical, they outperform all other shapes for the incidence angles they have been designed for. However, they result in more inhomogeneous acceptance. Overall, ellipsoidal shapes provided the best performance, both in homogeneity and absolute values of the sensitivity. Yet, the differences are only slightly more than 1 % with respect to the "worst" shape, the cones. Hence, the latter have been ultimately selected as they are the easiest to produce.

Besides, roughness on the side of the gel pads was implemented in Geant4. The sensitivity was simulated for four different kind of reflections as a function of a roughness coefficient. The latter corresponds to the sigma value of the normal distributions that characterise the differences between the average surface normal and the normal of the micro-facets that form the rough surface. Both the kind of reflection and the roughness coefficient must be properly set by comparison with experiments. Nonetheless, a very likely scenario is a roughness coefficient lower than 0.75 radians ($\sim 40^{\circ}$) with losses in performance less than 4 %.

The most recent LOM-16 configuration created by the IceCube collaboration was implemented in Geant4. It features regular gel pads with conical shape and the distribution of the PMTs is symmetric in both hemispheres of the module. Its sensitivity was $\sim$1.5 % higher than the former configuration, with a mean effective area of (482.104 ± 0.08 (cm^2)) at 400 nm. However, its angular acceptance was more inhomogeneous, being the standard deviation of the simulated effective areas with respect to the mean effective area more than 1 % larger than the old geometry. In addition, the penetrator cable, the PMT supporting structure and the mini-main boards were simulated (imported from CAD) and losses

in performance of $\sim 1\,\%$ were observed due to their shadow. As for the future, the shape of the new equatorial gel pads needs to be improved. Their axis of symmetry do not follow those of the PMTs, so they are no longer analytical volumes (like normal cones) and have been simulated approximately as cones with ellipsoidal section.

The second aim of this thesis was to test the intrinsic directional resolution of the mDOM and the LOM for the case of the zenith angle of individually simulated muons in water. To this end, both modules were simulated in the middle of a water basin that corresponds to a real one that is at the basement of the Institute for Nuclear Physics at Münster.

For the reconstruction, neural networks were used, and the ones that provided the best results were convolutional neural networks. To do so, the detection of simulated muons were considered as images formed by the number of photons detected in each PMT together with their angular distribution within the modules. For the optimisation of the neural networks, several of them with different architecture, matrix representation of the input data, regularisation techniques and training parameters were compared.

In the end, the resolutions, defined as the width of the one sigma interval of the distributions formed by the differences between the true and reconstructed zenith angles, were some degrees better on the mDOM than in the LOM. In particular, for events where at least 50 photons are detected and with muons zenith directions homogeneously distributed (prior selection) in the range of 0° to 90° , it is of 24° on the LOM and 22° on the mDOM. The reason is that mDOM has a larger number of PMTs (24 vs. 16) and therefore it provides (on average) more directional information for the same number of detected photons than the LOM.

Yet, the performance is not homogeneous across all zenith angles. It improves for moderate values (40° to 60°) whereas it is worse close to 0° and 90°. One of the reason is that there is no data neither above 90° nor under 0° and thus the network fails in the regression of those values. In addition, the shape of the basin (a rectangular prism whose length is greater than its height) results in asymmetric acceptance for the different zenith directions, and, on average, more photons per event are detected for larger zeniths. Besides, the election of the parameters of the network and its training could have some influence.

In the future, the module response and reconstruction performances can be tested with measurements at NEVOD, which features additional detectors that provide the true directions. Therefore the simulations and the reconstructions must be done again with this larger basin. In addition, the large volume will reduce the differences due to asymmetries of the basin for different zenith directions. Moreover, several modules can be considered at the same time, so the detection time could be an important input.

A Additional figures for chapter 7

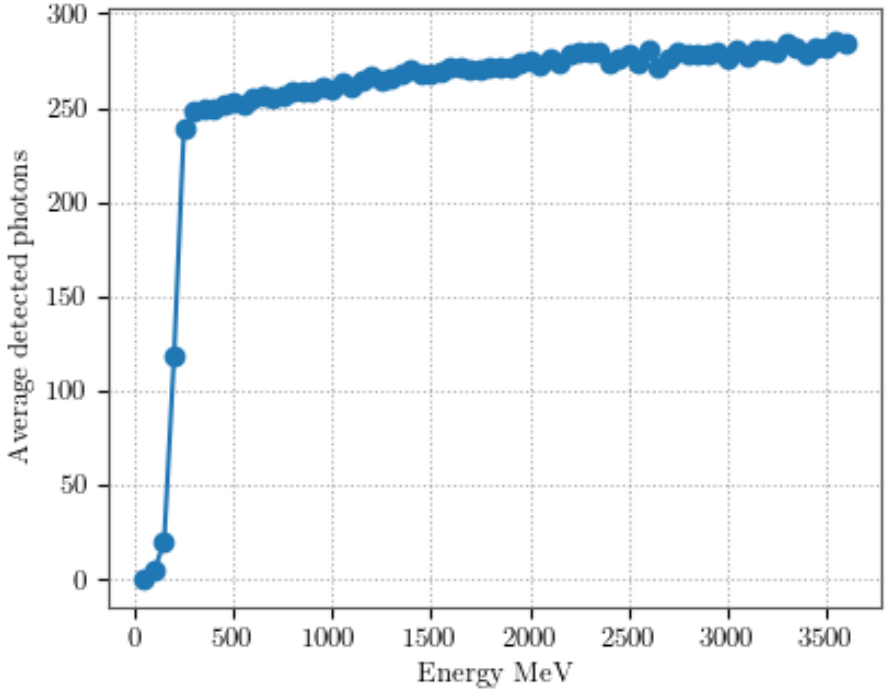

Figure A.0.1: Average number of detected photons for a given muon trajectory as a function of the muon energy with the mDOM. Simulated values were joined.

0	0	0	0	0	0	0	0	0	0	0	0	0	0	0
0	0	0	0	0	0	0	0	0	0	0	0	0	0	0
0	0	0	0	0	0	0	0	0	0	0	0	0	0	0
0	0	0	0	0	0	0	0	0	0	0	0	0	0	0
0	PMT0	0	0	0	PMT1	0	0	0	PMT2	0	0	0	PMT3	0
0	0	0	0	0	0	0	0	0	0	0	0	0	0	0
PMT11	0	PMT4	0	PMT5	0	PMT6	0	PMT7	0	PMT8	0	PMT9	0	PMT10
0	0	0	0	0	0	0	0	0	0	0	0	0	0	0
PMT19	0	PMT12	0	PMT13	0	PMT14	0	PMT15	0	PMT16	0	PMT17	0	PMT18
0	0	0	0	0	0	0	0	0	0	0	0	0	0	0
0	PMT20	0	0	0	PMT21	0	0	0	PMT22	0	0	0	PMT23	0
0	0	0	0	0	0	0	0	0	0	0	0	0	0	0
0	0	0	0	0	0	0	0	0	0	0	0	0	0	0
0	0	0	0	0	0	0	0	0	0	0	0	0	0	0
0	0	0	0	0	0	0	0	0	0	0	0	0	0	0

(a)

0	0	0	0	0	0	0	0	0	0	0	0	0	0	0
0	0	0	0	0	0	0	0	0	0	0	0	0	0	0
0	0	0	0	0	0	0	0	0	0	0	0	0	0	0
0	0	0	0	0	0	0	0	0	0	0	0	0	0	0
0	0	0	0	0	0	0	0	0	0	0	0	0	0	0
0	0	0	0	0	0	0	0	0	0	0	0	0	0	0
0	PMT0	0	0	0	PMT1	0	0	0	PMT2	0	0	0	PMT3	0
PMT11	0	PMT4	0	PMT5	0	PMT6	0	PMT7	0	PMT8	0	PMT9	0	PMT10
PMT19	0	PMT12	0	PMT13	0	PMT14	0	PMT15	0	PMT16	0	PMT17	0	PMT18
0	PMT20	0	0	0	PMT21	0	0	0	PMT22	0	0	0	PMT23	0
0	0	0	0	0	0	0	0	0	0	0	0	0	0	0
0	0	0	0	0	0	0	0	0	0	0	0	0	0	0
0	0	0	0	0	0	0	0	0	0	0	0	0	0	0
0	0	0	0	0	0	0	0	0	0	0	0	0	0	0

(b)

0	0	0	0	0	0	0	0
0	0	0	0	0	0	0	0
0	PMT0	0	PMT1	0	PMT2	0	PMT3
PMT4	0	PMT5	0	PMT6	0	PMT7	0
PMT8	0	PMT9	0	PMT10	0	PMT11	0
0	PMT12	0	PMT13	0	PMT14	0	PMT15
0	0	0	0	0	0	0	0
0	0	0	0	0	0	0	0

(c)

Figure A.0.2: Different matrix representations for the mDOM ((**a)** and **(b)**) and LOM **(c)** data that were tried in order to use CNN.

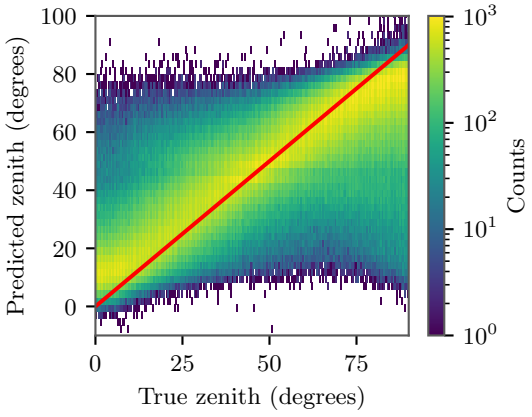

(a) At least 50 photons detected.

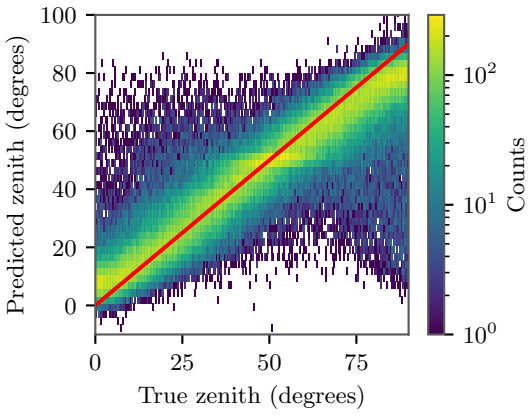

(b) At least 250 photons detected.

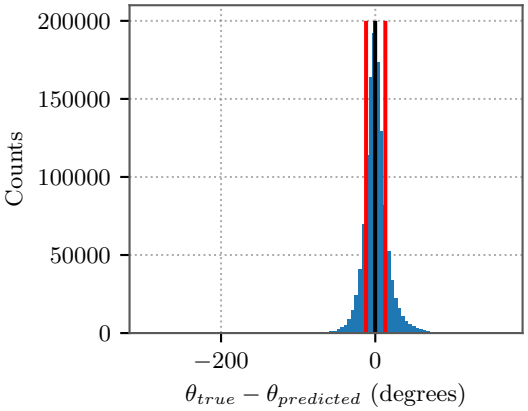

(c) Resolution for at least 50 photons detected.

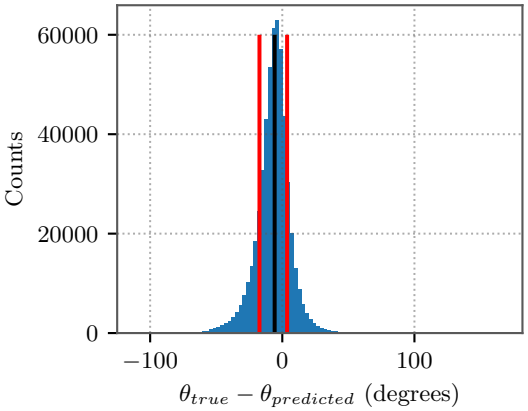

(d) Resolution for at least 50 photons detected and considering $\cos^2(\theta)$ as angular distribution.

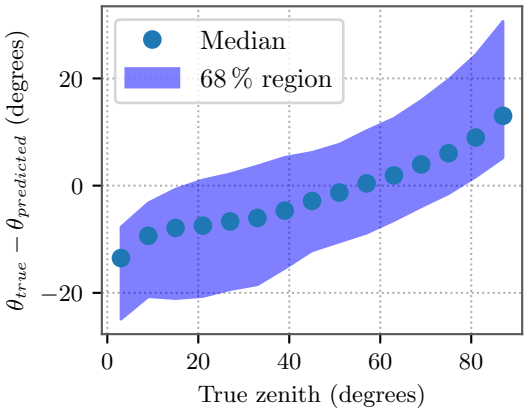

(e) Median and resolution as a function of true zenith.

Figure A.0.3: Reconstruction of the data of the LOM using the optimal convolutional network without dropout and with early stopping. **(a) and (c)**: The resolution is 25° while the median is at 0 25°. **(b)**: The resolution is 15° and the median is at 1°. **(d)** : The median is at -6° and the resolution is 21°. **e**: Median and one sigma region for the distributions of the differences between simulated and predicted zenith angles as a function of the true zenith angle.

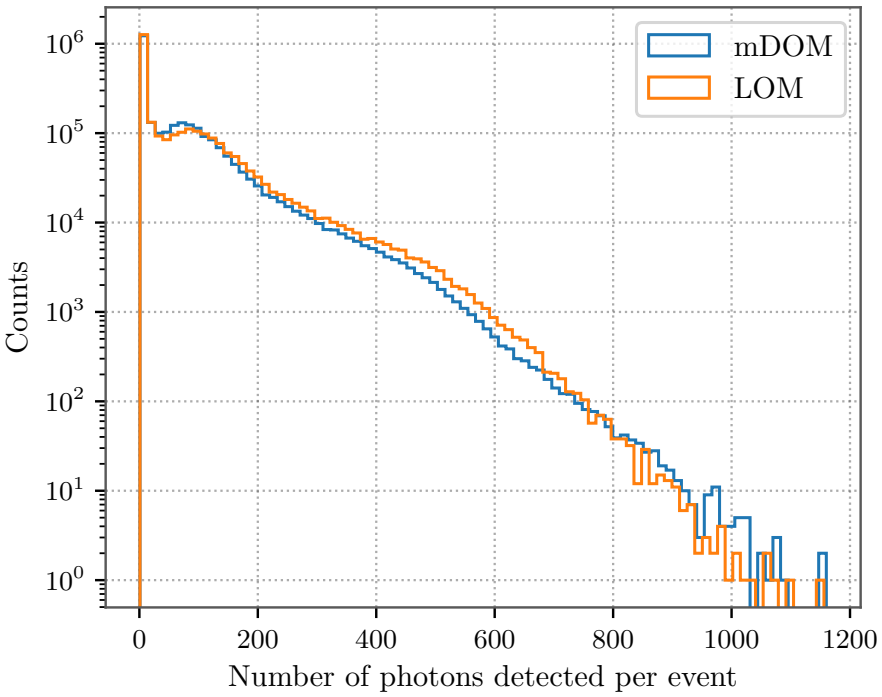

Figure A.0.4: Number of photons detected per muon event.

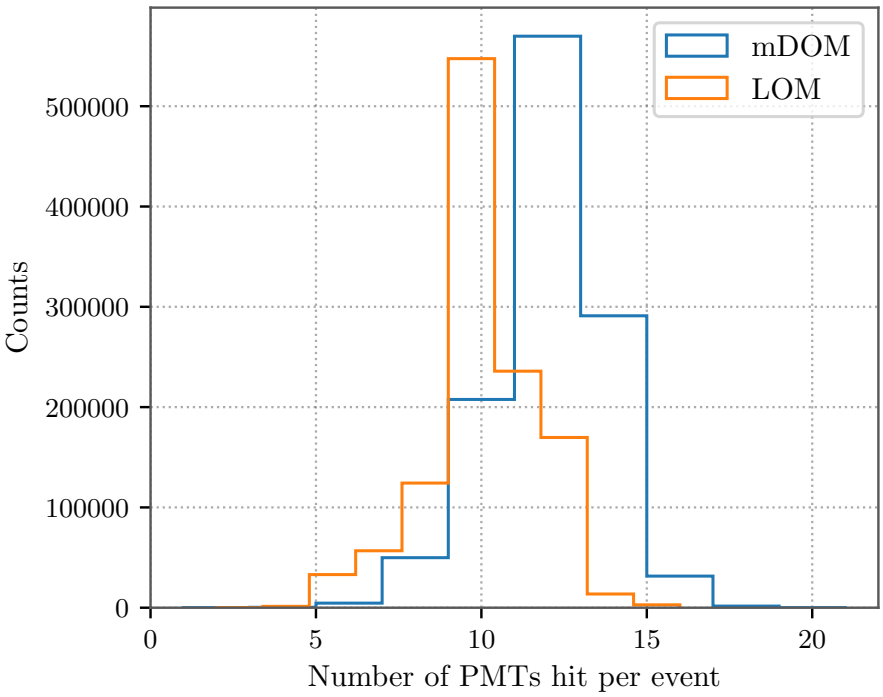

Figure A.0.5: Distribution of the number of PMTs hit per muon event where at least 50 photons are detected.

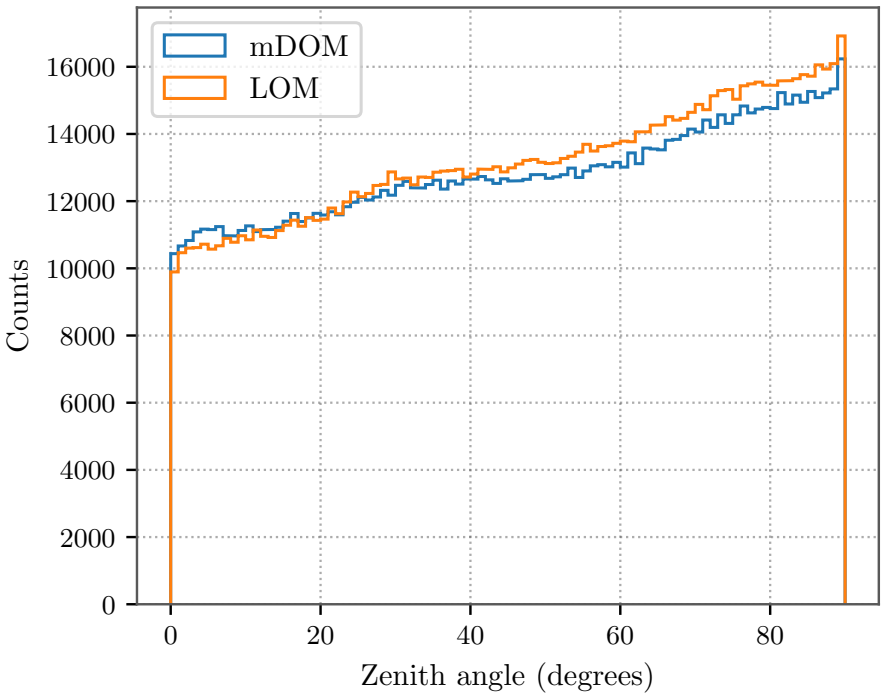

Figure A.0.6: Zenith angular distribution of the detected muon events in which at least 50 photons are detected. The original distribution of simulated muons was homogeneous across all zenith angles.

Bibliography

[1] Carlo Giunti and Chung W. Kim. *Fundamentals of Neutrino Physics and Astrophysics*. 2007. ISBN: 978-0-19-850871-7.

[2] J. Chadwick. "Possible Existence of a Neutron". In: *Nature* 129.3252 (Feb. 1932), pp. 312–312. DOI: 10.1038/129312a0. URL: https://doi.org/10.1038/129312a0.

[3] Enrico Fermi. "Tentativo di una Teoria Dei Raggi ". In: *Il Nuovo Cimento* 11.1 (Jan. 1934), pp. 1–19. DOI: 10.1007/bf02959820. URL: https://doi.org/10.1007/bf02959820.

[4] Clyde L Cowan Jr et al. "Detection of the free neutrino: a confirmation". In: *Science* 124.3212 (1956), pp. 103–104.

[5] Francis Halzen and Spencer R. Klein. "Invited Review Article: IceCube: An instrument for neutrino astronomy". In: *Review of Scientific Instruments* 81.8 (Aug. 2010), p. 081101. DOI: 10.1063/1.3480478. URL: https://doi.org/10.1063/1.3480478.

[6] "Evidence for High-Energy Extraterrestrial Neutrinos at the IceCube Detector". In: *Science* 342.6161 (Nov. 2013). ISSN: 1095-9203. DOI: 10.1126/science.1242856. URL: http://dx.doi.org/10.1126/science.1242856.

[7] Y. Fukuda et al. "Evidence for Oscillation of Atmospheric Neutrinos". In: *Physical Review Letters* 81.8 (Aug. 1998), pp. 1562–1567. ISSN: 1079-7114. DOI: 10.1103/physrevlett.81.1562. URL: http://dx.doi.org/10.1103/PhysRevLett.81.1562.

[8] Q. R. Ahmad et al. "Direct Evidence for Neutrino Flavor Transformation from Neutral-Current Interactions in the Sudbury Neutrino Observatory". In: *Physical Review Letters* 89.1 (June 2002). ISSN: 1079-7114. DOI: 10.1103/physrevlett.89.011301. URL: http://dx.doi.org/10.1103/PhysRevLett.89.011301.

[9] *The Nobel Prize in physics 2015*. URL: https://www.nobelprize.org/prizes/physics/2015/press-release/. (accessed: 8-1-2022).

[10] K.A. Olive. "Review of Particle Physics". In: *Chinese Physics C* 38.9 (Aug. 2014), p. 090001. DOI: 10.1088/1674-1137/38/9/090001. URL: https://doi.org/10.1088/1674-1137/38/9/090001.

[11] and M. Aker et al. "Direct neutrino-mass measurement with sub-electronvolt sensitivity". In: *Nature Physics* 18.2 (Feb. 2022), pp. 160–166. DOI: 10.1038/s41567-021-01463-1. URL: https://doi.org/10.1038/s41567-021-01463-1.

[12] Claus Grupen et al. *Astroparticle physics*. Vol. 50. Springer, 2005.

[13] Manuel Vogel. "Cosmic rays and particle physics, 2nd edition, by Thomas K. Gaisser, Ralph Engel, and Elisa Resconi". In: *Contemporary physics* 58.3 (2017), pp. 288–288. ISSN: 1366-5812. DOI: 10.1080/00107514.2017.1311376. URL: https://repository.gsi.de/record/209659.

[14] Christian Spiering. "Towards high-energy neutrino astronomy". In: *The European Physical Journal H* 37.3 (July 2012), pp. 515–565. ISSN: 2102-6467. DOI: 10.1140/epjh/e2012-30014-2. URL: http://dx.doi.org/10.1140/epjh/e2012-30014-2.

[15] P. Padovani et al. “Active galactic nuclei: what’s in a name?” In: *The Astronomy and Astrophysics Review* 25.1 (Aug. 2017). ISSN: 1432-0754. DOI: 10.1007/s00159-017-0102-9. URL: http://dx.doi.org/10.1007/s00159-017-0102-9.

[16] Mark Aartsen et al. “Multimessenger observations of a flaring blazar coincident with high-energy neutrino IceCube-170922A”. In: *Science* 361.6398 (July 2018). ISSN: 1095-9203. DOI: 10.1126/science.aat1378. URL: http://dx.doi.org/10.1126/science.aat1378.

[17] Kenneth Greisen. “End to the Cosmic-Ray Spectrum?” In: *Phys. Rev. Lett.* 16 (17 Apr. 1966), pp. 748–750. DOI: 10.1103/PhysRevLett.16.748. URL: https://link.aps.org/doi/10.1103/PhysRevLett.16.748.

[18] G. T. Zatsepin and V. A. Kuzmin. “Upper limit of the spectrum of cosmic rays”. In: *JETP Lett.* 4 (1966), pp. 78–80.

[19] Antonio Ereditato, ed. *The state of the art of neutrino physics: a tutorial for graduate students and young researchers*. Vol. 28. Advanced series on directions in high energy physics. New Jersey: World Scientific, 2018, 571 p. ISBN: 9789813226081. URL: https://bib-pubdb1.desy.de/record/411479.

[20] S. Cecchini and M. Spurio. “Atmospheric muons: experimental aspects”. In: *Geoscientific Instrumentation, Methods and Data Systems* 1.2 (Nov. 2012), pp. 185–196. DOI: 10.5194/gi-1-185-2012. URL: https://doi.org/10.5194/gi-1-185-2012.

[21] *Cosmic ray shower*. URL: https://en.wikipedia.org/wiki/File:AirShower.svg. (accessed: 10-1-2022).

[22] S. Fukuda et al. “The Super-Kamiokande detector”. In: *Nuclear Instruments and Methods in Physics Research Section A: Accelerators, Spectrometers, Detectors and Associated Equipment* 501.2-3 (Apr. 2003), pp. 418–462. DOI: 10.1016/s0168-9002(03)00425-x. URL: https://doi.org/10.1016/s0168-9002(03)00425-x.

[23] John David Jackson. *Classical electrodynamics; 2nd ed.* New York, NY: Wiley, 1975.

[24] I. M. Frank and I. E. Tamm. “Coherent visible radiation of fast electrons passing through matter”. In: *Compt. Rend. Acad. Sci. URSS* 14.3 (1937), pp. 109–114. DOI: 10.3367/UFNr.0093.196710o.0388.

[25] M.G. Aartsen et al. “The IceCube Neutrino Observatory: instrumentation and online systems”. In: *Journal of Instrumentation* 12.03 (Mar. 2017), P03012–P03012. ISSN: 1748-0221. DOI: 10.1088/1748-0221/12/03/p03012. URL: http://dx.doi.org/10.1088/1748-0221/12/03/P03012.

[26] R. Abbasi et al. “The design and performance of IceCube DeepCore”. In: *Astroparticle Physics* 35.10 (May 2012), pp. 615–624. ISSN: 0927-6505. DOI: 10.1016/j.astropartphys.2012.01.004. URL: http://dx.doi.org/10.1016/j.astropartphys.2012.01.004.

[27] R. Abbasi et al. “IceTop: The surface component of IceCube”. In: *Nucl. Instrum. Meth. A* 700 (2013), pp. 188–220. DOI: 10.1016/j.nima.2012.10.067. arXiv: 1207.6326 [astro-ph.IM].

[28] Aya Ishihara. *The IceCube Upgrade – Design and Science Goals*. 2019. arXiv: 1908.09441 [astro-ph.HE].

[29] T. Anderson et al. *Design and performance of the multi-PMT optical module for IceCube Upgrade*. 2021. arXiv: 2107.11383 [astro-ph.IM].

[30] Yuya Makino. “D-Egg: A next-generation optical module for IceCube”. In: *EPJ Web of Conferences* 207 (2019). Ed. by C. Spiering, p. 06005. DOI: 10.1051/epjconf/201920706005. URL: https://doi.org/10.1051/epjconf/201920706005.

[31] Ryo Nagai and Aya Ishihara. "Electronics Development for the New Photo-Detectors (PDOM and D-Egg) for IceCube-Upgrade". In: *arXiv preprint arXiv:1908.11564* (2019).

[32] S. Adrián-Martínez et al. "The prototype detection unit of the KM3NeT detector". In: *The European Physical Journal C* 76.2 (Jan. 2016). ISSN: 1434-6052. DOI: 10.1140/epjc/s10052-015-3868-9. URL: http://dx.doi.org/10.1140/epjc/s10052-015-3868-9.

[33] Lew Classen, Alexander Kappes, and Timo Karg. *A multi-PMT Optical Module for the IceCube Upgrade*. 2019. arXiv: 1908.10802 [astro-ph.HE].

[34] M.A. Unland Elorrieta et al. "Characterisation of the Hamamatsu R12199-01 HA MOD photomultiplier tube for low temperature applications". In: *Journal of Instrumentation* 14.03 (Mar. 2019), P03015–P03015. ISSN: 1748-0221. DOI: 10.1088/1748-0221/14/03/p03015. URL: http://dx.doi.org/10.1088/1748-0221/14/03/P03015.

[35] L. Classen. "The mDOM - a multi-PMT digital optical module for the IceCube-Gen2 neutrino telescope". PhD thesis. Feb. 2017. URL: https://www.uni-muenster.de/imperia/md/content/physik_kp/agkappes/abschlussarbeiten/doktorarbeiten/1702-phd_lclassen.pdf.

[36] M G Aartsen et al. "IceCube-Gen2: the window to the extreme Universe". In: *Journal of Physics G: Nuclear and Particle Physics* 48.6 (Apr. 2021), p. 060501. ISSN: 1361-6471. DOI: 10.1088/1361-6471/abbd48. URL: http://dx.doi.org/10.1088/1361-6471/abbd48.

[37] M. G. Aartsen et al. *Neutrino astronomy with the next generation IceCube Neutrino Observatory*. 2019. arXiv: 1911.02561 [astro-ph.HE].

[38] Nobuhiro Shimizu, Aya Ishihara, and Alexander Kappes. *Performance studies for a next-generation optical sensor for IceCube-Gen2*. 2021. arXiv: 2108.05548 [astro-ph.IM].

[39] Vedant Basu et al. "A next-generation optical sensor for IceCube-Gen2". In: *Proceedings of 37th International Cosmic Ray Conference — PoS(ICRC2021)* (July 2021). DOI: 10.22323/1.395.1062. URL: http://dx.doi.org/10.22323/1.395.1062.

[40] D. Suárez García. "Modeling of a multi-PMT optical sensor for IceCube-Gen2 in GEANT4 and Monte Carlo studies to optimize its sensitivity". MA thesis. 2021. URL: https://www.uni-muenster.de/imperia/md/content/physik_kp/agkappes/abschlussarbeiten/masterarbeiten/masterthesis_danielsuarez.pdf.

[41] Geant Collaboration. "Book For Application Developers". In: (2021). URL: https://geant4-userdoc.web.cern.ch/UsersGuides/ForApplicationDeveloper/fo/BookForApplicationDevelopers.pdf.

[42] *Geant4 web site*. URL: https://geant4.web.cern.ch/. (accessed: 27-2-2022).

[43] B. Herold. "Simulation and measurement of optical background in the deep sea using a multi-pmt optical module". PhD thesis. 2017.

[44] *"Nautilus marine service gmbh, vitrovex – glass instrumentation housings."* URL: https://www.vitrovex.com/instrumenthousings/. (Last accessed: 25-2-2022).

[45] *"Shin-etsu chemical co.."* URL: http://www.shinetsusilicone-global.com/index.shtml. (Last accessed: 25-2-2022).

[46] *Healpy documentation site*. URL: https://healpy.readthedocs.io/en/latest/. (Last accessed: 2-2022).

[47] IceCube collaboration. "Gel pad approach masterlist". internal note. 2021. URL: https://docs.google.com/document/d/13MmhrRr1giSseWhEHsz8lW65winMoZ2_jmUpIMQucFc/edit.

[48] H R Band et al. “Acrylic target vessels for a high-precision measurement of 13with the Daya Bay antineutrino detectors”. In: *Journal of Instrumentation* 7.06 (June 2012), P06004–P06004. ISSN: 1748-0221. DOI: 10.1088/1748-0221/7/06/p06004. URL: http://dx.doi.org/10.1088/1748-0221/7/06/P06004.

[49] Pablo Benítez Roland Winston Juan C. Miñano. *NONIMAGING OPTICS*. 2005. ISBN: 0-12-759751-4.

[50] Roland Winston, Lun Jiang, and Melissa Ricketts. “Nonimaging optics: a tutorial”. In: *Advances in Optics and Photonics* 10.2 (May 2018), p. 484. DOI: 10.1364/aop.10.000484. URL: https://doi.org/10.1364/aop.10.000484.

[51] Mustafa Kandemir and Altan Cakir. “Simulation and efficiency studies of optical photon transportation and detection with plastic antineutrino detector modules”. In: *Nuclear Instruments and Methods in Physics Research Section A: Accelerators, Spectrometers, Detectors and Associated Equipment* 898 (Aug. 2018), pp. 30–39. ISSN: 0168-9002. DOI: 10.1016/j.nima.2018.04.059. URL: http://dx.doi.org/10.1016/j.nima.2018.04.059.

[52] Francois Chollet. *Deep learning with python*. en. New York, NY: Manning Publications, Oct. 2017.

[53] Michael A. Nielsen. *Neural Networks and Deep Learning*. Determination Press, 2015.

[54] Diederik P. Kingma and Jimmy Ba. *Adam: A Method for Stochastic Optimization*. 2017. arXiv: 1412.6980 [cs.LG].

Acknowledgement

First of all I would like to thank Prof. Alexander Kappes for giving me the opportunity to write my thesis in this amazing group and for coordinating this double master's degree which has made it possible for me to come back to Münster for another year.

I would like to thank Prof. Carlos Guerrero for accepting to be my second examiner.

Many thanks to all of the members of the AG Kappes in general, for the interesting Mensa discussions, the support offered and the great working atmosphere.

Thank you very much to the guys of room 225, it has been great to spend so much time with you in this whole process.

Special mention goes to Martin Unland and Markus Dittmer, for proofreading my thesis and for the many times you have helped and guided me in the last year.

All this would not be possible without the unconditional support of my mother, Ángeles, and my girlfriend, Nicola Eva. Many thanks to the two loves of my life.